Spin-Spin Interactions and their Impact on Organic Light-Emitting Devices

Dissertation zur Erlangung des
naturwissenschaftlichen Doktorgrades
der Julius-Maximilians-Universität Würzburg

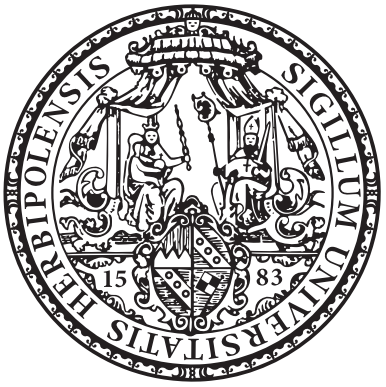

vorgelegt von

Sebastian Günter Weißenseel

aus Schweinfurt

Würzburg, 2021

Eingereicht am: 14.07.2021
bei der Fakultät für Physik und Astronomie

1. Gutachter: Prof. Dr. Vladimir Dyakonov
2. Gutachter: Prof. Dr. Volker C. Behr
der Dissertation.

Vorsitzende(r): Prof. Dr. Porod

1. Prüfer: Prof. Dr. Vladimir Dyakonov
2. Prüfer: Prof. Dr. Volker C. Behr
3. Prüfer: Prof. Dr. Bernd Engels
im Promotionskolloquium.

Tag des Promotionskolloquiums: 19.01.2022
Doktorurkunde ausgehändigt am:

”I have not failed.
I’ve just found 10.000 ways that won’t work.”

Nikola Tesla, inventor of AC systems

Contents

1 Introduction

The saddest aspect of life right now is that science gathers knowledge faster than society gathers wisdom. **Isaac Asimov**

There was a time when we all thought that the exceptional situation we experienced in March 2020 would be short-lived. Even though this situation has almost become everyday life for more than a year now, many branches experienced a renaissance, while others like art, culture and events industry are still at a complete standstill. At this point in time, July 2021, it can be said that especially in the business world and in the sector of school education, the Covid-19 pandemic has brought about an unplanned surge in digitalization overall [1]. A return to the *old normal* is now proving very unlikely. We are on the direct path to the post-Covid era. The variety of offers for digital networking and its use in digital meetings and home schooling has resulted in an enormous additional demand for screens and devices for digital communication and teaching over the last year. "The global display market size was valued at USD 148.4 billion in 2021 and is projected to reach USD 177.1 billion by 2026" says a report from *research and markets* [2]. Meanwhile, organic light-emitting diode (OLED) technology is also getting a big boost in this forecast. Their application in displays has become indispensable and is gaining more and more attention due to their potentially lower production costs compared to conventional display technology such as the liquid crystal display (LCD). Figure 1.1 shows current and predicted sales figures for various application examples in which OLEDs play a major role. While the use in televisions has not yet really taken hold, the share of OLED displays in smartphones and so-called wearables is already quite large. Here, too, the pandemic has made itself felt, as many people have turned from group sports to individual sports due to the contact restrictions. In this niche wearables such as smart watches and fitness trackers are becoming increasingly popular for personal checkups of people's health status. [3–5].

A completely new star on the horizon, however, is the use of OLEDs in transparent display applications, for example in glasses with augmented reality (AR). This makes it possible to project information directly into the user's field of vision, which can be helpful for activities that require both hands to be free [6]. In addition, current research is in the development of tattoo-able OLEDs for use as biosensors or in antimicrobial

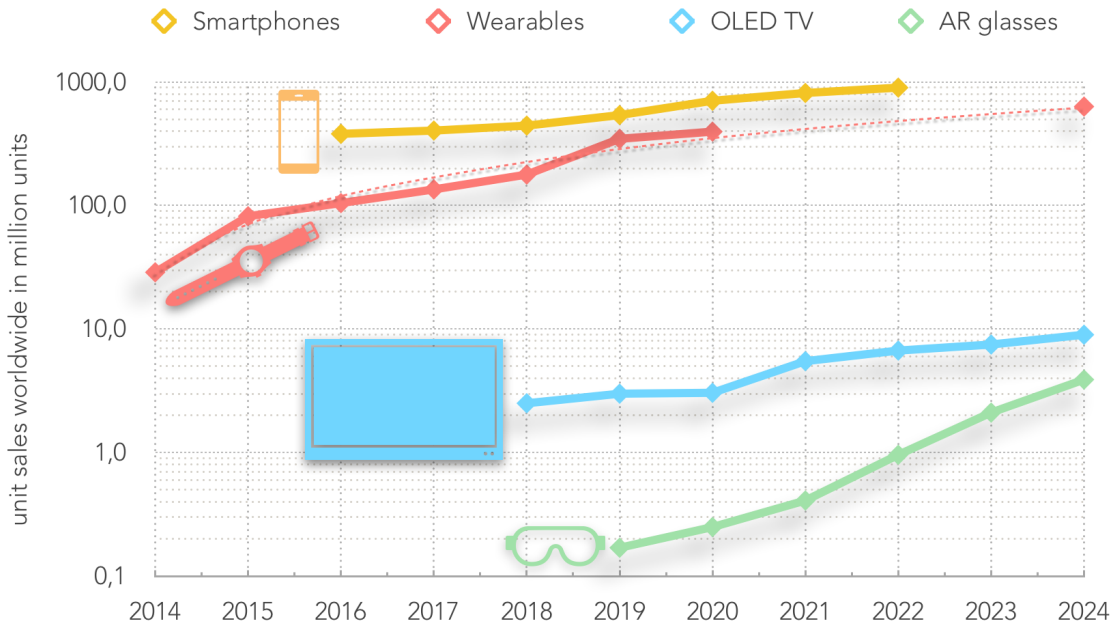

Figure 1.1: The increase in unit sales (in million units) for several display application using OLED technology: Smartphone revenues (predicted values for 2019 to 2022) [3]; OLED TV (predicted values for 2020 to 2024) [4]; AR glasses (predicted values for 2021 to 2024) [6]; wearables (predicted values for 2020 to 2024) [5].

photodynamic therapy [7, 8]. The high demand for applications of OLEDs shows that there is a general desire for this technology and that basic research of various novel OLED materials continues to be of great importance. The currently commercialized OLED devices are mostly based on fluorescent [9–11] and phosphorescent emitters [12, 13]. In order to understand the possibilities of expanding the diversity of OLED emitters through scientific research, the drawbacks of these two approaches will now be briefly outlined.

Upon electrical operation of OLED devices, negative (electrons) and positive charge carriers (holes) are injected at the contacts, which then form 25% radiative singlet states and 75% non-radiative triplet states in the active layer of the device. In fluorescence based devices, also denoted first generation OLEDs, the non-radiative particles are then lost for the light harvesting process, which entails a considerable loss of efficiency. To make up for this loss, precious heavy metal atoms were incorporated into somewhat more complex molecular structures. These generate a strong spin-orbit coupling (SOC) between the singlet and triplet states through a *heavy atom* effect [14, 15]. In this way, it is possible to convert almost all of the generated excitons into triplets, which in this case become radiant due to the strong SOC and can be used by phosphorescence. This type of devices is attributed to the 2nd generation OLEDs. However, the colour blue remains the problem with triplet emitters. There are no blue

triplet emitters that can maintain long-term stability in the device. The main problem for all blue emitters is the high exciton binding energy (2.5 to 3 eV), which makes it highly reactive for oxygen [16, 17]. The longevity of the triplets in phosphorescence emitters, especially of blue emitters, is the Achilles heel of this generation.

A sustainable approach to overcome these issues succeeded with thermally activated delayed fluorescence (TADF). It is a relatively old concept, originally known as E-type delayed fluorescence (DF) [18–21], in which a small energy gap between singlet and triplet enables an inverse process and thus conversion from triplets to singlets. Adachi's group succeeded in using this concept to fabricate efficient OLEDs in 2012, which has since created a new branch of research in the OLED community [22–25]. Here, the thermal activation of the triplets happens via the so-called reverse intersystem crossing (RISC), which in the end enables an internal quantum efficiency up to 100%. The rate of this transition depends strongly on the molecular design of the emitter, primarily on the distance between the electron and the hole on the molecule. More precisely, the energy gap and thus the transition rate can be adjusted by the wave function overlap of the two particles. This directly results in an enormous task for the research groups to find suitable new molecular structures which, on the one hand, have an efficient TADF mechanism, are highly radiant and, on top of that, are freely selectable in their colour through simple synthesis.

This is the starting point for the first project of this thesis. In an international collaboration with OLED researchers from Augsburg, Sion and Lausanne in Switzerland, a novel deep blue TADF emitter is being investigated. Its molecular geometry has been chosen in such a way that, in addition to the TADF property, an increased optical outcoupling of the device is made possible by a stick-like shape. A basic characterization of the emitter, as well as the influence of the molecular geometry on the spin-spin interactions, which determine the TADF and the luminous properties, is examined.

In the further course of the work, several commercially available material systems are examined. The main question is how exactly the RISC process works. Different causes for the spin-flip, such as a weak SOC [26–28] and hyperfine interactions [29] are discussed and investigated on two TADF concepts. Spin-sensitive methods are applied, which allow to manipulate the triplet states and then to query the response of the system optically via the singlets after RISC has taken place. In detail, the linewidth of an electroluminescence detected magnetic resonance (ELDMR) experiment is tested for magnetic field dependence. The huge advantage of this method is the possibility to gain knowledge on spin-dependent processes in fully processed devices under electrical operation.

In the final project, a more in-depth study is performed on a commercially available material system to further expand the immense possibilities of ELDMR. The resonance spectrum typically shows inhomogeneous broadening mechanisms. While in the standard ELDMR experiment the triplet states are manipulated by a single frequency in the radio range, a clever irradiation of a second radio frequency allows to burn a hole into the inhomogeneously broadened spectrum, which gives this method its name: hole burning experiment. The linewidth of the hole is then determined by intrinsic relaxation mechanisms. In this work this method is applied for the first time on an electrically driven OLED device.

However, before the results from the aforementioned projects (i) deep blue emitter (ii) magnetic field dependence of the ELDMR linewidth and the (iii) ELDMR hole burning experiment are presented, all the necessary basics are first explained in detail and their physical connection with OLEDs is discussed. Chapter two explains the basics of organic semiconductors and presents the working principle of an OLED. The basics of spin physics are then provided in the third chapter, while the fourth chapter delivers all the important facts about the experiments, which are conducted. Finally, after the three chapters on results (five to seven), the most important results are presented in a resume.

2 Organic Light Emitting Diodes

Here, the basic principles of organic semiconductors and their application in organic light emitting diodes (OLEDs) are illustrated. The fundamental physics behind these devices like optical and electrical characteristics are explained in detail. The concept of thermally activated delayed fluorescence (TADF), which is the main focus of this thesis, is introduced. The chapter concludes with emphasizing different approaches for achieving efficient OLED devices based on TADF.

2.1 Organic Semiconductors

The world of organic molecules is mainly based on two distinct atoms: hydrogen and carbon. With these two building blocks a huge variety of molecules is already available. The smallest hydrocarbon consists of four hydrogens and one carbon atom: methane. In addition, it is possible that heteroatoms are added, like nitrogen, oxygen or sulfur. A more complex example is the benzene ring. In this carbon ring, the s- and p-orbitals of the six C-atoms overlap while creating a hybrid-orbital. These atomic hybrid-orbitals combine to molecular orbitals (MO), as described in the linear combination of atomic orbitals (LCAO) method [30]. The neighboring atoms create a σ-bond along the ring, while the remaining p_z-orbitals merge to π-bond. In the benzene case a π-cloud above and below the molecular axis is formed, where the π-electrons are delocalized over several atoms in the molecule. The two bonding types are depicted as an example in Figure 2.1a in the molecule ethen C_2H_4. These σ-bonds are shown in blue and the π-bond in red. According to the LCAO method, the total number of atomic orbitals stays the same as for molecular orbitals. If now two atomic orbitals ϕ_a and ϕ_b are considered, the linear combination of those orbitals can be written as $\Psi_+ = c_1\phi_a + c_2\phi_b$. Here, Ψ_+ is the solution of the positive interference of two electron wavefunctions [31]. This MO possesses a bonding character (σ, π, n), while the negative interference $\Psi_- = c_1\phi_a - c_2\phi_b$ evolves anti-bonding character (π^*, σ^*). The parameters c_1 and c_2 are positive numbers. Bonding orbitals lower the energy of the electrons compared to the atomic energy level of the electrons, while anti-bonding MOs are higher in energy than the atomic

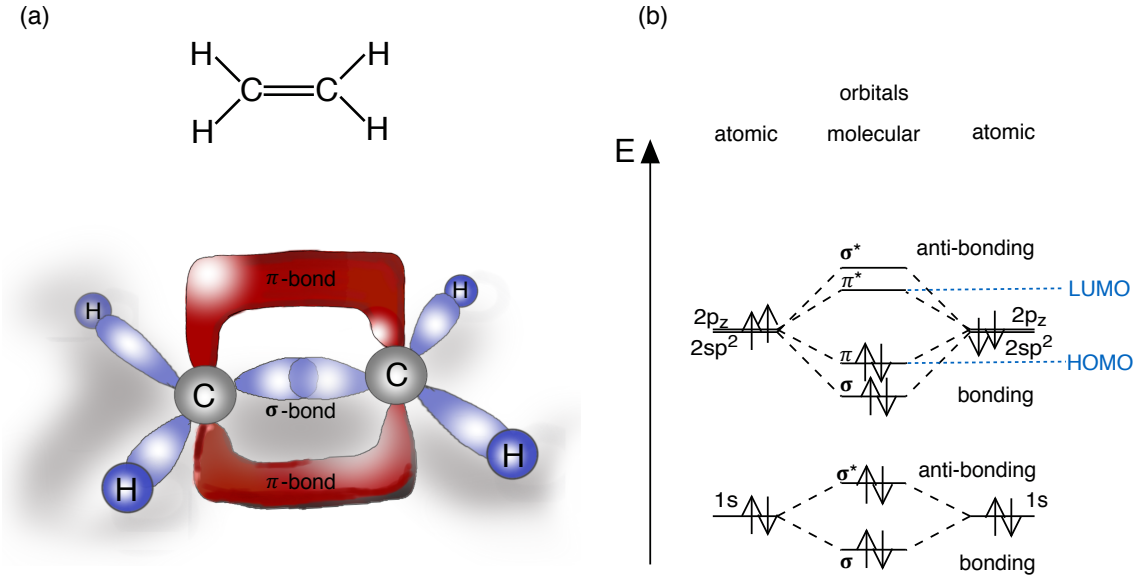

Figure 2.1: (a) Molecular structure and schematic visualisation of the ethen molecule. The carbon atoms exhibit three $\sigma-$bonds (blue) due to the overlap of the hybridized sp^2-orbitals and one π-bond (red) due to overlap of the p_z orbitals. (b) Energetic scheme of molecular orbitals (MO) formed in the ethen molecule from the atomic orbitals of the C-atoms. The atomic orbitals hybridize into bonding and anti-bonding orbitals. These orbitals are filled according to Hund's rule [32]. Here, the π-orbital is the HOMO and the anti-bonding π^*-orbital is the LUMO. Adapted from [31, 33].

level. The corresponding energies are derived from Schrödinger's equation and can be written as [31]:

$$\begin{aligned} E_+ &= \frac{(\alpha+\beta)}{(1+S)} \\ E_- &= \frac{(\alpha-\beta)}{(1-S)} \end{aligned} \tag{2.1}$$

where α describes the Coulomb integral, β the resonance integral and S the overlap integral [31]. An exemplary energetic scheme for ethene is shown in Figure 2.1b. The atomic orbitals, which take part in the binding of the molecule, are the orbitals of the two carbon atoms, the $1s$, $2sp^2$ and p_z-orbitals . Arrows indicate the occupation of the orbitals with electrons according to the Hund's rule [32]. Here, it is notable that the energy of the $2sp^2$ and p_z-orbitals is lowered by the formation of the MOs. The anti-bonding π^*- and σ^*-orbitals are empty. In some cases, not all orbitals are involved in the bonding. These specific orbitals are then called non-bonding n-orbitals. Now, of high interest for electronic transitions are the highest occupied molecular orbital (HOMO) and the lowest unoccupied molecular orbital (LUMO) of the molecule. In the exemplary case of ethene in Figure 2.1, the HOMO is a π-orbital. The next higher

lying unoccupied orbital is the anti-bonding π^*-orbital, here the LUMO. An electronic transition between these two orbitals is denoted as a $\pi - \pi^*$ transition. The energy difference of the π-splitting in most organic compounds is in the visible range of the electromagnetic spectrum and therefore suitable for organic devices like organic solar cells and light emitting diodes [34].

Optical Properties

An important electronic process in organic semiconductors is the absorption of a photon. The lowest state of energy of a molecule is called the ground state. Hence, by absorbing a photon's energy, an electron is lifted to a higher-lying energy state. This creates a so-called excited state of the molecule, which is referred to as exciton [35]. In the process of electronic excitation usually a transition between molecular orbitals is involved. In the general case, the electron is excited from the HOMO to the LUMO. Possible transitions for valance electrons between different energetic states are illustrated in a Jablonski-diagram (Figure 2.2). The ground state is called the S_0 singlet state. Absorption of a photon usually happens from S_0 to the first excited singlet state S_1. There are also transitions possible even to higher lying singlet states S_n. A transition from the singlet ground state to the singlet excited state does not involve a change of the spin state (Spin $S = 0$), which is then called spin-allowed. This transition is fast and in the picosecond to nanosecond range. A transition from the ground state to a triplet (Spin $S = 1$) is first-order spin-forbidden and therefore not very likely to happen. Further details on spin multiplicity are given in Section 3.1. A molecular system also exhibits vibronic modes, thus resulting in vibrational sub-levels of the electronic states. In the Jablonski-diagram the electronic states are given by the thick lines and the vibrational levels v_i by the thin lines. Radiative transitions are given by solid arrows, while non-radiative transitions are shown as dashed arrows. After absorption of a photon from the ground state into a higher vibronic and electronic energy state, non-radiative relaxation from the higher vibronic to the lowest vibronic level occurs immediately via vibrational relaxation (VR). Energy is usually transferred to the surroundings of the molecule. Photon emission occurs from the lowest electronic excited state, which is in the case of a singlet state the S_1 state. This phenomenon is well known as Kasha's rule [36]. Radiative transition from the singlet state is called fluorescence. A non-radiative transition from an excited singlet S_1 to an excited triplet state T_1 is possible by intersystem crossing (ISC). Here, a change of the excitons total spin S is needed, which results in a very slow transition on a microsecond time-scale. Further, the radiative transition from a triplet state is known as phosphorescence. Again a spin-flip is necessary for this process, which also makes the phosphorescence a very slow luminescent transition.

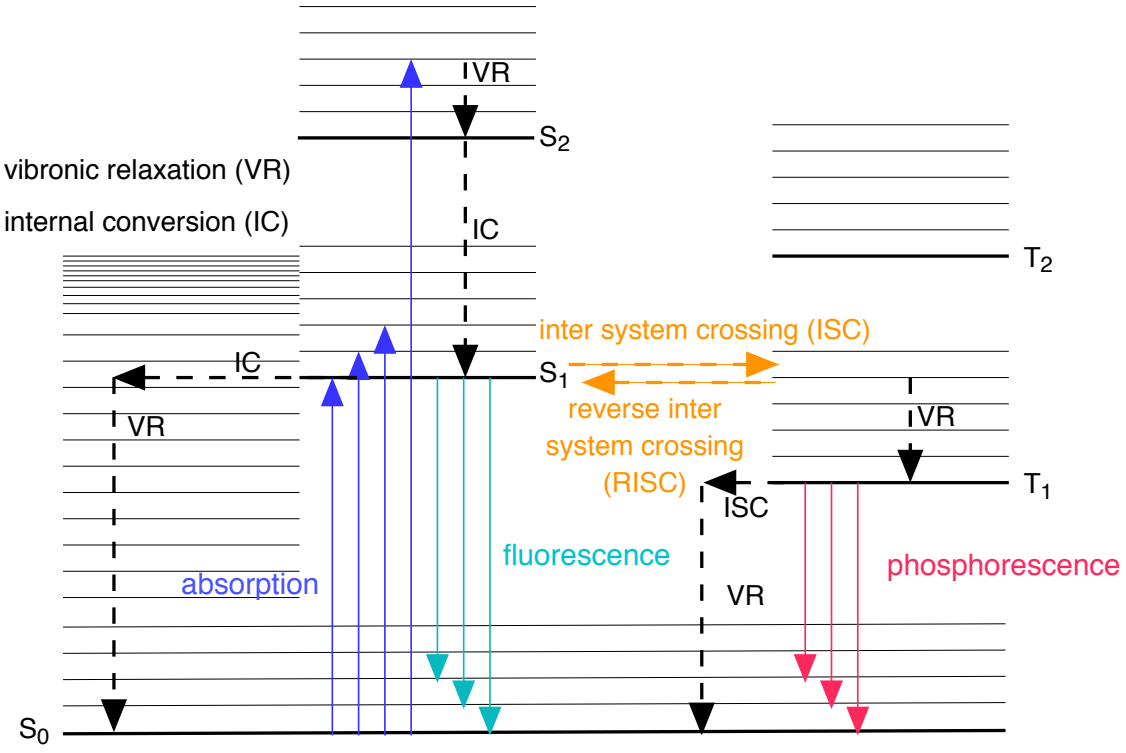

Figure 2.2: Jablonski-diagram demonstrating the possible radiative and non-radiative transitions in an organic molecule. Excitation of the molecule creates a transition from the singlet ground state S_0 to the first excited singlet state S_1 (purple). Electronic states are given by thick lines, while vibrational levels are shown as thin lines. The spin-forbidden transition between singlet S_1 and triplet T_1 is known as (reverse) intersystem crossing (orange). Radiative decay from singlet is denoted as fluorescence (light blue), from triplet as phosphorescence (red). Non-radiative deactivation to the ground state happens via vibronic relaxation (black).

Triplets can also decay non-radiatively by ISC and VR back to the singlet ground state S_0. The non-radiative pendant for higher-lying singlet states is the internal conversion (IC) between the electronic singlet states to the singlet ground state. Reverse intersystem crossing (RISC) from the excited triplet to the excited singlet state builts the fundamental process for all materials investigated in this thesis. Impact of the RISC on the perfomance of modern OLEDs is discussed in detail in Section 2.4. If the nuclear geometry of molecules is also considered in an absorption process, the Franck–Condon principle comes into play. It describes the absorption and emission of light on scale of nuclear coordinates [37] and implies, that nuclear geometry in the molecule does not change under optical excitation, since the movement of electrons and the time scale of absorption is very fast compared to nuclear motion. An absorption process from a vibrational ground state to a vibrational level of a higher electronic state exhibits a higher probability, if the wave function overlap of the nuclear vibronic sub-levels is enhanced. Thus, the spectral intensity of the emission spectra correlates with the transi-

tion probability between the vibrational levels, resulting in the well known vibrational substructure of an organic molecule [31].

Quantum dynamics: transitions in organic molecules

The quantum mechanical description of the aforementioned transitions provides a more detailed insight on the transition rules between the various levels available in Figure 2.2. The following Section is in accordance with [35]. Based on the Born-Oppenheimer approximation the molecular wave function Ψ may be described with three independent approximate wave functions: the electronic wave function Ψ_0 for the electron position and the electronic orbital motion in space, χ_{vib} describes the nuclear configuration and includes vibrational movements of the molecule. Furthermore, Ψ_S characterizes the spin wave function:

$$\Psi \sim \Psi_0 \cdot \chi_{vib} \cdot \Psi_s \tag{2.2}$$

Note that this approximation breaks down if there is non-zero coupling between Ψ_0 and χ_{vib} (vibronic coupling) or between Ψ_0 and Ψ_s (spin-orbit coupling). Nevertheless, Fermi's golden rule implies the basic principles to deduce selection rules if a particle changes its quantum state from Ψ_i to Ψ_f [38]:

$$k_{\mathbf{i}\rightarrow\mathbf{f}} = \frac{2\pi}{\hbar} |\langle \Psi_i | H | \Psi_f \rangle|^2 \frac{dn}{dE} \tag{2.3}$$

The transition rate $k_{\mathbf{i}\rightarrow\mathbf{f}}$ from the initial state Ψ_i to final state Ψ_f is a measure of the transition probability per unit time. In other words, the inverse of $k_{\mathbf{i}\rightarrow\mathbf{f}}$ denotes the *mean* lifetime of the initial state. A better understanding of a direct measure of the lifetime is delivered, if all final states are considered by a summation of all available final states. The matrix element responsible for the perturbation is given by H. dn/dE is the density of states, which are available for the transition. If any desired perturbation creates a matrix element with the value zero, this perturbation cannot drive a transition between Ψ_i and Ψ_f. The transition is called "forbidden". To find efficient transitions, a perturbation needs to be applied, that makes Ψ_i and Ψ_f "look alike" [35]. Here, the operator for example that couples the wave function of the initial and the final state vibrational is called $\mathbf{P}_{\text{vib}}$. One can picture that $\mathbf{P}_{\text{vib}}$ distorts the electronic part of the wave function of Ψ_i into a shape that looks like Ψ_f, which is justified by some vibration in the molecule. Then the transition rate is proportional to the vibrational overlap of the two involved states, the so-called Franck-Condon factor $\langle \chi_i | \chi_f \rangle$ (see Equation 2.4). If now transitions between singlets and triplets and vice versa are considered, the inter-

esting perturbation is the spin-orbit coupling (SOC), which couples the electron spin motion with the electron orbital motion. This perturbation allows a change of the spin wave function, which is the case for (reverse) intersystem crossing (Figure 2.2). Here, the operator of SOC $\mathbf{P}_{\mathrm{SOC}}$ makes a pair of parallel spins (triplet) "look like" a pair of anti-parallel spins (singlet). Together with vibrational coupling, the modified "golden rule" can be written as [35]

$$k_{\mathbf{i}\rightarrow\mathbf{f}} = \underbrace{\left[\frac{k_{\max}\langle\Psi_i|\mathbf{P}_{\mathrm{vib}}|\Psi_f\rangle^2}{\Delta E_{if}^2}\right]}_{\text{vibrational coupling}} \times \underbrace{\left[\frac{\langle\Psi_i|\mathbf{P}_{\mathrm{SOC}}|\Psi_f\rangle^2}{\Delta E_{if}^2}\right]}_{\text{spin-orbit coupling}} \times \underbrace{\langle\chi_i|\chi_f\rangle}_{\substack{\text{vibrational overlap}\\ \text{Franck-Condon factor}}} \tag{2.4}$$

where k_{max} is the maximum possible rate constant (zero-point motion), ΔE_{if}^2 is the energetic separation between Ψ_i and Ψ_f. If no change of spin is involved in the transition, the second term is missing in Equation 2.4. Till now, only radiationless transitions have been considered. The interaction of electrons with the electric and magnetic field of light is described by an energy exchange between the electromagnetic field of the photon and the molecule. When the resonance condition $\Delta E = h\nu_{ph}$ is satisfied, the oscillation of the electric field F of the photon creates a charge separation Δr. The extent of the displacement is given by the vector $\mathbf{r}$. If this vector is mulitplied by a unit electric charge e, this results in the classical dipole moment $\mu_i = e\mathbf{r}$. This dipole moment is now the perturbation of interest in Equation 2.3, which acts on the electronic part of the wave function Ψ_0 (see Equation 2.2). The nuclei (χ_{vib}) are not affected by the oscillation of the electromagnetic field, as well as the spin (Ψ_S). With the dipole moment, a measure of the transition strength can be defined. In a simple model, the oscillator strength f can be viewed as the ratio of the intensity of radiation or absorption emitted by a molecule compared to the intensity of an oscillation of a single electron bound to that molecule, which is in this case described by an classical harmonic oscillator [35]. In the ideal case of a perfect harmonic oscillator $f = 1$, which means, every passing photon has a maximum probability of absorption. The oscillator strength is directly connected to the matrix element of the quantum mechanical transition dipole moment $\mu_i^2 = \langle\Psi_i|\, e\mathbf{r}\,|\Psi_f\rangle^2$

$$f = \left(\frac{8\pi m_e \nu}{3he^2}\right)\cdot\mu_i^2 = \left(\frac{8\pi m_e \nu}{3he^2}\right)\cdot\langle\Psi_i|\, e\mathbf{r}\,|\Psi_f\rangle^2 \tag{2.5}$$

where m_e is the mass of the electron, ν is the energy of the transiton (in cm^{-1}), h is the Planck's constant and $\mathbf{r}$ is the length of the transition dipole (in cm). Due to the overlap integral in this equation, it becomes clear how the radiative strength of a transition depends on the orbital nature of the involved states. Transitions with a $\pi - \pi^*$-

character usually exhibit an oscillator strength of 10^{-2} to 1, while transitions with a $n-\pi^*$-character, also known *charge transfer states*, are in the range of 10^{-5} to 10^{-3} [31]. The importance of charge transfer states for efficient TADF devices is highlighted in Section 2.5, while the influence of the oscillator strength on TADF emitters is investigated in the result chapter 5.

Transport Properties

Although the π-electron system stabilizes the molecule's geometry, there is almost no direct electronic interaction between neighboring molecules. Each molecule acts as an isolated block in an organic amorphous crystal. These blocks solely interact via the weak van-der-Waals forces. Thus, in contrast to inorganic crystals, where charges are embedded in a well-formed three dimensional lattice structure, here, the transport can not be described by collective phenomena. In disordered amorphous films, in general, the HOMO and LUMO levels are statistically distributed due to random orientation of the individual molecules. In more detail, Heinz Bässler described the density of states (DOS) in amorphous solids in his Gaussian disorder model (GDM) with the following distribution [39]

$$g(\epsilon) = \frac{1}{\sqrt{2\pi}\sigma}\exp\left(-\frac{(\epsilon-\epsilon_0)^2}{2\sigma^2}\right) \tag{2.6}$$

where ϵ_0 is the mean value of the energy distribution and σ, the Gaussian disorder parameter, or in other words the width of the distribution, which is usually in the order of $\sim 100\,\text{meV}$ [31]. The disordered energy landscape is shown schematically in Figure 2.3. Without any interaction with the environment, charges are localized within the π-electron system and hence the charge carriers are trapped on the molecule. A small electronic coupling between two neighboring molecular crystal sites allows a tunneling process from one site to the other. In the famous Marcus theory, this tunnel probability was first mentioned to depend on the transfer integral between the wavefunctions of the corresponding energy states [40]. Miller and Abrahams further improved this approach by taking into account phonon assisted hopping between energetically non-equivalent sites. The transition rate ν_{ij} for such a phonon assisted hopping process between two sites i, j is given by [41]

$$\nu_{ij} = \nu_0 \exp(-2\gamma R_{ij}) \begin{cases} \exp\left(-\frac{E_j - E_i}{kT}\right) & E_j > E_i \\ 1 & E_j < E_i \end{cases} \tag{2.7}$$

where ν_0 is the attempt–to–escape frequency, R_{ij} is the spatial distance between the two energy states, γ is the overlap factor. The first term in the equation considers

the distance dependence of ν_{ij}, while the second term is thermally activated for upward hopping and equal to one for downward hopping in energy. Now, if the system approaches the thermal equilibrium, the charges occupy the lower energetic tail of the DOS. The density ρ of these charge carriers is again found to be energetically distributed, which is considered by the density of occupied states (DOOS). The mean energy value of the DOOS is given by $E_m = \sigma^2/kT$. So far, the mobility μ can now be derived from the Gaussian disorder model as [39]

$$\mu(T,E) = \mu_0 \exp\left[-\left(\frac{2\sigma}{kT}\right)^2\right] \cdot \exp\left[C\sqrt{F}\left(\left(\frac{\sigma}{kT}\right)^2 - \Sigma^2\right)\right] \tag{2.8}$$

with σ the Gaussian disorder parameter, C a scaling factor and Σ a spatial disorder parameter. Note that in such a disordered system an external applied electric field F also increases the mobility in the hopping transport mechanism. The GDM does not account for correlated hopping sites, however, it explains the basic ideas of the hopping transport in disordered organic systems. Several more advanced models describing the transport phenomena in organics are found in literature [42], [43], [44].

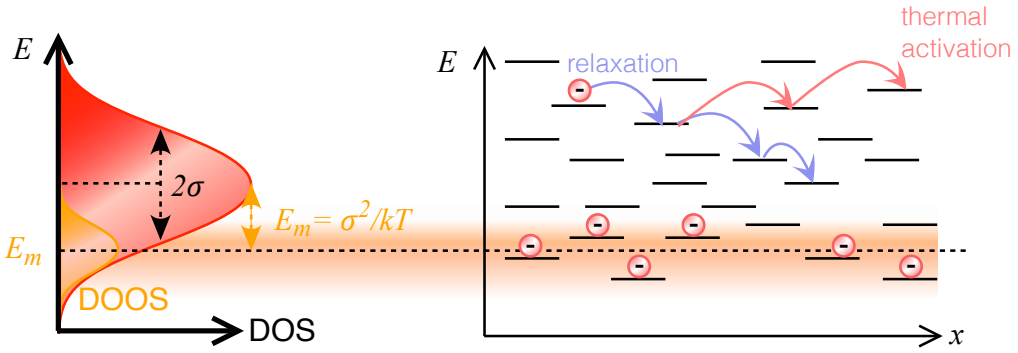

Figure 2.3: Gaussian distribution of density of states (DOS) in the LUMO of an amorphous organic seminconductor. The energy states are randomly distributed in space. In thermal equilibrium the lower tail of the DOS is occupied. Charge transport from site to site is possible only by hopping transport under participation of phonons. The downward hopping probability is equal to unity, while upward hopping is thermally activated. Adapted from [31].

Metal-organic interfaces

If an organic device is operated electrically, it needs to be wired by metal contacts in order to apply a voltage and to inject a current. At some point in the electric circuit, there has to be a transition from the conductive metal to the organic world and therefore a transition from the inorganic band transport to the organic hopping transport. This is happening at the metal-organic interface. If an organic semiconductor is brought in

contact with a metal, it is crucial to look at the difference of the Fermi level E_F of the metal and the electron affinity χ_{el} of the organic semiconductor. Or in other words, the work function of the metal $\phi_{w,M}$ and the HOMO/LUMO of the organic. The energetic barrier between the metal and semiconductor can be described by a Schottky-barrier. At the interface, the Fermi levels of both materials equalize, which results in a bending of the band structure of the semiconductor. The height of the injection barrier for electrons δ_{EIB} depends on the work function $\phi_{w,M}$ of the metal and the energy of the LUMO level and is given by $\delta_{EIB} = \phi_{w,M} - \text{LUMO}$ with respect to the vacuum level. For holes, the energetic barrier is given by the difference between the metal and the HOMO energy level $\delta_{HIB} = \text{HOMO} - \phi_{w,M}$. Additionally, in most cases, an interface dipole is formed in the organic layer due to electronic interaction of the molecules with the metal [45],[46]. This dipole either reduces or increases the barrier of the Schottky-contact, depending on the direction of the dipole formation. Nevertheless, the charge carriers have to overcome the barriers δ_{EIB} and δ_{HIB}, before an efficient charge current flow is possible. This is possible either by thermionic emission following the Richardson–Schottky equation [47]. Firstly, this phenomenon considers the thermal energy of the charge carriers to overcome the energetic barrier. The second possibility for efficient charge injection is Fowler-Nordheim tunneling, which is favored at higher electric fields [48]. Here, the electronic band structure is bent by the external field in such a way that the charge carriers are able to tunnel through the barrier. The tunnel-probability for this process depends on the width of the barrier and the applied electric field. This process is well known as field emission. Both processes are present in organic devices and are crucial for efficient charge injection at the metal-organic interface.

2.2 Layer and Energy Structure of Organic Light Emitting Devices

After electronic transitions and transport in disordered organic semiconductors are introduced, the focus is now drawn to the application of these two mechanism for light generation in devices. The emergence of light emission from organic compounds started as the first organic electroluminescence from an antracen-single crystal was reported by Pope et al. in 1963 [49]. His group delivered the basic knowledge about the energetic requirements needed for charge carrier injection into organics, which is still valid for modern devices. The first real light emitting device working as an OLED was based on the organic compound 8-hydroxyquinoline aluminum (Alq_3) reported by Tang and van Slyke [50]. It was built of a glass substrate coated with indium-tin-oxide

(ITO). The top electrode was an alloy or mixture of magnesium and silver. The layer of the luminescent material between these electrodes was only 60 nm thick. That was the first step of the huge research field of light emitting organic thin-film devices.

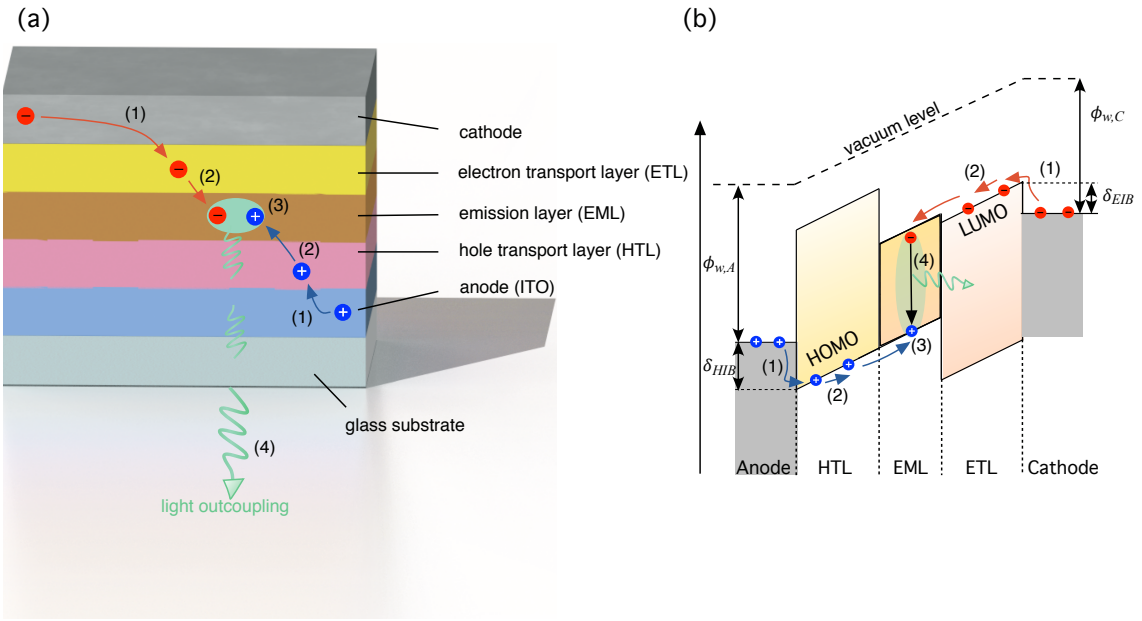

Figure 2.4: (a) Schematic Layer structure of an organic light emitting diode. The organic layers are processed on a indium-tin-oxide (ITO) covered glass substrate. The emission layer (EML) is sandwiched between the electron/hole transport layers (ETL/HTL). The top electrode is usually a low work function $\phi_{w,C}$ metal, e.g. aluminum. (b) The energetic landscape of an OLED device under electrical operation with an external voltage U_{ext}. The desired stages for efficient electrical operation of an OLED are (1) charge carrier injection from the electrodes into organic layers by overcoming the injection barriers $\delta_{EIB}/\delta_{HIB}$, (2) transport of charge carriers by hopping transport, (3) exciton formation in the EML and (4) radiative recombination of excitons and light outcoupling. Modified from [34].

Layer structure

Now, the basic layer structure of a modern OLED device is shown in Figure 2.4a. For efficient light out-coupling, OLEDs are usually processed on a transparent substrate like glass or, even for flexible devices, on plastic sheets. The anode is a thin layer of a sputtered material with a low work function ϕ_w for efficient hole injection, the ITO layer. For the first organic layer, the hole injection layer, the energetic barrier δ_{HIB} between the work function $\phi_{w,A}$ of the ITO and the HOMO of the organic material is required to be small (Figure 2.4b). The hole injection layer often also works as a transport layer for the injected charges. The same requirements hold for the electron injection from the cathode into the LUMO of the electron transport layer (ETL). The barrier δ_{EIB} between

the work function $\phi_{w,C}$ and the LUMO of the ETL should also be kept at a minimum. A typical metal used for the cathode is aluminum. To further reduce the workfunction, often calcium (Ca) or lithium-flouride (LiF) layer is placed between the organics and the cathode. If an external voltage is applied to the device, a voltage drop is generated between the anode and the cathode and the injected charge carriers diffuse through HTL/ETL by hopping transport. The sandwiched emission layer (EML) is filled with electrons and holes simultaneously. Preferably, the LUMO of the HTL (or the HOMO of the ETL) exhibits a higher (lower) energetic value to block electrons (holes) from exiting the EML. In this case, electrons and holes are energetically confined in the EML. With this specific energetic landscape within the device, the efficient formation of bound excitons is ensured (Figure 2.4b).

Characteristic device parameter

In order to characterize a device after preparation, it needs to be measured by a current response for an externally applied voltage. During a sweep of the electric current density j, the electroluminescence of the device is monitored simultaneously. The measurement of the mentioned quantities leads to fundamental current–voltage– luminescence characteristics, also called j-V-EL-curve. The ideal current behavior of a diode is described by the ideal Shockley-equation, which postulates an exponential increase of the device current with increasing external voltage [51]

$$j = j_0 \left(\exp\left(\frac{qV)}{nk_bT} \right) - 1 \right) \tag{2.9}$$

with j_0 as the saturating current for reverse operation, V applied voltage, n the ideality factor, k_B Boltzmann factor and q elementary charge. In a real device, several effects lead to a discrepancy from the ideal Shockley-equation. Shunt and series resistive effects lead to the "non-ideal" shockley equation [52]

$$j = j_0 \left(\exp\left(\frac{q(V - jAR_S)}{nk_bT} \right) - 1 \right) + \frac{V - jR_SA}{R_PA} \tag{2.10}$$

where jR_sA represents the voltage drop due to a series resistance, A is the active area of the device. The last term accounts for a linear increase of the current due to a parallel resistance.

External quantum efficiency

The external quantum efficiency (EQE) summarizes several mechanisms, which contribute to the total efficiency of an electrically driven device, starting from free charge carriers to a photon exiting the device. In short the EQE quantifies the amount of photons leaving the devices per injected charge carrier pairs. The formula of the EQE is given by the internal quantum efficiency (IQE) η_{int} times the out-coupling factor η_{out} [34]

$$\eta_{\text{ext}} = \eta_{\text{int}} \cdot \eta_{\text{out}} = \gamma\, \eta_{\text{r}}\, \eta_{\text{eff}}\, \eta_{\text{out}} \tag{2.11}$$

Here, γ is the charge carrier balance factor, which is the probability of a charge carrier to encounter its counterpart for exciton formation. In modern OLED devices with optimized layer thicknesses and energetic matching of the HOMO/LUMO levels for efficient injection, this factor is considered to be $\gamma = 1$ [53]. Further, η_{r} is the singlet-triplet factor, which tells how many excitons are formed in the singlet state for photon generation in the emission layer. Usually, considering the electron/hole spin, the statistical ratio of singlet and triplet yield is 1:3. The effective quantum efficiency η_{eff} considers the quantum mechanical probability of photon generation if the emission layer is embedded into a micro-cavity and is depending on the Purcell factor F. A micro cavity can either enhance or reduce the probability of radiative recombination if the wavelength of the electric field of the light emission is in the order of the physical dimensions of the OLED device. The effective quantum efficiency is given by

$$\eta_{\text{eff}} = \frac{\text{F} \cdot \Gamma_{\text{r}}}{\text{F} \cdot \Gamma_{\text{r}} + \Gamma_{\text{nr}}} \tag{2.12}$$

with the transition rates for radiative Γ_{r} and non-radiative Γ_{nr} recombination. If a photon is generated in the emission layer, there is only a chance smaller than one for the photon to exit the device. The out-coupling factor η_{out} considers the total reflection of a photon at the layer interfaces with different optical density n. One can show that the out-coupling factor is approximately given by the mean refractive index n of the organic layers as [54, 55]

$$\eta_{\text{out}} = \frac{1}{2n^2} \tag{2.13}$$

This formula gives an estimation of the upper limit of the optical output power if one assumes values of $n = 1.6 - 1.8$. The assumption limits the EQE for isotropic emitters in the EML to $\eta_{\text{ext}} \sim 15 - 20\%$ if all other parameters of formula 2.11 taken with their theoretical maximum. However, this limit can be exceeded if the orientation of emission of the emitters is optimized. Simulations show that η_{eff} can be increased by 50% by the

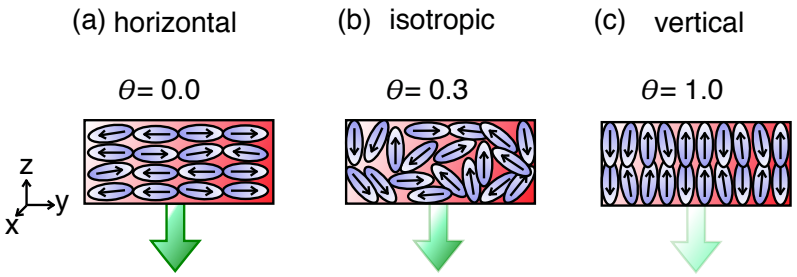

Figure 2.5: Orientation of the transition dipoles (black arrows) in an amorphous emission layer. The anisotropy factor θ is a measure of the distribution of the transition dipole moment in the emission layer. Influence of horizontal ($x-y-$plane) $\theta = 0$, isotropic $\theta = 0.3$ and vertical ($z-$direction) orientation show decreasing emission properties (green) in z-direction.

use of horizontal dipole moments in contrast to isotopic emission [56], [57]. Here, the Purcell factor F is replaced by the expression $F(\theta)$ [58], [34]

$$F(\theta) = \frac{1-\theta}{2} \cdot (F_x + F_y) + \theta \cdot F_z \tag{2.14}$$

The parameter of interest is here the orientation anisotropy factor θ of the Purcell factor F. For isotropic orientation $\theta = 1/3$, for horizontal orientation $\theta = 0$ and for vertical orientation $\theta = 1$. Here, horizontal orientation is in $x-y-$plane and vertical in $z-$direction.

2.3 Classification of OLED Emitters

The previous sections introduced all the fundamental principles which are needed to understand the electrical operation of an organic device. Nevertheless, the focus is now drawn to detailed pathways and intermediate states of the involved excitons and how these states and the transition rates between them are affected by the molecular structure of the emitter. Figure 2.2 already demonstrated the interconversion between excited singlet S_1 and excited triplet states T_1 by ISC and RISC. These processes are important to understand the emergence of the three generations of OLED emitters. For comparison all three types of OLED emitters are shown in Figure 2.6.

- **Fluorescent emitters**
  In fluorescent emitter based devices, only the singlet excited states S_1 show luminescence and hence the IQE is limited to $\eta_{\text{int}} = 25\%$, due to a singlet-triplet ratio of 1:3. In contrast, the triplet states T_1 decay non-radiatively, which is a huge drawback regarding the EQE. In total, fluorescent emitters are limited to $\eta_{\text{ext}} = 5\%$. The rate of intersystem crossing k_{ISC} from the S_1 to T_1 is usually is very

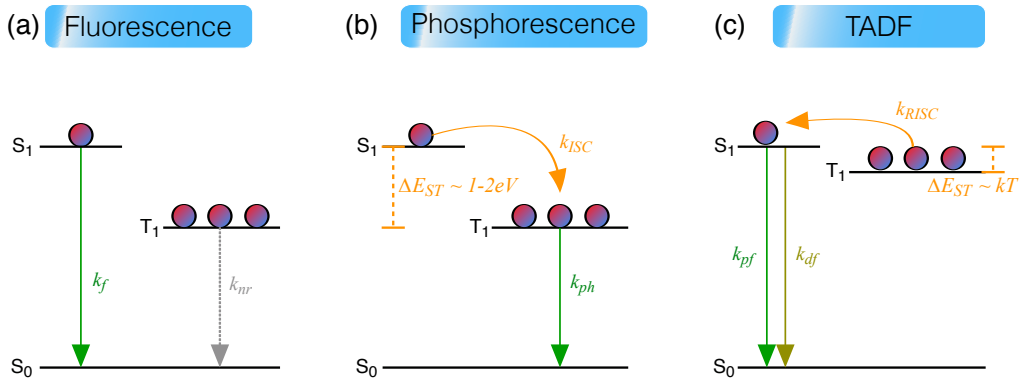

Figure 2.6: The three classes of OLED emitters. (a) Fluorescence emitter make use of singlet states only (k_f) . Triplets are energetically trapped and decay non-radiatively (k_{nr}) (b) In phosphorescence based emitter, heavy atoms enable spin-orbit coupling, which allows intersystem crossing (k_{ISC}) of singlets to low-lying triplet states ($\Delta E_{\mathrm{ST}} \simeq 1-2\,\mathrm{eV}$). The radiative transition to ground state via phosphorescence is in a time range of hundreds of μs to several ms. (c) Emitters making use of thermally activated delayed fluorescence (TADF) exhibit a small singlet-triplet gap ($\Delta E_{\mathrm{ST}} \simeq kT$), which allows the triplet-to-singlet up-conversion by reverse intersystem crossing k_{RISC}, followed by delayed fluorescence k_{df} at a microsecond time-scale. Initially generated singlets decay via prompt fluorescence k_{pf} in nanosecond time-scale, similar to (a).

low, since there is no strong driving mechanism to allow spin-forbidden singlet-to-triplet conversion.

- **Phosphorescent emitters**

  To overcome the drawback of low IQE, heavy metal atoms have been introduced into emitting molecules which enable a channel for singlets to undergo ISC efficiently [13, 59–61]. In addition, this class of emitters enables room temperature phosphorescence from the lower-lying triplet levels by making use of the heavy-atom effect. This effect increases the so-called spin-orbit coupling matrix element between the singlet and the triplets, or in other words, it allows spin-flips in the spin-forbidden T_1 to S_0 transition. Thus, phosphorescent emitters can be realized exhibiting a theoretical IQE of $\eta_{\mathrm{int}} = 100\%$. The mean lifetime of radiative transition to ground state via phosphorescence is in a time range of hundreds of μs to several ms.

- **TADF emitters**

  In this thesis the focus is on the third type of emitters, the so-called TADF emitter. Here, the up-conversion of triplets to singlets is enhanced by efficient reverse intersystem crossing (RISC) [23, 62]. The subsequent emission after RISC is called *delayed* fluorescence. In addition, the RISC process is thermally acti-

vated which increases the fraction of delayed emission with rising temperature. Hence, the electrically generated singlet S_1 states exhibit a typical fluorescent lifetime of several tenth of nanoseconds which is called *prompt* fluorescence. In contrast, the pathway of electrically generated triplets through RISC happens at a microsecond time-scale. Due to efficient thermally activated delayed fluorescence (TADF), an IQE of $\eta_{\text{int}} = 100\%$ is also possible with this class of OLED emitters.

2.4 Singlet-Triplet Gap and Triplet-to-Singlet Up-Conversion

The crucial parameter dominating the efficiency of a TADF emitter is the singlet-triplet gap ΔE_{ST}. Conventional emitters exhibit usually singlet-triplet gaps of several hundred meV to $1\,eV$. The customized design of the molecule's geometry allows to decrease this gap down to several tenth of meV. In this case, the thermal activation of the lower-lying triplet T_1 to the higher-lying singlets S_1 is possible, since $\Delta E_{ST} \approx k_B T$ and thus is in the range of the thermal energy. The rate of the triplet-to-singlet up-conversion k_{RISC} is then following the Boltzmann term [62]

$$k_{RISC} \sim \exp\left(-\frac{\Delta E_{ST}}{k_b T}\right) \tag{2.15}$$

in detail, the more thermal energy in the system is available, the more triplets occupy higher vibronic levels. Hence, the triplets at higher vibronic levels being iso-energetic to the S_1 vibrational ground state can undergo the transition via reverse intersystem crossing. In this process, a change of the total spin S of the exciton from $S = 1$ to $S = 0$ is desired (see Section 3.1). This spin-conversion involves a quantum mechanical effect called spin-mixing. One can describe the electronic states by perturbation theory. Two states with different spins can have the same energy, but still the transition between these states is spin-forbidden. This is the case if only the zeroth order is considered. The character of theses states is described as *pure* [35]. The first and second order treatment according perturbation theory may include some *mixed* terms. In literature, several mechanisms are discussed to be responsible for the spin mixing: the hyperfine interaction (HFI) [29], spin–orbit-coupling (SOC) [26–28] or the Δg-mechanism [63]. In other words, there must be a magnetic interaction which acts solely on the spin of one of the two involved charge carriers forming the exciton. All three interactions are defined in more detail in chapter 3.

The determining factor in Equation 2.15 is the singlet-triplet gap ΔE_{ST}. The aim of

TADF emitters is to gain maximum efficiency by keeping the RISC rate k_{RISC} at a maximum, that is at a low value of ΔE_{ST}. To know how this value can be influenced, one needs to have a look on the origin of the spitting [64–67]:

$$\Delta E_{S-T} = E_T - E_S \simeq 2J_{ex} \tag{2.16}$$

where J_{ex} is the exchange integral between the two particles, which form the exciton. More details on the exchange integral is given in Section 3.2.1 (Equation 3.10c). The main parameter giving rise to the value of the integral is the spatial overlap of the orbital wavefunctions of the HOMO ϕ_{HOMO} and the LUMO ϕ_{LUMO}. For ordinary compounds, ϕ_{HOMO} and ϕ_{LUMO} have similar shapes and locations on the molecule. Thus, the exchange interaction J_{ex} of the involved charge carriers is high due to enormous overlap of the wavefunctions. In contrast, the challenge of finding an efficient TADF emitter is to create a spatial separation of the HOMO/LUMO orbitals by a smart choice of donor and acceptor elements. Unfortunately, the oscillator strength f suffers from the decreased electron-hole coupling and hence it is important to keep an eye on the emission properties while tuning the triplet-to-singlet up-conversion [68, 69].

2.5 Guest-Host vs. Donor-Acceptor Approach

For efficient harvesting of the non-radiative triplet states in TADF compounds, a spatial separation of the ϕ_{HOMO} and ϕ_{LUMO} wavefunction is desired. So far, two different approaches have been made in the OLED community to fulfill this requirement. The first one in based on the separation of the donor and acceptor group of a single molecule (Figure 2.7a). Here, the separation is realized for example by introducing a twist, creating large distances between electron and hole inside one molecule by donor and acceptor units that are almost perpendicular to each other. The resulting energy state in this case is usually denoted as a **charge transfer** (CT) state [23, 24, 68]. Since it is based on a charge transition inside the emitter, this approach is well known as *intra*-molecular TADF. Commonly, CT-TADF emitters are embedded in a transparent wide-band gap matrix with a ratio of 10:90 to prevent self-quenching effects between neighboring emitter molecules.
The second TADF concept is based on the approach to completely dislocate the electron and the hole wave functions on two distinct molecule [62, 70–72]. The resulting excitonic state is here called an **exciplex** (Figure 2.7b). The wavefunction of the hole is located in the HOMO of the donor molecule, while the wavefunction of the electron is located in the LUMO of the acceptor molecule. The concept is also referred to as

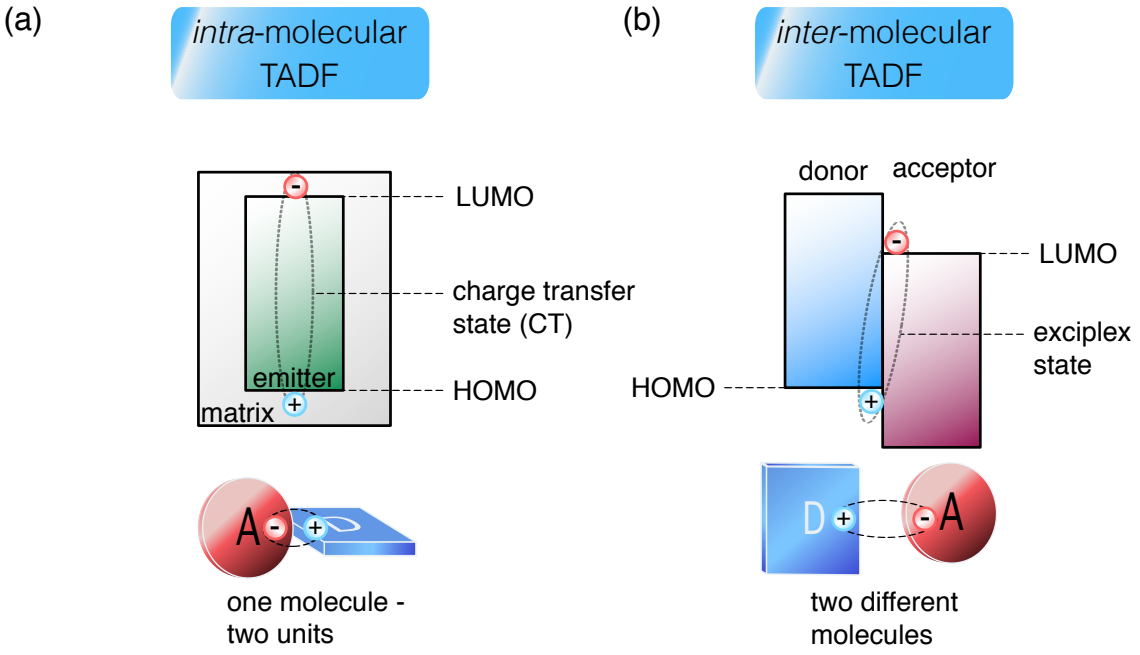

Figure 2.7: The two TADF approaches: (a) *charge transfer* (CT) emitter: The TADF-process takes place on only *one* emitter molecule consisting of perpendicular acceptor and donor units. The concept is called *intra*-molecular TADF and the involved state is a *charge transfer* (CT) state. Commonly, the emitter is embedded in a matrix layer with low emitter concentration (10:90) (host-guest system). (b) *exciplex*-D-A-complex: inter-molecular TADF based on a Donor-Acceptor approach with two different molecules taking part in the emission.

inter-molecular TADF. Here, the challenge is less separation of the ϕ_{HOMO} and ϕ_{LUMO} by synthesis, but more to match the right compounds with corresponding HOMO and LUMO levels. To increase the probability of forming D:A-pairs, a co-evaporation of both materials with a ratio of 50:50 is often used, instead of a direct two-layer interface [70].

3 Electron Paramagnetic Resonance

The previous chapter introduced the fundamentals on organic light emitting diodes. An important physical quantity, which determines the efficiency of these devices is the spin. It is inevitable to have a closer look on the spin and its impact on the transition processes in TADF compounds. This chapter provides a detailed background of the underlying spin-physics and how to apply spin-sensitive methods based on electron paramagnetic resonance (EPR) to gain new information for OLED improvement. The spin theory is given in a nutshell in accordance with [73], [74] and [75].

3.1 The Spin

The spin S is a quantum mechanical intrinsic property of a particle referred to an angular momentum. In contrast to the orbital angular momentum L, there is no classical counterpart to the spin. Its property is to precess around the external magnetic field vector $\vec{B}$ with a precession frequency ω_L, the Lamor-frequency, with the gyro-magnetic ratio γ [73]:

$$\omega_L = \gamma \cdot B \tag{3.1}$$

For a free electron the gyro-magnetic ratio is given by $\gamma = g\mu_B/\hbar$, where g is the Landé factor, μ_B is the Bohr magneton and $\hbar$ the reduced Planck constant. The phenomenon, the spin, was first discovered by Stern and Gerlach in 1922, who observed a splitting of a beam of silver atoms in an inhomogeneous magnetic field [76]. While the spin quantum number I of nuclei depends on the isotope, electrons always posses a spin of $S = 1/2$, as all fermionic particles. With respect to the direction of the external magnetic field $\vec{B}$ the spin can occupy $2S+1$-states. For electrons this number ends up in two states in z-projection of the spin vector (see Figure 3.1a), the parallel alignment $|\uparrow\rangle$ for the so-called *spin-up* state and anti-parallel alignment $|\downarrow\rangle$ for the *spin-down* state referred to as a *doublet state*. These spin eigenstates are part of the total wave function of the electron Ψ. It is the product of the electronic Ψ_{el}, the vibrionic Ψ_{vib} and the spin wave function Ψ_{spin}, resulting in $\Psi = \Psi_{el}\Psi_{vib}\Psi_{spin}$. The multiplicity of a doublet

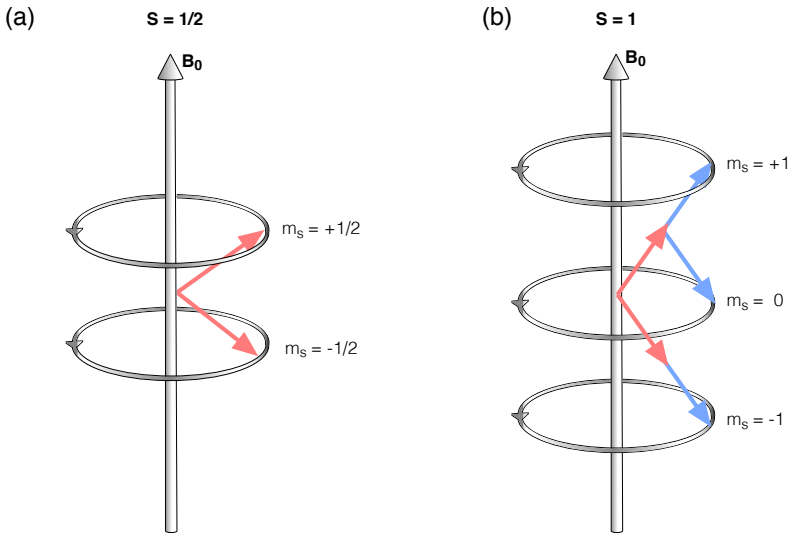

Figure 3.1: (a) Spin doublet with spin $S = \pm 1/2$ and $m_s = \pm 1/2$ (b) Triplet with three-fold multiplicity and a total spin of $S = 1$. The triplet sub-states are described by $m_s = -1, 0, +1$

state is equal to 2. These two states are described by the magnetic quantum number m_s. The magnetic quantum number is determined by the spin quantum number S of the particle

$$m_s = -S, (-S+1), ..., (S-1), +S. \tag{3.2}$$

In systems with more than one un-paired (electron) spin, spin-spin interactions are possible. The interaction of the spins leads to a summation of the individual spin quantum numbers $S = S_1 + S_2$, resulting in either a *singlet* state or a *triplet* state, with a total spin of $S = 0$ and $S = 1$. If now the underlying states are described by a total wave function $\Psi = \Psi_{el}\Psi_{spin}$ again, the eigenstates of the four resulting new spin states can be written as [31]:

$$\begin{array}{lll} \text{Singlet:} & \Psi_{spin,S} = \frac{1}{\sqrt{2}}(\alpha_1\beta_2 - \beta_1\alpha_2) & S = 0; m_s = 0 \\ \text{Triplet:} & \Psi_{spin,T_+} = \alpha_1\alpha_2 & S = 1; m_s = +1 \\ & \Psi_{spin,T_0} = \frac{1}{\sqrt{2}}(\alpha_1\beta_2 + \beta_1\alpha_2) & S = 1; m_s = 0 \\ & \Psi_{spin,T_-} = \beta_1\beta_2 & S = 1; m_s = -1 \end{array} \tag{3.3}$$

Here, α and β are the spin wave functions of the one-electron states with $S = 1/2$ and $m_s = 1/2$ and $S = -1/2$ and $m_s = -1/2$, respectively. A schematic diagram of a triplet spin system is given in Figure 3.1b. The singlet state is denoted as S and magnetic quantum number $m_s = 0$, while the triplet sub-levels are called T_+, T_0, T_- states, with magnetic quantum numbers $m_s = +1$, $m_s = 0$ and $m_s = -1$. The multiplitiy of the

singlet state is one-fold and the triplet multiplicity threefold. Another quantum mechanical description of the spin is done by the spin operator vector

$$\mathbf{S} = \begin{pmatrix} S_x \\ S_y \\ S_z \end{pmatrix} \tag{3.4}$$

while its components contain the Pauli matrices σ_i. For a spin $S = 1/2$ system the components read as

$$S_x = \frac{\hbar}{2}\sigma_x \qquad S_y = \frac{\hbar}{2i}\sigma_y \qquad S_z = \frac{\hbar}{2}\sigma_z \tag{3.5}$$

with the Pauli matrices

$$\sigma_x = \begin{pmatrix} 0 & 1 \\ 1 & 0 \end{pmatrix} \qquad \sigma_y = \begin{pmatrix} 1 & 0 \\ 0 & -1 \end{pmatrix} \qquad \sigma_z = \begin{pmatrix} 0 & 1 \\ -1 & 0 \end{pmatrix} \tag{3.6}$$

The direction of the precession of a spin can be changed in an EPR experiment by applying resonant microwave radiation in perpendicular orientation to the external magnetic field $\vec{B}$. For example in the picture of Figure 3.1a, the time-dependent oscillating magnetic field of the microwave $\vec{B}_1$ introduces a spin-flip from spin-down to spin up. In the present work, spin-flips in small-molecule compounds for OLED application are investigated. The previous chapter dealt with the formation of excitons in organic devices. Now, since these excitons are a bound state of an electron and a hole, both fermions, the resulting spin states are either a singlet or a triplet state. The arising inter-spin interactions for such particles are given in the section below.

3.2 Spin-Spin Interactions

If two neighboring spins, for example an electron and a hole on two molecular sites, form a bound state, an exciton, several interactions between these spins as well with their surroundings are possible. All interactions have an impact on the energy of the exciton. In general, the energy of a particle is given by the eigenvalue of the spin-Hamilton operator $\mathscr{H}$. It consists of several contributions and can be expressed as [73], [77], [78]:

$$\mathscr{H} = + \underbrace{\boldsymbol{g}\mu_B \boldsymbol{S}\vec{\boldsymbol{B}}}_{\substack{\text{Zeeman} \\ \text{interaction}}} - \underbrace{\boldsymbol{S}_a^T \boldsymbol{J} \boldsymbol{S}_b}_{\substack{e^-e^- \text{ exchange} \\ \text{interaction}}} + \underbrace{\boldsymbol{S}^T \boldsymbol{D} \boldsymbol{S}}_{\substack{\text{dipolar} \\ \text{interaction}}} + \underbrace{\boldsymbol{S}^T \boldsymbol{A} \boldsymbol{I}}_{\substack{\text{hyperfine} \\ \text{interaction}}} - \underbrace{\boldsymbol{g}_N \mu_N \vec{\boldsymbol{B}}^T \boldsymbol{I}_Z}_{\substack{\text{nuclear Zeeman} \\ \text{splitting}}} + \underbrace{\boldsymbol{I}^T \boldsymbol{Q} \boldsymbol{I}}_{\substack{\text{nuclear quadrupole} \\ \text{interaction}}} \tag{3.7}$$

The first term is the electronic **Zeeman interaction**, which describes an energetic splitting of spin carrying particles in an external magnetic field. The second and the third term are based on electron-electron interactions. **Exchange interaction** is determined by the isotropic exchange coupling parameter **J**, which couples two spins $\mathbf{S}_a$ and $\mathbf{S}_b$ by their Pauli repulsion. **Dipolar interaction** considers the interaction of a spin with the magnetic field of a neighboring spin. This results in an energetic splitting **D** even in the absence of an external magnetic field and is also called **zero-field splitting** (ZFS). The last three terms account for interactions with surrounding nuclei. **Hyperfine interaction** is the direct result of an additional net magnetic field generated by the magnetic moment **I** of a nucleus in the environment of a spin **S**. The nuclear Zeeman splitting and the nuclear quadrupole interaction are mentioned only for the sake of completeness and are neglected in the present study, since these are vanishingly weak in organics and especially at fields $B < 1\,\mathrm{T}$.

3.2.1 Exchange

From a classical point of view, if two particles with an electric charge are in close distance, an electrostatic force or repulsion acts on both of the particles, depending on the sign and the distance between them. Now, a typical quantum mechanical example is the hydrogen molecule when two electrons interact with two protons. In such a system it is not possible that the two electrons occupy the same quantum state within the quantum system due to Pauli exclusion principle [79]. Regarding the symmetry of the overall wave-function of these *indistinguishable* particles, the two-particle wave function of such a system is antisymmetric with respect to the exchange of electrons [80]. An interaction term arises which is of pure quantum mechanical nature, called the **exchange interaction**. In the spin Hamiltonian of Equation 3.7 this is taken into account with the term:

$$\mathscr{H}_{exch} = \mathbf{S}_a^T \mathbf{J}\, \mathbf{S}_b = \begin{pmatrix} S_{a,x} & S_{a,y} & S_{a,z} \end{pmatrix} \begin{pmatrix} J_{xx} & J_{xy} & J_{xz} \\ J_{yx} & J_{yy} & J_{yz} \\ J_{zx} & J_{zy} & J_{zz} \end{pmatrix} \begin{pmatrix} S_{b,x} \\ S_{b,y} \\ S_{b,z} \end{pmatrix} \tag{3.8}$$

where **J** is the exchange coupling tensor between two spins. It includes only electronic (Coulomb and Pauli) interactions and not the magnetic interaction of two paired spins

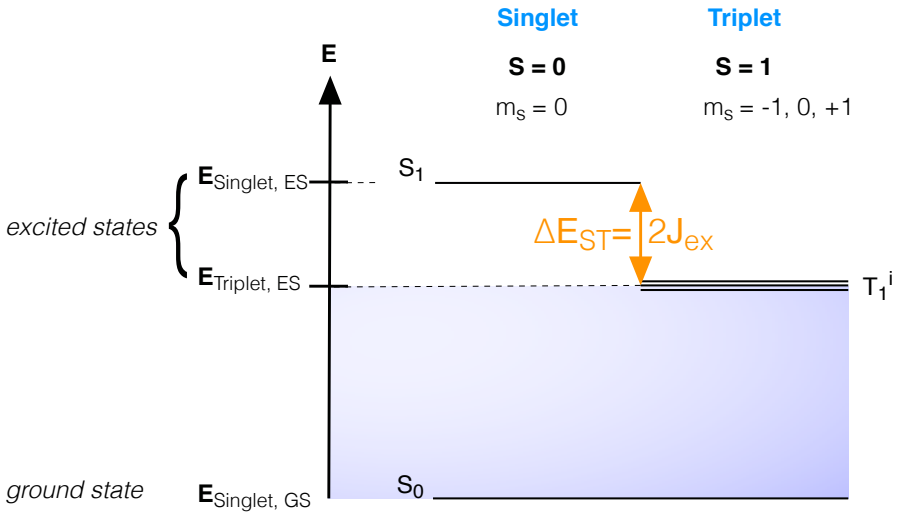

Figure 3.2: Energetic splitting between singlet and triplet states. It is determined by the strength and sign of the exchange interaction J_{ex}, here $J_{ex} < 0$.

(see Section 3.2.3). The energy of singlets E_S and triplets E_T in the system is then given by [25, 64]

$$E_S = S + C + J_{\text{ex}} \tag{3.9a}$$

$$E_T = S + C - J_{\text{ex}} \tag{3.9b}$$

where S is the overlap integral, C the coulomb repulsion integral, and J_{ex} the exchange integral.

$$S \equiv \int \phi_1(r_a)\phi_2(r_a)dr_a \tag{3.10a}$$

$$C \equiv \int\int \phi_1(r_a)\phi_2(r_b)\frac{e^2}{|r_b - r_a|}\phi_1(r_a)\phi_2(r_b)dr_a dr_b \tag{3.10b}$$

$$J_{\text{ex}} \equiv \int\int \phi_1(r_a)\phi_2(r_b)\frac{e^2}{|r_b - r_a|}\phi_1(r_b)\phi_2(r_a)dr_a dr_b \tag{3.10c}$$

where the integral over dr_i is an integral over space, ϕ_i the orbital wave-functions and r_i are the coordinates of the electrons. Assuming a small overlap S, we arrive at the origin of the singlet-triplet gap ΔE_{ST} combining Equation 3.9a and 3.9b [64, 66, 67]

$$\Delta E_{ST} = E_T - E_S \simeq 2J_{ex} \tag{3.11}$$

The direction of the energetic splitting still depends on the sign of the exchange integral J_{ex}. In the case of the hydrogen molecule H_2, the value of $J_{ex} > 0$, which lowers the singlet state. Now, in the present study the underlying molecules have a more com-

plicated orbital structure than the hydrogen molecule. Here, $J_{ex} < 0$ which lowers the triplet state (Figure 3.2). Thus, excitons in TADF compounds exhibit a small singlet-triplet splitting, if the exchange interaction of the hole located in the HOMO ϕ_{HOMO} and the electron in LUMO ϕ_{LUMO} is driven by a small spatial overlap between ϕ_{HOMO} and ϕ_{LUMO} [64].

3.2.2 Zeeman

The fact, that the electron spin interaction with an external magnetic field results in splitting was first shown by Pieter Zeeman in 1897 by observing a splitting in the optical spectra of doublet and triplet states in Cadmium [81]. It is the fundamental effect, which makes the investigation of spin states in EPR possible. In the spin Hamiltonian the electron Zeeman interaction (EZI) is described by

$$\mathscr{H}_{Zeeman} = \mathbf{g}\mu_B\mathbf{S}\cdot\vec{B}. \tag{3.12}$$

with $\mathbf{g}$ the electronic g-tensor, μ_B the Bohr magneton, $\mathbf{S}$ the spin operator and $\vec{B}$ the vector of the external magnetic field. The contribution to the total energy is given by the Eigenenergies of the Zeeman-term

$$\mathscr{E}_{|S,m_s\rangle} = m_s\cdot\mathbf{g}\mu_B\vec{B}. \tag{3.13}$$

with the magnetic quantum number m_s. In Section 3.1 it is shown, that in the case of a triplet, $m_s = -1, 0, +1$. This results in a spitting due to EZI into three energetic sub-levels. The Eigenenergies of the EZI for for triplets the states are:

$$\begin{aligned} \mathscr{E}_{|1,+1\rangle} &= (+1)\,\mathbf{g}\mu_B\vec{B} \\ \mathscr{E}_{|1,0\rangle} &= 0 \\ \mathscr{E}_{|1,-1\rangle} &= (-1)\,\mathbf{g}\mu_B\vec{B} \end{aligned} \tag{3.14}$$

The energetic splitting with increasing magnetic field is shown in Figure 3.3

The Electronic g-tensor

The electronic environment of a spin is covered by the electron g-tensor. For a free electron, which means no electronic interaction with the environment, the g-tensor is isotropic and reduced to the g-factor with the value of $g_e = 2.00231930436153$. Now,

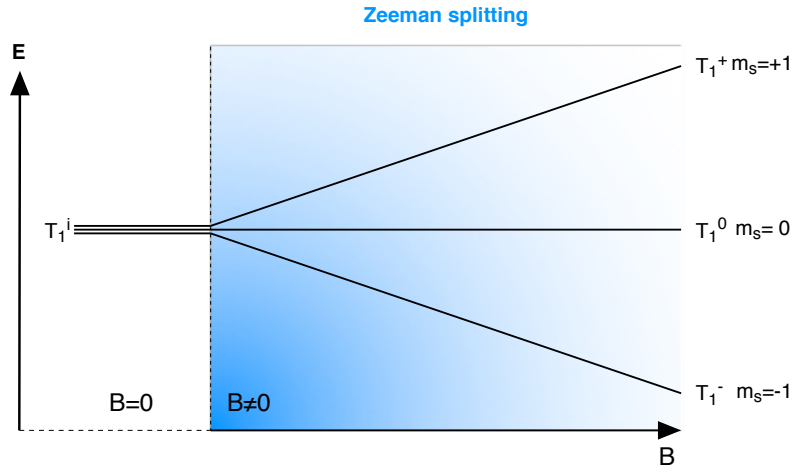

Figure 3.3: Energetic splitting between triplet sub-levels following Equation 3.14. With increasing magnetic field, the $m_s = -1$ and the $m_s = +1$ are shifted away from the central triplet state $m_s = 0$. The slope of the splitting is determined by the electronic g-factor.

interaction with the environment of the spin as spin-orbit coupling leads to anisotropy in the g-tensor. The g-tensor can be diagonalized

$$\mathbf{g} = \begin{pmatrix} g_{xx} & g_{xy} & g_{xz} \\ g_{yx} & g_{yy} & g_{yz} \\ g_{zx} & g_{zy} & g_{zz} \end{pmatrix} = \begin{pmatrix} g_{xx} & 0 & 0 \\ 0 & g_{yy} & 0 \\ 0 & 0 & g_{zz} \end{pmatrix} \tag{3.15}$$

and is then fully described by its diagonal components g_{xx}, g_{yy}, g_{zz}. In the special case of an exciplex triplet, it is possible that the two spins, which form the exciplex, have different g-factors. This would be a direct result of the environment of each spin, for example the HOMO of a donor molecule and the LUMO of acceptor molecule. In other words, each spin's g-factor may slightly deviate from the g-factor of a free electron g_e if the influence of its orbital environment is strong, e.g. if the spin-orbit coupling is strong. If the two independent spins S_a and S_b possess the g-factors g_a and g_b, then the difference $\Delta g = g_b - g_a$. From Equation 3.1, it can be derived that a difference in the g-factors directly implies different precession frequencies ω_L for each spin S_a and S_b, which is referred to as the Δg-*mechanism* [82],[83].

3.2.3 Dipolar

In systems with more than one unpaired spin, magnetic spin-spin interactions are possible. The fundamental principle behind these interactions is the magnetic dipole-dipole interaction between two dipoles. This interaction is independent from an external magnetic field and since it results in an energetic splitting at zero magnetic field,

it is also known as the *zero-field splitting* (ZFS) and shown in Figure 3.4. The splitting results from the magnetic interaction of one unpaired spin with another unpaired spin in close vicinity. For a particle with $S \geq 1$ the ZFS-term of the spin Hamiltonian is given by the anisotropic zero-field splitting tensor **D** [73]:

$$\mathscr{H}_{ZFS} = \mathbf{S}^T \mathbf{D}\ \mathbf{S} = \begin{pmatrix} S_{a,x} & S_{a,y} & S_{a,z} \end{pmatrix} \begin{pmatrix} D_{xx} & D_{xy} & D_{xz} \\ D_{yx} & D_{yy} & D_{yz} \\ D_{zx} & D_{zy} & D_{zz} \end{pmatrix} \begin{pmatrix} S_{b,x} \\ S_{b,y} \\ S_{b,z} \end{pmatrix} \tag{3.16}$$

If the tensor **D** is diagonalized, it can be expressed by the zero-field interaction parameters D and E:

$$\mathbf{D} = \begin{pmatrix} D_{xx} & 0 & 0 \\ 0 & D_{yy} & 0 \\ 0 & 0 & D_{zz} \end{pmatrix} = \begin{pmatrix} -\frac{D}{3} + E & 0 & 0 \\ 0 & -\frac{D}{3} - E & 0 \\ 0 & 0 & \frac{2}{3}D \end{pmatrix} \tag{3.17}$$

Then the axial term of the tensor in z-direction is given by D

$$D \equiv \frac{3}{2} D_{zz} \tag{3.18}$$

while the rhombicity is included in the parameter E

$$E \equiv \frac{1}{2}(D_{xx} - D_{yy}) \tag{3.19}$$

If both values are non-zero, they are measurable in an EPR experiment and deliver a fingerprint-feature in a typical EPR spectrum of a studied compound, which is discussed in more detail in Section 3.3. The classical magnetic dipole-dipole interaction depends on the distance vector $\vec{r}$ between two magnetic dipoles. From this point of view it is pretty obvious that the inter-spin distance dominates the interaction strength of the ZFS tensor **D**. The measurement of the ZFS-parameters in an EPR is a direct measure of the delocalization of the triplet extend $\vec{r_{ab}}$. The dependence of the ZFS of two spins S_a and S_b is given in frequency units by [84]:

$$D/h = \frac{\mu_0}{4\pi h} \frac{g_a g_b \mu_B^2}{|\vec{r}_{ab}|^3} (1 - 3cos^2\theta) \tag{3.20}$$

where μ_0 is the permeability constant, g_a and g_b are the g-factors of the spins S_a and S_b, $\vec{r}_{ab}$ the inter-spin distance and θ is the angle between $\vec{r}_{ab}$ and the external magnetic field $\vec{B}$.

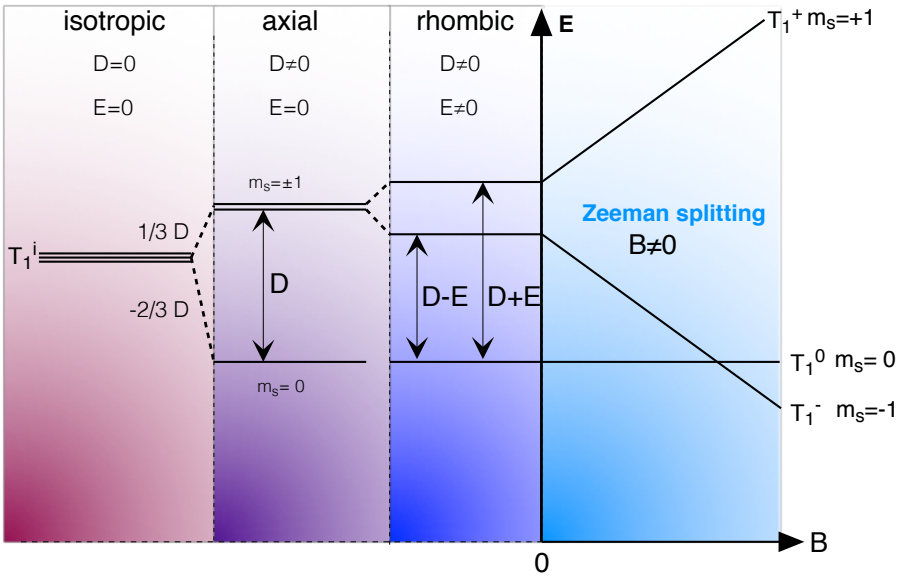

Figure 3.4: Energetic scheme of the zero-field splitting (ZFS) parameters D and E in triplet states. In absence of an external magnetic field the triplet sub-levels $m_s = 0$ and $m_s = \pm 1$ are split by the value D if the system exhibits an axial symmetry. The degeneracy of the $m_s = \pm 1$ is lifted if the symmetry is rhombic. Then the $m_s = \pm 1$ are further split by the parameter E.

3.2.4 Hyperfine

The counterpart of the electron-electron dipolar interaction is the hyperfine interaction (HFI). It involves the magnetic interaction of an electron spin with surrounding paramagnetic nuclei. Therefore, one has to take into account the magnetic nuclear spin of a nucleus I. A first example is the nucleus of a hydrogen atom. The proton possesses a nuclear spin of $I = 1/2$. A nearby electron spin can now interact with the magnetic field generated by the nucleus. The hyperfine spin-spin interaction term in the spin Hamiltonian is written in the same form as in the case of the electron-electron dipolar interaction. The dipolar tensor **D** is replaced by the hyperfine tensor **A** and additionally, a nuclear spin **I** appears instead of the second electron spin:

$$\mathscr{H}_{HFI} = \mathbf{S}^T \mathbf{A}\, \mathbf{I} = \begin{pmatrix} S_x & S_y & S_z \end{pmatrix} \begin{pmatrix} A_{xx} & A_{xy} & A_{xz} \\ A_{yx} & A_{yy} & A_{yz} \\ A_{zx} & A_{zy} & A_{zz} \end{pmatrix} \begin{pmatrix} I_x \\ I_y \\ I_z \end{pmatrix} \tag{3.21}$$

The hyperfine tensor can also be expressed in terms of its isotropic and anisotropic part [73]:

$$\mathbf{A} = A_0 \mathbf{1} + \mathbf{T} \tag{3.22}$$

where A_0 is the isotropic hyperfine coupling constant, $\mathbf{1}$ is a unit matrix and $\mathbf{T}$ is the anisotropic hyperfine matrix. The isotropic part is a direct measure of the Fermi contact interaction or in other words, the value of the wave function of the electronic spin at the nucleus [85]. The anisotropy is given by the dipolar magnetic interaction between the electron spin and the nuclear spin. A_0 can also directly be calculated by the trace of the hyperfine tensor $\mathbf{A}$ with $A_0 = tr(\mathbf{A})/3$. If the electron spin is surrounded by several nuclei, then a summation over all nuclei i is necessary:

$$\mathscr{H}_{HFI,i} = \sum_i \mathbf{S}^T \mathbf{A}_i \ \mathbf{I}_i \tag{3.23}$$

In the case of a triplet system with $S = 1$, the hyperfine interaction with a nucleus leads to a further splitting of the triplet sub-levels. The splitting depends on the interactions strength given by the HFI coupling constant A_0 (see Figure 3.5). The number n_{HFI} of hyperfine levels from i nuclei is given by the nuclear spin $\mathbf{I}$ as $n_{HFI} = (2 \cdot \mathbf{I} + 1)^i$. The magnetic quantum number of the nucleus $m_i = -I, ..., I$ specifies the nomenclature of the HFI sub-levels. The $m_s = 0$ sub-level remains degenerate.

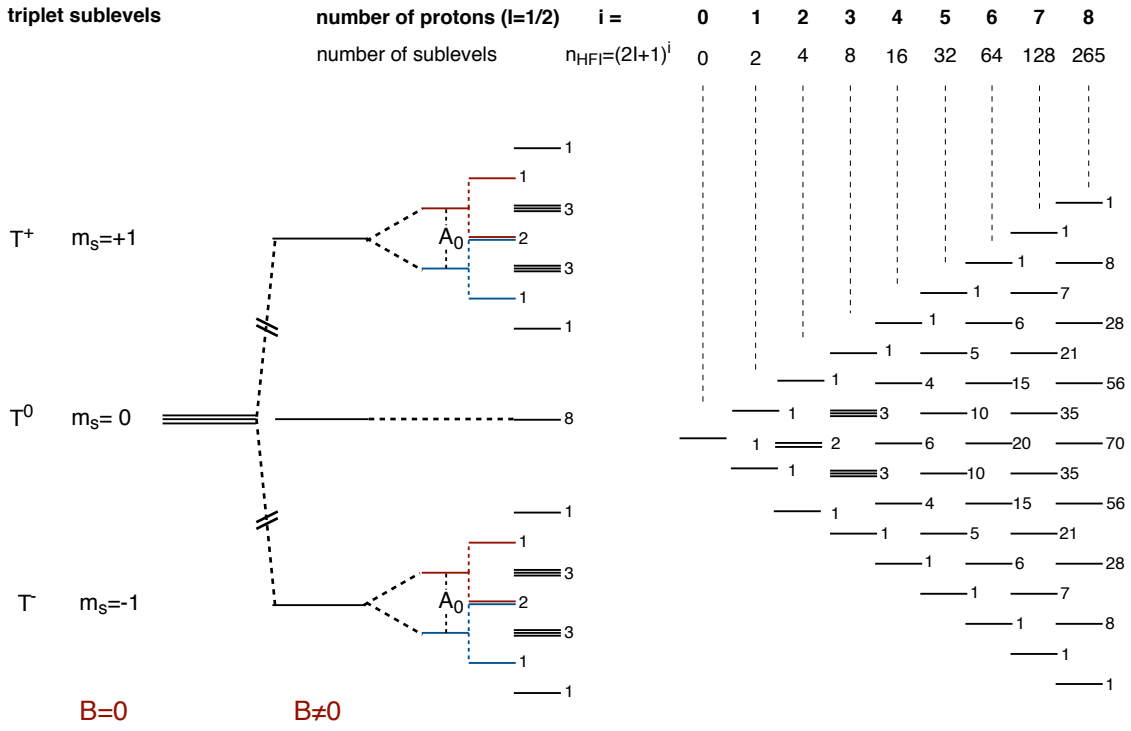

Figure 3.5: Energetic scheme of the HFI of hydrogen nuclei in a triplet state. The $m_s = \pm 1$ triplet sub-level are further split by the parameter A_0 for equivalent contribution of three hydrogen nuclei (left). For increasing numbers of interacting nuclei, the number of degenerate sub-levels is ruled by the binomial coefficients of the Pascal's triangle (right).

3.3 The Principle of Magnetic Resonance

Since now all relevant interactions have been discussed, which lead to several energetic splittings, the focus is now drawn to transitions between these energy states. A transition of a spin state between two energy states is realized by the involvement of an electromagnetic wave, or in more detail, a photon of the same energy as the energetic splitting of the spin state. The detailed demands and selection rules for absorption and emission of such a photon is discussed in the following. In this work magnetic resonance is applied only to systems with Spin $S = 1$ and with an exchange coupling constant $J_{ex} < 0$. Therefore, the following explanations will concentrate mostly on the principle of magnetic resonance in triplet states ($S = 1$). The basic principle, which makes an EPR transition possible in the first place is the electronic Zeeman interaction of these triplet states (Section 3.2.2). The triplet sub-level splitting due to this interaction at an exemplary magnetic field of $B_0 = 225\,\mathrm{mT}$ is in the range of several μeV. Now, an electromagnetic wave can be absorbed between these sub-levels if its energy is isoenergetic with the Zeeman splitting, that is, in the microwave range of the electromagnetic spectrum. For $B_0 = 225\,\mathrm{mT}$ the resonance frequency $\nu_{mw} = 6.3\,\mathrm{GHz}$ which is also the Lamor frequency (see Equation 3.1) of the system at this magnetic field value. The formula, describing the resonant transition frequency is the resonance condition [73]:

$$\Delta E = h\nu_{mw} = g_e \mu_B B_0 \tag{3.24}$$

If this condition is obeyed, an EPR transition is possible. In common EPR experiments usually the absorption or emission of resonant microwave radiation is detected under a change of the external magnetic field B_0. It is also possible to keep the external magnetic field B_0 at a constant value and sweep the frequency of the microwave radiation ν_{mw}. For absorption of a photon, the spin selection rules allow only changes of the magnetic quantum number m_s in the range of $\Delta m_s = \pm 1$, which is in the case of a triplet, a transition between $T_1^+ \leftrightarrow T_1^0$ and $T_1^0 \leftrightarrow T_1^-$. In addition, the intensity of the EPR signal is proportional to the population difference of the triplet sub-levels. This difference is a direct result of the equilibrium magnetic polarization. This spin-polarization is ruled by the Maxwell-Boltzmann distribution. If two levels have the energetic splitting ΔE at a given temperature T the population ratio of both levels is described by [73]:

$$\frac{n_1}{n_2} = \exp\left(-\frac{\Delta E}{k_B T}\right) \tag{3.25}$$

where n_1 and n_2 are the populations of the spin states and $k_B T$ is the thermal energy of the system. At a resonant frequency of $\nu_{mw} = 6.3\,\text{GHz}$ and an external magnetic field of $B_0 = 225\,\text{mT}$, this value is $n_1/n_2 = 0.99899$ at room temperature.

3.3.1 Total Magnetization and Bloch-equations

When conducting EPR experiments in the lab, the studied object is always a *macroscopic* sample. This implies that the interaction of the electromagnetic microwave field with the sample has to be described on a macroscopic scale. All spins in the sample are treated as an ensemble of magnetic moments $\vec{\mu}_i$ with the total magnetization vector $\vec{M}$. Without an external magnetic field, the direction of $\vec{M}$ is fixed and is given by the sum of the magnetic momenta of N individual spins μ_i

$$\vec{M} = \frac{1}{V}\sum_{i=1}^{N}\vec{\mu}_i \tag{3.26}$$

where V is the volume of the sample. If now an external magnetic field $\vec{B}$ is applied, the individual spins precess around the magnetic field vector (Figure 3.6a). Thus, the time-dependent magnetization $d\vec{M}/dt$ contains the net magnetization of the sample and is given by the equation of motion

$$\frac{d\vec{M}}{dt} = \gamma_e \vec{M} \times \vec{B} \tag{3.27}$$

where $\gamma_e = g\mu_B/\hbar$ is the electronic gyromagnetic ratio. If the external magnetic field is along the z-axis, then $\vec{B} = B_0$ and the equations of motion for each Cartesian direction is given by

$$\frac{dM_x}{dt} = \gamma_e M_y B_0 \qquad \frac{dM_y}{dt} = -\gamma_e M_x B_0 \qquad \frac{dM_z}{dt} = 0 \tag{3.28}$$

In an EPR experiment, the change of the precession of the total magnetization vector is induced by a second magnetic field, which is oscillating in time. The amplitude is B_1 and the direction is commonly perpendicular to B_0. Exemplary, for a circular B_1-field in x-y-direction the components are written as

$$B_{1x}(t) = B_1 cos(\omega_{mw} t) \qquad B_{1y}(t) = B_1 sin(\omega_{mw} t) \qquad B_{1z} = 0 \tag{3.29}$$

Now, for simplification, introducing a rotating coordinate frame is usefull. The reference frame is set to rotate around the z-axis with the Lamor frequency ω_L with $z = z'$. (Figure 3.6b). In this frame the magnetization vector appears stationary to the ob-

server. If then the microwave B_1-field is considered along the x'-axis in the rotating frame, the magnetization vector $\vec{M}$ undergoes a precession about the x'-axis. The frequency of this rotation is then the angular frequency $\omega_1 = g\mu_B B_1/\hbar$. Typical values for the magnetic fields are for example $B_0 = 0.3\,\mathrm{T}$ and $B_1 = 1\,\mu\mathrm{T}$. Thus it follows, that $\omega_1 << \omega_L$ [86]. In the experiment, in general, a sweep of the external magnetic field B_0 or the microwave frequency ω_{mw} of the B_1 field is considered. Then, $\omega_{mw} \neq \omega_L$ results for the non-resonant case. Due to interactions with the lattice, the spin system tends

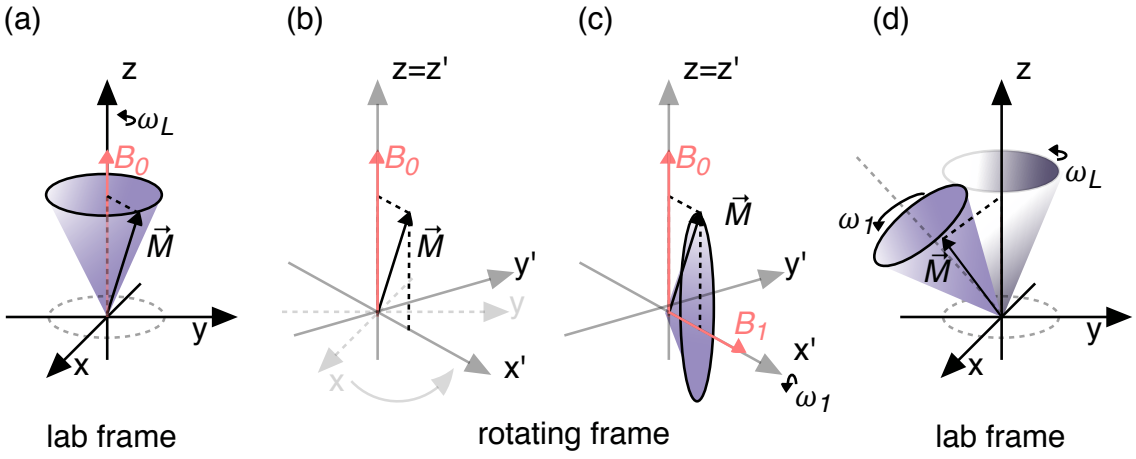

Figure 3.6: (a) The magnetization vector $\vec{M}$ is precessing around the external magnetic field in z-direction (B_0). The figure is shown in the lab-coordinate system x, y, z. (b) In the rotating frame approximation, the magnetization vector is fixed in space, while the coordinate system is rotating along the z-axis with an angular frequency corresponding to the Larmor frequency ω_L. (c) The microwave field B_1 also appears stationary along the x'-axis in the rotating frame x', y', z'. The magnetization vector $\vec{M}$ undergoes a precession about the x'-axis with an angular frequency ω_1. (d) Nutation of the magnetization vector in the lab frame with ω_1 and ω_L. Adapted from [86].

to relax to the equilibrium value of the magnetization M_0. The time constant for this relaxation process is given by T_1, the spin-lattice-relaxation time, or also the *longitudinal* relaxation time. The second relaxation effect is described by T_2, which accounts for the time constant of the *transversal* magnetization. The decay here is due to spin-spin relaxation and causes decoherence of the spin system. The Bloch equations in the rotating frame are then given with relaxation times [73]:

$$\frac{dM_{x'}}{dt} = -(\omega_L - \omega_{mw})M_{y'} - \frac{M_{x'}}{T_2} \tag{3.30a}$$

$$\frac{dM_{y'}}{dt} = (\omega_L - \omega_{mw})M_{x'} + \gamma_e B_1 M_z - \frac{M_{y'}}{T_2} \tag{3.30b}$$

$$\frac{dM_z}{dt} = -\gamma_e B_1 M_{y'} - \frac{M_z - M_z^0}{T_1} \tag{3.30c}$$

The Bloch equations are a set of coupled linear differential equations, which can be solved by a steady state approximation for continuous microwave field B_1. The steady-state solutions are given by [73]:

$$M_{x'} = -M_z^0 \frac{\gamma_e B_1 (\omega_L - \omega_{mw}) T_2^2}{1 + (\omega_L - \omega_{mw}) T_2^2 + \gamma_e^2 B_1^2 T_1 T_2} \tag{3.31a}$$

$$M_{y'} = +M_z^0 \frac{\gamma_e B_1 T_2}{1 + (\omega_L - \omega_{mw}) T_2^2 + \gamma_e^2 B_1^2 T_1 T_2} \tag{3.31b}$$

$$M_z = +M_z^0 \frac{1 + (\omega_L - \omega_{mw}) T_2^2}{1 + (\omega_L - \omega_{mw}) T_2^2 + \gamma_e^2 B_1^2 T_1 T_2} \tag{3.31c}$$

In addition, for small values of B_1, which is in principle the case for low microwave powers, the last term of the nominator, the saturation parameter, vanishes due to $s = \gamma_e^2 B_1^2 T_1 T_2 << 1$. One obtains, for example, for the y-direction of the magnetization vector M_y [86]:

$$M_y(\omega_L - \omega_{mw}) = (M_z^0 / B_0)) B_1 T_2 / [1 + (\omega_L - \omega_{mw})^2 T_2^2] \tag{3.32}$$

This solution is a *Lorentzian* function, which is, based on the assumptions made before, a proportional resonance response of an EPR experiment if a sweep of the microwave field ω_{mw} is considered, while B_0 and ω_L are kept at a fixed value. In other words, in this simplified picture, the linewidth of the Lorentzian curve is determined by the $1/T_2$. This is the case in the so-called linear regime, at low microwave power, or respectively small B_1-fields and no other spin-spin interaction considered. The linewidth is a *natural linewidth*, or also called **homogeneous** if it is only ruled by the T_2- decoherence time.

3.3.2 Linewidth Broadening Mechanisms

In the ideal case, all spins in the sample have the same spin-hamiltionion parameters and all spins are exposed to the same magnetic field. This picture leads to a homogeneous linewidth. However, in amorphous solid samples, the involved spins are randomly oriented and exposed to various interactions with other spin centers, which both causes different resonance frequencies w_L for each spin. In this case the linewidth is not homogeneous anymore. The spin species are not magnetically equivalent and therefore the linewidth appears *inhomogeneously* broadenend [73, 86]. The two possible lineshapes, the Lorentzian shape for the homogeneous case and Gaussian

for the inhomogeneous case, are depicted in Figure 3.7. In general, the homogeneous linewidth Γ_H depends on [73]

$$\Gamma_H = \frac{1}{T_2}(1+\gamma_e^2 B_1^2 T_1 T_2)^{\frac{1}{2}} \tag{3.33}$$

and is thus dependent on experimental conditions due to B_1. Note, that the parameter Γ_H is half the linewidth at half-maximum (HWHM). The various linewidth broadening mechanisms are discussed in the following section.

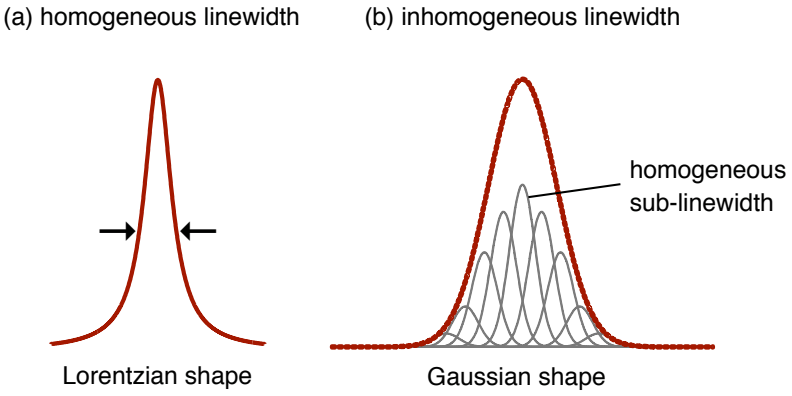

Figure 3.7: (a) The homogeneous linewidth exhibits a typitcal Lorentzian shape, often determined by the natural linewidth of the involved state. (b) The inhomogeneous linewidth is given by the superposition of several Lorentzian sub-resonances with a normal distribution of resonance frequencies. The normal distribution is leading to a Gaussian shape of the envelope linewidth. Adapted from [86].

Homogeneous Broadening

- **Lifetime broadening**
  The first Lorentzian shaped broadening mechanism is the so-called lifetime broadening. It is based on the quantum mechanical effect, that if a quantum mechanical system is changing in time, it is impossible to know the exact energy. The underlying phenomenon is the Heisenberg's uncertainty principle of time and energy $\Delta E \Delta t \geq \frac{\hbar}{2}$ [87, 88]. In other words, if a measurement of a quantum state demands the amount of time Δt, the standard deviation ΔE of the energy of the involved states exhibit a lower limit. This implies, there are no distinct energy states. In an EPR experiment the finite lifetime results in a Lorentzian linewidth, with the lifetime as the limiting parameter.

- **Power broadening**
  If the system is pumped heavily by high microwave power, the intensity of the

EPR signal is driven to saturation. In this case the linewidth is increased due to microwave power broadening, when the last term of the nominator in equation 3.31 is not vanishingly small [89, 90]. Then the high value of the B_1 contributes to the linewidth. In addition, the high microwave intensity leads to stimulated emission of the saturated spin states, due to high density of microwave photons in the sample. Subsequently, the lifetime of the involved spins is reduced and thus the linewidth increased.

Inhomogeneous Broadening

- **External magnetic field inhomogeneity**
  If the linewidth is ruled by inhomogeneous broadening, it consists of spins, which are not magnetic equivalent. Nevertheless, the signal could also seem to be broadened for magnetically equivalent spins if the external field is inhomogeneous over the spatial extend of the sample. Then only a fraction of the total spin ensemble is in resonance with the microwave field due to an inhomogeneous external magnetic field. The same fact needs to be considered for the B_1-field as well.

- **Dipole-dipole interactions**
  A high possibility of creating a shift in resonance frequency delivers the presence of dipolar interactions. Here, a spin influences another spin in close proximity due to its own magnetic moment. If the dipolar fields are random in direction, this causes a normal distribution of transition frequencies, since the local fields of each spin is slightly different [75].

- **Unresolved hyperfine interactions**
  The same argument as in the previous effect holds for the dipole-dipole interaction with various paramagnetic nuclei. Each nucleus generates a splitting of the resonance frequency. For a high number of HFI splittings the number of possible transitions increases enormously (see Figure 3.5). If the contributions are non-equivalent, the transition frequencies are randomized and not resolved in the EPR spectrum. The intensity of the individual sub-resonance lines is then ruled by a Gaussian distribution [73, 89].

- **Strains in Spin-Hamiltonian parameters**
  Finally, different spin centers may exhibit structural strains from the molecular disorder in the organic sample [78]. This effect is often observed in glassy

compounds or frozen solutions. Strain in the spin system can influence several parameters in the Spin-Hamiltonian resulting for example in D-strain [91] or a g-strain [92, 93]. Here, it is noteworthy, that a g-strain is connected to a line broadening with increasing magnetic field, since the g-factor is proportional to the slope of the Zeeman-interaction (see Section 3.2.2).

3.3.3 Simulation of Triplet Spectra

The absorption profile or in other words the magnetic resonance spectrum for example for a EPR transition is a Lorentzian profile (Figure 3.8a). Now, if a spin-pair on an organic molecule exhibits various spin interactions, this leads to several energetic splittings as explained in the previous section. All these interactions produce specific observable features in the magnetic resonance spectrum. A typical triplet spectrum of an organic film with an exemplary ZFS of $D = 100\,\mathrm{MHz}$ is shown in Figure 3.8b. The line shape of the absorption spectrum is more complex than a simple Lorentzian profile. It consists of a superposition of several absorption lines with different molecular orientation, also called a powder spectrum. The molecular orientation of a spin within an organic film results in an angular dependence of the zero field splitting parameters [73]:

$$D = D_0 \left(cos^2(\theta) - \frac{1}{3} \right) \tag{3.34}$$

$$E = E_0 \cdot sin^2(\theta) \cdot cos(2\phi) \tag{3.35}$$

with θ as the polar angle between the external magnetic field B_0 and the orientation of the molecular axis z and ϕ the azimuthal angle. The powder spectrum is the superposition of spectra for all orientations. The shoulders in Figure 3.8b are determined by $2D$ at a polar angle of $\theta = 0°$ and $\theta = 180°$, while the spikes in the spectrum are given by a separation of D at a polar angle of $\theta = 90°$. This fact makes EPR a powerful tool for studying organic triplet spectra, since interaction parameters can directly be read off from the spectrum if the peak positions are clearly resolved. In addition to the dipolar coupling, for some organic compounds a nearby nucleus further splits the observed features of the line shape. An interaction with a nucleus of $I = 1$ like a nitrogen atom results in an additional three-fold energetic splitting of the triplet sub-levels. Figure 3.8c shows a simulation of a triplet powder spectrum with an additional isotropic hyperfine interaction strength of $A_0 = 20\,\mathrm{MHz}$. While in the case without any hyperfine interaction in Figure 3.8b the dominant triplet peaks are nicely resolved, a splitting of the peaks and the shoulders is observable in 3.8c.

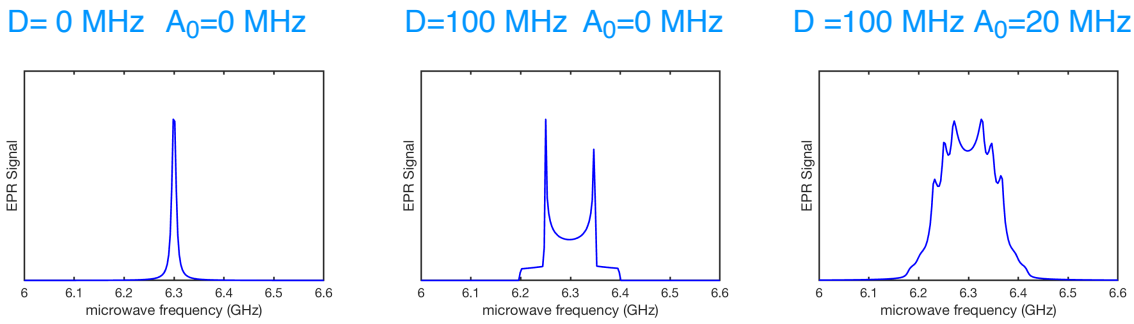

Figure 3.8: Simulation of frequency swept EPR absorption spectra in a triplet spin system $S = 1$. The resonant magnetic field is set to $B_0 = 225\,\text{mT}$ with a resonance frequency of $\nu_{mw} = 6.3\,\text{GHz}$ and a homogeneous linewidth of $\Gamma_H = 5\,\text{MHz}$. Graph (a) exhibits no ZFS interaction ($D = 0\,\text{MHz}$) and no hyperfine interaction ($A = 0\,\text{MHz}$). The spectrum in (b) shows the powder spectrum of a triplet with $D = 100\,\text{MHz}$ with random molecular orientation with respect to the magnetic field axis. (c) In addition to (b), isotropic HFI with one nucleus of $I = 1$ and interaction strength $A_0 = 20\,\text{MHz}$ is simulated. Simulations have been performed with the Matlab tool EasySpin [78].

3.3.4 Electroluminescence Detected Magnetic Resonance - Theory

A standard EPR experiment is conducted by keeping the microwave radiation at a fixed frequency ν_{mw} and sweeping the external magnetic field B_0. The observation of the spin resonance is usually realized via detection of the intensity of microwave absorption of the investigated spin system. In this work, the focus is on light emitting compounds, therefore it is desirable to detect the spin states optically. Furthermore, a magnetic resonance study of the electroluminescence (EL) from electrically driven devices is beneficial since, in particular with TADF materials, the up-conversion from triplet states to emitting singlets can be observed. The triplet states of the investigated systems are sensitive to the magnetic field, as explained in Section 3.2.2. The triplet sub-levels split in an external magnetic field and resonant microwave radiation with frequency ν_{mw} is able to induce transitions between these sub-levels. The change of triplet sub-level population can indirectly be observed by detecting the EL during a sweep of the magnetic field. This special form of spin resonance bears the name electroluminescence detected magnetic resonance (ELDMR). A detailed schematic of the transitions involved in generating the ELDMR signal is shown in Figure 3.9. When the spin system is electrically operated, a ratio of 1:3 for singlets to triplets is established in equilibrium with $B_0 = 0$. Then, a fraction of the triplets decays non-radiatively via k_{nr}, while in TADF OLEDs ideally the majority of the triplet population undergoes RISC via k_{RISC}. Now, under resonance condition a new equilibrium state of triplet population is generated by stimulated emission and microwave absorption. That results in a change

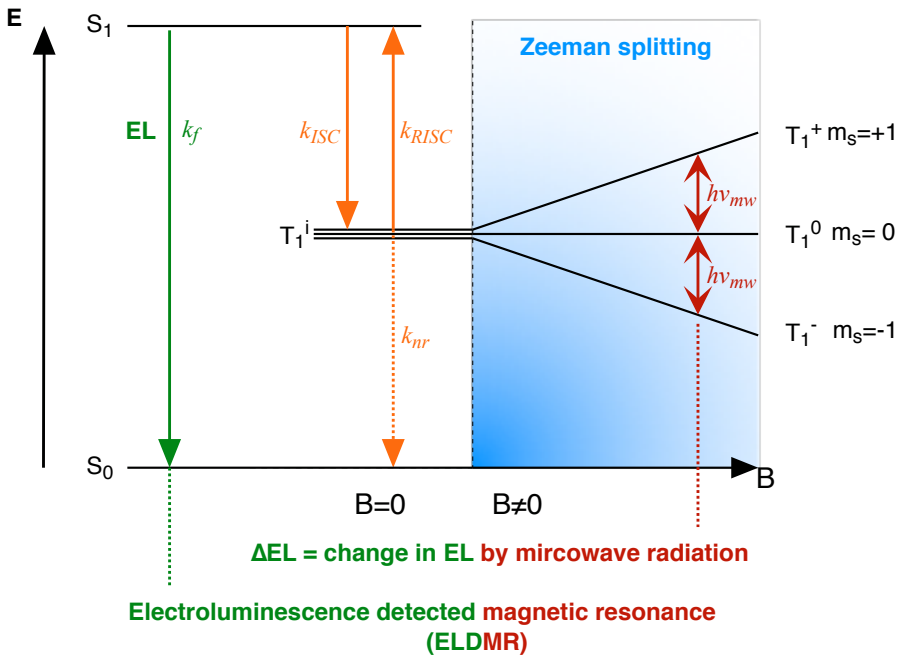

Figure 3.9: Dominant transitions in ELDMR. Microwave radiation (red arrows) of a fixed frequency is applied ν_{mw} to drive transitions between triplet sub-levels T_1^+, T_1^0, T_1^-. In resonance the transition rates of reverse intersystem crossing k_{RISC} and triplet non-radiative decay k_{nr} is slightly changed, leading to a change of electroluminescence ΔEL compared to off-resonance.

of the rate constants k_{nr} and k_{RISC}. A change in both rates will alter the quantum yield of the singlet state and change the intensity of the EL by the amount of ΔEL compared to the off-resonance case. The change of the EL is defined as $\Delta EL = EL_{on} - EL_{off}$, the difference between the on-resonance value EL_{on} and the off-resonance EL_{off}. Both parameters, EL_{on} and EL_{off}, depend on the number of excitons generated by current injection. For this reason, the relative change is often specified, also denoted as ELDMR contrast:

$$\frac{\Delta EL}{EL} = \frac{EL_{on} - EL_{off}}{EL_{off}} \tag{3.36}$$

3.3.5 Hole Burning Spectroscopy - Theory

If deeper insight into broadened magnetic resonance spectra is desired, it is advisable to conduct a so-called hole burning experiment [94, 95]. The idea behind this experiment is to irradiate the spin system with a second microwave frequency, denoted as *pump* frequency ν_{pump}. If the systems linewidth is for example relaxation-broadened, the entire line is influenced. In other words, the line profile is therefore compressed compared to the undisturbed spectrum (see Figure 3.10a). If the power of ν_{pump} is chosen as high as possible, the whole line may disappear. In contrast, if the spin system

is broadened by orientation disorder, only a fraction of the total spins is resonant to ν_{pump}, while the other spins have different resonant frequencies and are non-resonant to ν_{pump}. Only the portion of the line that comes from these spins, can also be saturated. The resulting shape is a *hole* in the undisturbed spectrum (see Figure 3.10b). The linewidth of the hole then corresponds to the homogeneous linewidth.

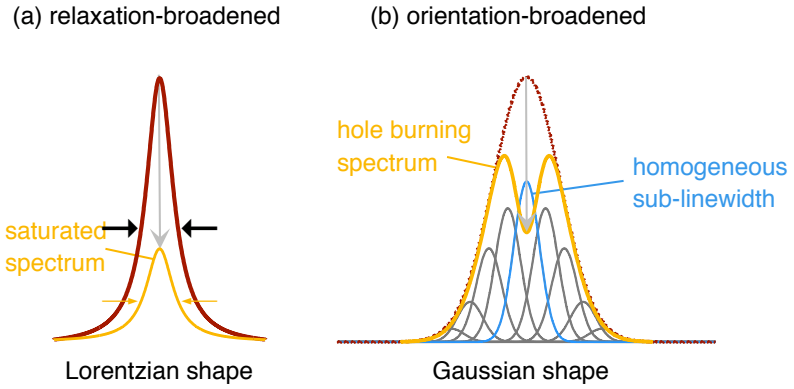

Figure 3.10: (a) A relaxation broadened spectrum is compressed in a hole burning experiment. (b) An orientation broadened spectrum is resulting in a hole in the inhomogeneously broadened spectrum (red). The hole burning spectrum (orange) is obtained, when a single frequency is burned out of a distribution of transition frequencies.

4 Experimental Section

Since the previous two chapters explained all the fundamental theoretical details of organic semiconductors and spin resonance, the focus is now on the realized experiments. At first a short overview is given on the device fabrication, followed by the j-V-EL characterization, device efficiency and time-resolved electroluminescence. Finally, the setup for spin resonance experiments applied to fully working devices is introduced in detail.

4.1 Device Fabrication

For successful fabrication of any device based on organic layers, it is crucial to apply deposition techniques that allow precise adjustments of the thickness of the organic layer, while maintaining the energetic impact on the molecule as low as possible to prevent degradation of the molecule. In the past years of OLED research, the method of choice developed for device fabrication of small molecules is the physical vapor deposition under high vacuum ($p \leq 1.0 \cdot 10^{-6}$ mbar). In contrast, polymers are commonly solution processed by spin coating. In general, the device fabrication starts with an indium tin oxide (ITO) covered glass substrate. The size of the glass substrate is usually 13 mm×13 mm. The huge advantage of ITO is a high transparency, while keeping the sheet resistance at a low value of $10^{-4}\,\Omega$cm [57]. To define an active area of the device, two contact stripes are etched into the ITO layer by photo lithography. The width of the remaining ITO stripes is $3\,mm$ (see Figure 4.1a). The standard cleaning procedure is applied after lithography. The substrates are cleaned 10 minutes each in water, acetone and isopropanol and finally exposed to oxygen plasma for 30 s. As a next step, the hole injection layer (HIL) is fabricated. Depending on the used compound, this layer is either solution processed or evaporated. In the case of the standard water-based polymer PEDOT:PSS the spin coating technique is applied at 3000 rotations per minute (rpm) with a ramp time of 1 s and a duration of 60 s. PEDOT:PSS is highly soluble in water, which excludes the use of toxic solvents like chlorobenzene. After spin coating PEDOT:PSS, the substrates are annealed at 130 °C to completely evaporate the remaining water in the film and to fully polymerize the HIL. Subsequently, the substrate is

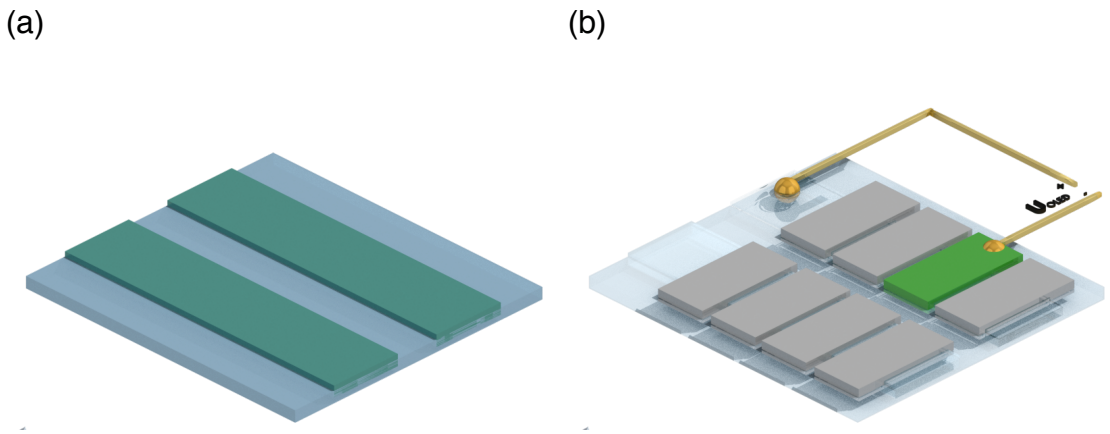

Figure 4.1: Fabrication of an OLED device. (a) An indium tin oxide (ITO, green) covered glass is used as a substrate. Two stripes are etched by photolithography to define an active area of the device. (b) The organic layers and top electrodes are evaporated on top through a shadow mask. By selectively contacting one of the processed OLED cells on the ITO (anode) and the aluminum stripe (cathode), the device is emitting. Light out-coupling is generated at the bottom of the substrate.

placed into the evaporation chamber for physical vapor deposition. Here, the active area of eight devices are formed by the evaporation of the organic material through a shadow mask. The resulting structure is shown in Figure 4.1b. Each organic material needed for a specific layer is filled in a crucible. The crucible is heated upon evaporation of the material at around 1 Å/s. The evaporation rate is measured by a quartz oscillator which is placed above the hot crucible. In order to realize co-evaporation, two materials are placed at opposite positions in the chamber. Note, that the measured evaporation rates may differ, since both quarz oscillators may be influenced by the second material source. The substrates are placed in a rotating substrate holder above the organic sources. As a top electrode in this work a thin 5 nm layer of Calcium (Ca) is followed by 120 nm Aluminum (Al). The evaporation rates are 0.2-0.3 Å/s for Ca and 1-3 Å/s for Aluminum. Since the layer structure of the organic layers is not the same in the different parts of this theses, the details on the layer structures are given in the corresponding chapter.

4.2 Experimental Access to OLED Efficiencies

To obtain the typical OLED parameters like j-V-EL-characteristics, electroluminescence spectrum or the EQE, which have been introduced in Section 2.2, the device needs to be electrically operated by an external voltage source. For simultaneous measurement of the current and electroluminescence response under a constant voltage sweep in time, a precision semiconductor parameter analyzer (Agilent 4155C) is used. The following

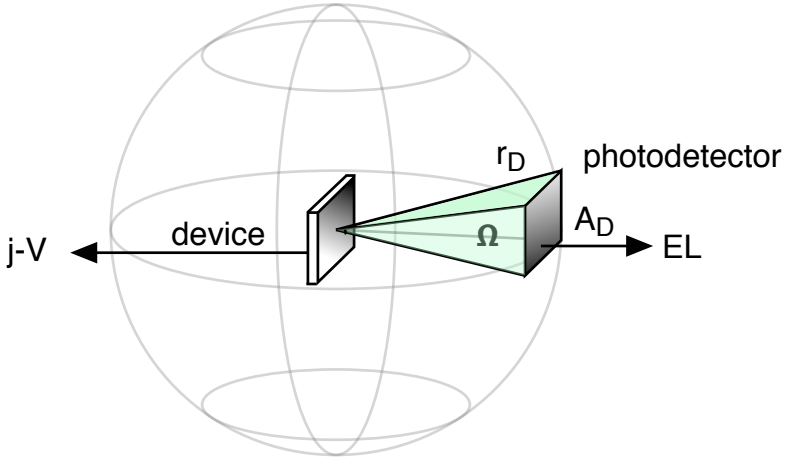

Figure 4.2: Measurement of the j-V-characteristics and EQE. If the device is placed next to a photodetector with a known distance r_D, detector area A_D and detector efficiency η_D, then the total photon flux Φ_0 of the OLED device can be estimated by the amount of photons passing the solid angle Ω. In this approximation of the EQE, the device is treated as a point source.

considerations are also found in [96]. The photodetector is placed in close proximity at a known distance r_D (Figure 4.2). This geometry allows the measurement of the EQE under the following considerations: (i) the emission of the device is treated as a point source (ii) all photons are emitted from the device into a hemisphere (iii) the detected photon flux Φ_D at the detector is proportional to the total amount of photons Φ_0 exiting the device along the distance vector r in direction of the photodetector. The number of photons is measured by the photocurrent of the photodetector I_D. Together with the efficiency of the detector η_D this results in $\Phi_D = I_D/e\eta_D$. The fraction of all photons reaching the detector is given by the solid angle Ω. The solid angle can be calculated by the area of the detector A_D and the distance between the detector and the emitting device as $\Omega = A_D/r^2$. The total photon flux of the device directly above the device is then given by

$$\Phi_0 = \frac{\Phi_D}{\Omega} = \frac{r^2 I_D}{e\eta_D A_D} \tag{4.1}$$

An integration of the hemisphere yields an additional factor of $2\pi \cdot \frac{1}{2}$ if a Lambert emission is assumed. The total photon flux containing all photons from all directions $\Phi_{\text{tot}} = \pi\Phi_0$. The EQE was introduced in Section 2.2 as the number of photons exiting the device per injected electron. With the aforementioned geometric considerations, the j-V-EL-measurement delivers a good estimate of the EQE by:

$$\eta_{\text{ext}} = \frac{e\Phi_{\text{tot}}}{I_{\text{OLED}}} = \frac{e\pi\Phi_0}{I_{\text{OLED}}} = \frac{\pi r^2 I_D}{\eta_D A_D I_{\text{OLED}}} \tag{4.2}$$

4.3 Time-Resolved Electroluminescence

The devices in this work are based on the mechanism of thermally activated triplet upconversion leading to delayed fluorescence (see Section 2.4). Hence, it is advisable to examine the devices in a time-resolved manner. In addition, an evaluation of the temperature dependence is also desirable. The method of choice, which combines both requirements, is here temperature-dependent transient EL. This technique combines the possibilities of observing the temporal course of the electroluminescence while successively increasing the temperature. This makes it possible to visualize the thermal activation of the delayed fluorescence directly in the device. The geometric arrangement from Section 4.2 can be used for this measurement. A photo detector is placed next to the device at a known distance r_D. Now, instead of a parameter analyzer, a pulsed voltage source is used to generate a rectangular voltage signal of $\Delta t = 1\,\mathrm{ms}$ duration and $V_{\mathrm{on}} = 10\,\mathrm{V}$ amplitude (see Figure 4.3). The intensity of the Electroluminescence is measured by the photodetector (Hamamatsu S2281) and recorded with a digitizer card (GaGe CompuScope), which works as an oscilloscope. The digitizer card is triggered directly by the voltage pulse generator to start the measurement at the onset of the voltage at $t = t_{\mathrm{on}}$. After switching on, the device is gradually filled with charge carriers

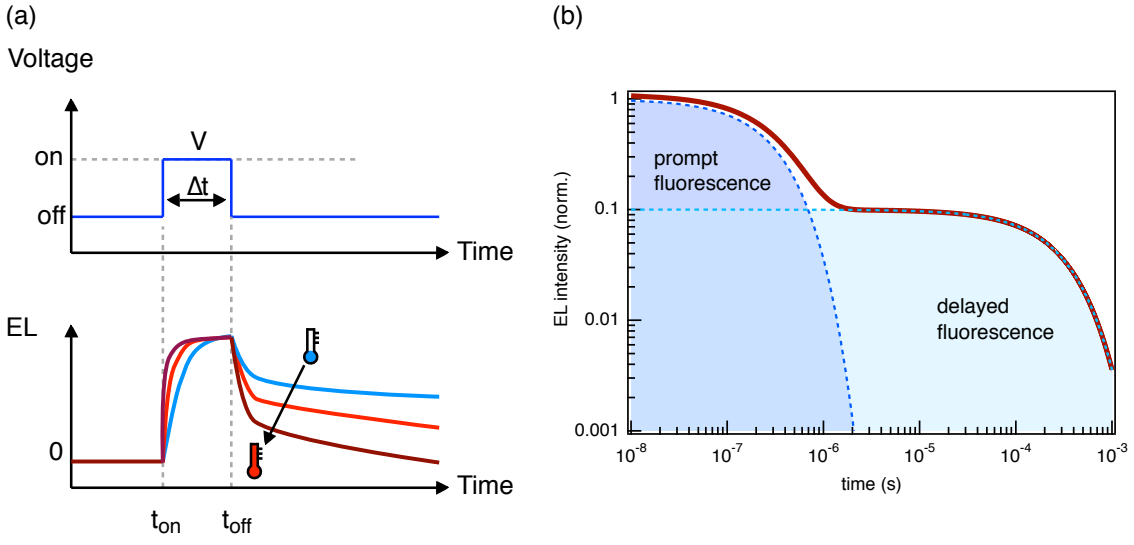

Figure 4.3: (a) Measurement of temperature-dependent transient electroluminescence (trEL). A pulsed voltage of duration $\Delta t = 1\,\mathrm{ms}$ is applied. The integral electroluminescence is measured via a photodetector. The lifetimes decrease with increasing temperature. (b) Ideal bi-exponential decay of a TADF system (red curve). The prompt component (dark blue curve) is shown with a time constant of τ_{pr} =ns and the delayed component (light blue curve) with $\tau_{\mathrm{TADF}} = \mu$s according to Equation 4.3

and the emission increases. After an almost constant current flow is reached, the EL

saturates (see Fgiure 4.3,a dark red curve). The pulse duration Δt, must be adjusted so that the EL reaches a plateau before the device is switched off at $t = t_{\text{off}}$. The decay of the electroluminescence after the switch-off process is the important part for TADF systems. Singlet states usually decay via prompt fluorescence after a few hundred nanoseconds. Whereas the time constant for the afterglow due to the delayed fluorescence is in the microsecond range. Ideally, both the prompt and delayed component are described by an exponential decay [64]

$$I(t) = A \cdot \exp\left(-\frac{t}{\tau_{\text{pr}}}\right) + B \cdot \exp\left(-\frac{t}{\tau_{\text{TADF}}}\right) \tag{4.3}$$

where A, B are the magnitudes of the prompt and delayed component, τ_{pr} and τ_{TADF} are the the respective lifetimes. Figure 4.3 shows the theoretical course of an ideal time decay of a TADF system after excitation with τ_{pr} =ns and $\tau_{\text{TADF}} = \mu$s. To examine the temperature response of a TADF device, the trEL measurement is conducted at several temperatures. Therefore, the device is in thermal contact with a copper block, which is mounted onto a Peltier element cooler (Peltron PRG H100). Here, the temperature can be controlled within a temperature range of 244 K - 309 K. To prevent influences from ambient light and oxygen quenching, the measurements are done under constant nitrogen flow in a blackened box.

4.4 Magnetic Resonance in Organic Semiconductor Devices

In the following, the experimental realization of spin resonance on organic semiconductor devices is presented. The experimental components required for this are an electromagnet to generate the magnetic B_0-field, a microwave stripline to guide the microwaves to the sample and a sample holder to attach and contact the sample. Finally, it still needs the components for the electrical operation of the OLED and optical detection.

Magnetic Field

In order to apply a magnetic field of values between for example up to 1 T for EPR, typically electro-magnetic coils are used. Here, a high current in the coils of several tens of amperes is generating the magnetic field perpendicular to the coil plane. In this work, a modified Bruker Spectrometer (Bruker ESP300) is used for B_0. A sketch of the coils is shown in Figure 4.4. The magnet is designed so that the magnetic field is as homo-

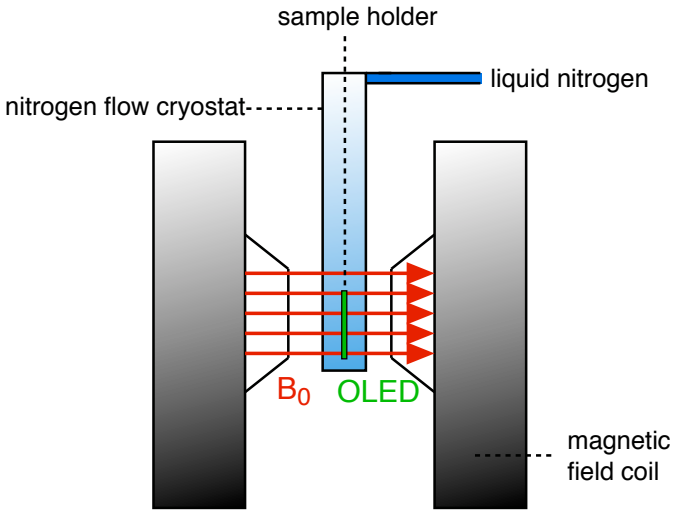

Figure 4.4: The generation of the magnetic field B_0 (red arrows) via a modified Bruker Spectrometer. The sample (green) is placed in a nitrogen flow cryostat(blue), fitting between the magnetic field coils(black). The magnetic field B_0 is homogeneous over the sample volume.

geneous as possible in the area between the pairs of coils. For a magnetic field sweep, a successive current ramp is run in each case, which then enables a semi-continuous sweep of the magnetic field. Between the two magnetic field coils, a nitrogen flow cryostat (Oxford) is mounted to allow temperature dependent measurements of ELDMR. The temperature is monitored by a temperature Controller (Lakeshore 335).

Microwave Stripline

In a standard EPR experiment the microwaves coupling into the sample is usually generated by a microwave cavity. There, a maximum of the magnetic B_1-field is formed directly at the sample by standing waves at a resonant frequency of the cavity. Unfortunately, the resonance properties of the cavity are severely influenced when studying devices in the center of the cavity. In addition, the limited space in the cavity requires a special minimalist design of the devices, so that standard OLEDs cannot be used. In order to maintain comparability with standard OLED devices, an alternative concept for microwave coupling is applied in this work. The microwaves are guided into a so-called non-resonant stripline, which, simply put, is a thin conducting metal stripe on a dielectric substrate with a conducting bottom side (Figure 4.5). The electromagnetic wave is traveling in the dielectric layer between the stripe on the top and the backside contact. The magnetic B_1-field is circled around the metal strip. If an OLED device is placed on top of the stripline, the B_1-field is directly coupled into the device. By applying this method, a major advantage is having access to a broadband frequency range,

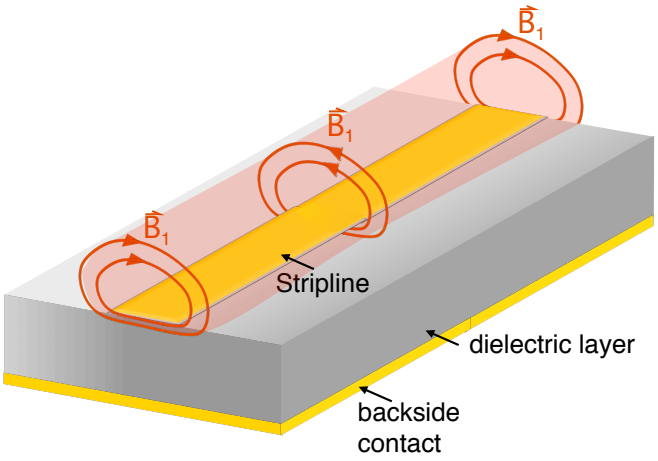

Figure 4.5: The concept of microwave coupling: a non-resonant stripline, consisting of a metal stripe on top and a backside contact. The dielectric layer confines the electric field inbetween the top and the bottom contact. The magnetic B_1-field is circular around the top electrode. OLED devices are placed on top of the stripline in order to generate sufficient values of B_1-field in the sample.

instead of being fixed to one resonance frequency like in the case of a resonant cavity. This allows multi-frequency studies at any desired resonance position. The frequency range of the setup is optimized up to a resonant frequency of $\nu_{mw} = 40\,\text{GHz}$.

4.4.1 Electroluminescence Detected Magnetic Resonance - Setup

While the theory of ELDMR was introduced earlier in Section 3.3.4, the focus is now on the experimental details of this advanced version of electron spin resonance. The method is primarily intended to analyse fully processed devices. This results in the necessity to centre these devices in the centre of the magnetic field coils (Figure 4.4) and still allow for electrical contacting in the cryostat. This task is performed by a sample holder, which forms a unit together with the microwave stripline (Figure 4.5) and holds the sample in place. A general overview of the whole setup is shown in Figure 4.6. The metal stripe of the stripline also functions as the cathode contact for the OLED sample, as the glass substrate is attached upside down, with the aluminium contacts of the device touching the stripline. The anode contact is realized by flexible pins, which are pressing against the ITO surface of the device. To operate the device a source measure unit (SMU, Keithley 237) is connected to the stripline and the pins. If not stated otherwise, the SMU delivers a constant current. A microwave signal generator (Anritsu MG3694C) can be used to apply microwave radiation from 8 MHz up to

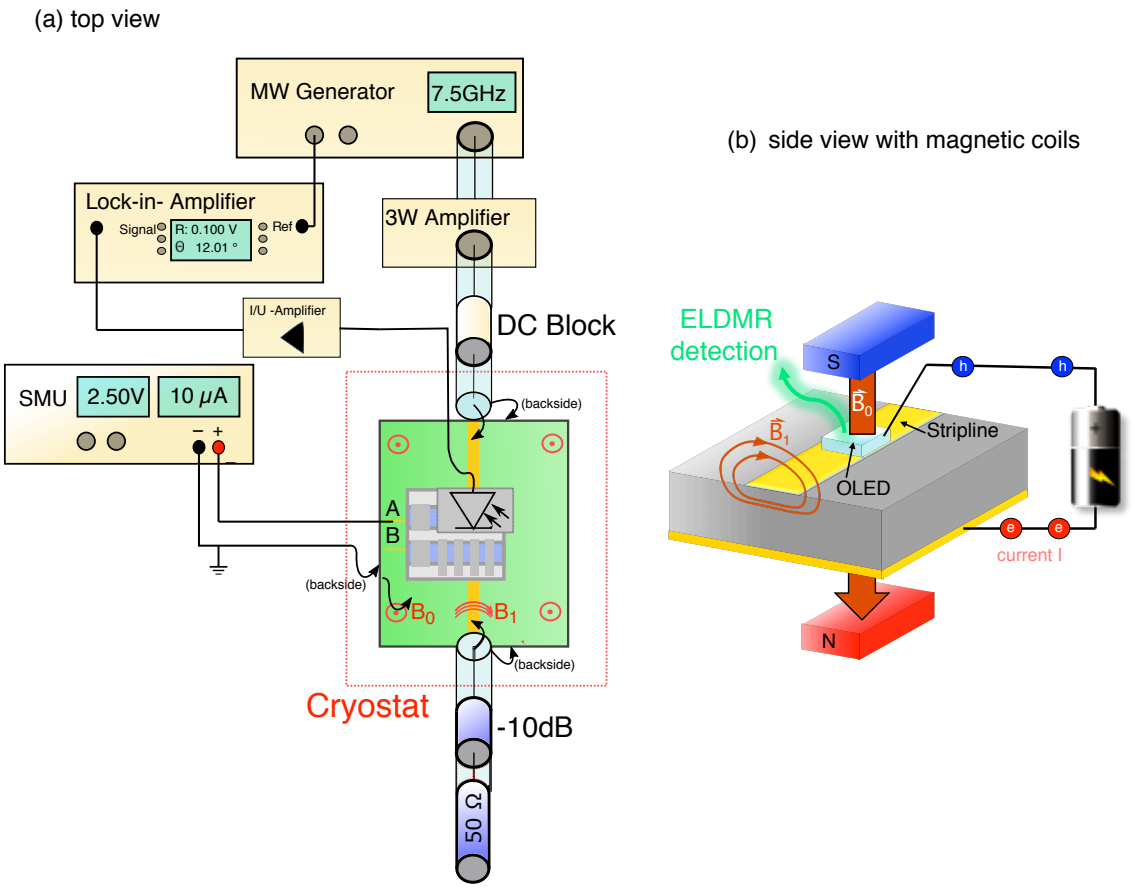

Figure 4.6: Sketch of the ELDMR setup. (a) The stripline is placed into a cryostat (red dotted) between two magnet coils, which generate the B_0-field (red circles). The B_1-field is depicted by the red arrows above the stripline. OLEDs on the stripline are operated by a source-measure unit (SMU). The electroluminescence is detected by the amplified photo-current of a photo diode (I/U-amplifier). Lock-In-detection of this signal is realized by chopping the microwaves at a TTL-frequency of ~ 1 kHz. (b) Sketch of the orientation of the B_0-field versus the B_1-field.

40 GHz, operating at a maximum output power of 20 dBm. To increase the B_1-field at the sample, the microwaves are amplified by a 3W-amplifier. To decouple the DC current from the microwave components, a DC-block is inserted between the stripline and the amplifier. The electroluminescence is detected by a photo detector (Hamamatsu Si photodiode S2387-66R), followed by a current/voltage amplifier (Femto DLPCA-200). The amplified signal is measured by a lock-in amplifier (Signal Recovery Model 7265). The lock-in amplifier is locked by a TTL-pulse at a modulation frequency of around $\nu_{\mathrm{mod}} = 1\,\mathrm{kHz}$, which is given by a pulse generator (Keithley3390). The spin system is modulated by the same pulse generator by chopping the microwave generator at the same frequency ν_{mod} via on-off-modulation. During an ELDMR measurement, usually a fixed frequency is chosen, while the magnetic B_0-field is swept across the resonance position. With the stripline setup, it is also possible to perform mircowave sweeps at

a fixed magnetic field, which is then called frequency swept ELDMR. This is a huge advantage compared to the cavity method and an important step on the way to hole burning spectroscopy, which is explained in the next section.

4.4.2 Hole Burning Spectroscopy - Setup

Only minor changes need to be done to the aforementioned ELDMR setup for hole burning spectroscopy. The idea of this measurement technique is introduced in section 3.3.5. A second microwave generator (Windfreak V1) is used as pump source, in order to pump the spin system at a specific microwave frequency ν_{pump}. Since the pump generator is supposed to drive certain spin transitions into saturation, it is advantageous, also to use a microwave amplifier for the second microwave generator. A high power combiner is attached to both outputs of the microwave amplifiers, to feed both microwave fields into the stripline. There are two possible detection methods

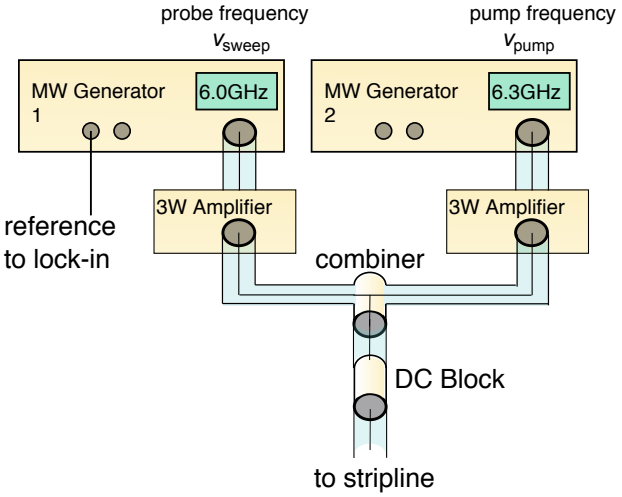

Figure 4.7: Sketch of the extension of the setup for hole burning spectroscopy. A second microwave generator is attached to the microwave axis by a high power combiner. This generator works as a pump frequency generator ν_{pump}, which pumps the investigated spin system during a sweep of the first generator.

available, depending on which microwave generator is modulated. In the first method, a ELDMR frequency sweep is performed, by on-off-modulation of the sweep generator. This experiment is expected to detect the ELDMR spectrum, except the transition, which is saturated by ν_{pump}. The second method is supposed to detect the saturated transiton directly by on-off-modulation of the pump generator. In other words, this method direcly probes the hole spectrum, which is caused be the pump frequency.

5 Influence of Donor–Acceptor Dihedral Angle on Exciton Kinetics and Singlet–Triplet Gap in Deep Blue Thermally Activated Delayed Fluorescence Emitter [1]

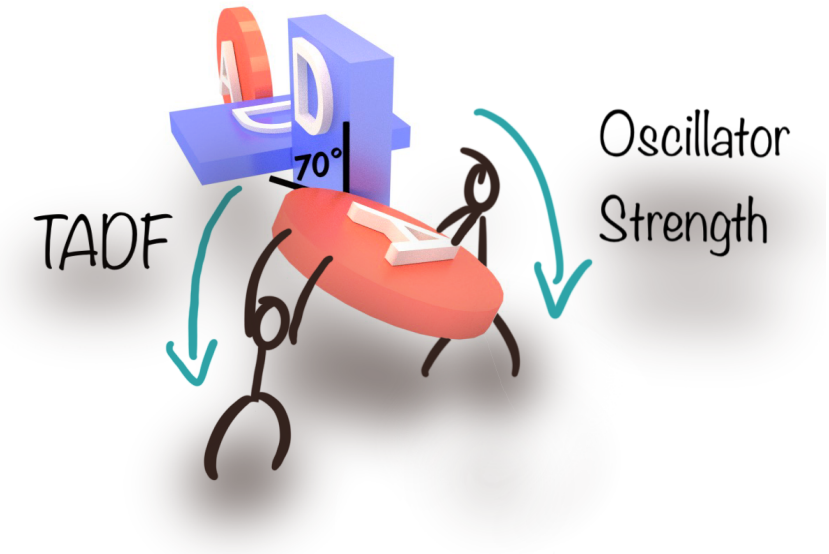

[1] This chapter is based on
Sebastian Weißenseel, Nikita A. Drigo, Liudmila G. Kudriashova, Markus Schmid, Thomas Morgenstern, Kun-Han Lin, Antonio Prlj, Clémence Corminboeuf, Andreas Sperlich, Wolfgang Brütting, Mohammad Khaja Nazeeruddin, Vladimir Dyakonov. **Getting the Right Twist: Influence of Donor–Acceptor Dihedral Angle on Exciton Kinetics and Singlet–Triplet Gap in Deep Blue Thermally Activated Delayed Fluorescence Emitter.** *The Journal Of Physical Chemistry C (2019)* doi: 10.1021/acs.jpcc.9b08269

Abstract

Here, a novel deep blue emitter SBABz4, 4,4′-(10H,10′H-9,9′-spirobi[acridine]-10,10′-diyl)-dibenzonitrile, for use in organic light emitting diodes (OLEDs) is investigated. The molecular design of the emitter enables thermally activated delayed fluorescence (TADF), which we examine by temperature dependent time-resolved Electroluminescence (trEL) and Photoluminescence (trPL). We show that the dihedral angle between donor and acceptor strongly affects the oscillator strength of the charge transfer state alongside the singlet–triplet gap. The angular dependence of the singlet–triplet gap is calculated by time-dependent density functional theory (TD-DFT). A gap of 15 meV is calculated for the relaxed ground-state configuration of SBABz4 with a dihedral angle between the donor and acceptor moieties of 86°. Surprisingly, an experimentally obtained energy gap of 72 ± 5 meV can only be explained by torsion angles in the range of $70 - 75°$. Molecular dynamics (MD) simulations showed that SBABz4 evaporated at high temperature acquires a distribution of torsion angles, which immediately leads to the experimentally obtained energy gap. Moreover, the emitter orientation anisotropy in a host matrix shows an 80% ratio of horizontally oriented dipoles, which is highly desirable for efficient light outcoupling. Understanding intramolecular donor–acceptor geometry in evaporated films is crucial for OLED applications, because it affects oscillator strength and TADF efficiency.

5.1 Introduction

Fluorescence-based organic light-emitting diodes (OLEDs) are known to reach a maximum internal quantum efficiency (IQE) η_{int} of 25% due to spin-statistics, while the incorporation of heavy metal atoms in emitting molecules enables the phosphorescence IQE of 100% due to efficient spin-orbit coupling [9–11, 13]. The molecules based on TADF can harvest nonradiative triplets via reverse intersystem crossing (RISC) and can also yield η_{int} of 100% [97–101]. Intuitively, one has to minimize the singlet-triplet energy gap to enhance the triplet-to-singlet up-conversion [23, 62]. This condition is commonly fulfilled by separating electron and hole wave functions onto different moieties, so that their overlap is reduced. Large separation of electron and hole is realized in the molecules comprised of donor and acceptor units that are almost perpendicular to each other. The dihedral angle θ between donor and acceptor determines the exchange energy and hence ΔE_{ST}. Actually, one has to find a compromise for θ, because $\theta = 90°$ means perfectly separated e-h wave functions and, consequently, zero singlet-triplet gap, but, at the same time, the oscillator strength f for radiative transi-

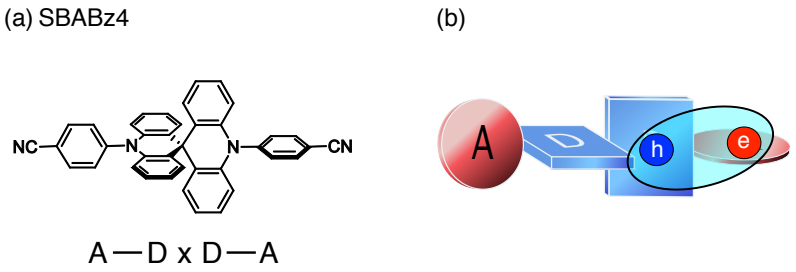

Figure 5.1: (a) Structural formula of SBABz4. The molecule consists of two acridine donors (D) linked by a spiro-bridge (x) and two benzonitrile acceptor units. (b) A sketch of the linear A–DxD–A structure. The spirobridge leads to the perpendicular arrangement of the donor groups. The orbital overlap between donor and acceptor groups is decreased due to perpendicular conformation between donor and acceptor units.

tions from the excited CT state to the ground state vanishes [69]. θ can be calculated theoretically, but the optimum value for θ is hard to predict a priori. The calculated dihedral angle θ for an isolated molecule in its relaxed configuration can differ from the real value in a thin-film device prepared by thermal evaporation. Therefore, the experimentally measured activation energies can deviate substantially from the theoretically predicted values. Thus, the relation between experimentally found activation energies and ΔE_{ST} is not evident. However, MD can reveal distribution of dihedral angles in evaporated films of TADF emitters, thereby delivering activation energies comparable to experimental values. To make use of the increased IQE, the light outcoupling should be optimized, too. The light outcoupling in OLEDs with isotropic emitters can be quantified by the outcoupling factor $\eta_{out} = 1/(2n^2)$, where n is the refractive index of the emitting layer of the device [55]. The molecular orientation in evaporated amorphous films for OLEDs is in most cases random. This leads to an isotropic light-emission that limits EQE of OLEDs. However, recent studies have shown that sticklike emitters tend to selforient themselves within the film [102–104]. The resulting anisotropic emission improves the light-outcoupling, which results in the higher theoretical limit and experimental values for EQE. Optimizing the light extraction of OLEDs is, therefore, a highly relevant aspect. In this work, we demonstrate an increased horizontal orientation of the transition dipole moment in a film of a deep blue TADF emitter. The emitter can harvest the nonradiative triplets and also yield an η_{int} close to 100 %. In addition to that, we performed optical simulations on the OLED stack with a dipole model based on the scattering matrix-transfer-formalism to calculate the maximum possible EQE in dependence of the film thicknesses in the OLED device. However, we were able to reveal the actual distribution of dihedral angles in the evaporated film of TADF emitters using MD. The resulting theoretical values for activation energies show excellent agreement with experiment. The deep blue emitting molecule studied here consists

of two donor (D) and two acceptor (A) moieties. The central core consists of two acridine donors linked by a spiro-bridge (x). Together with the two linearly attached benzonitrile acceptors, an A-DxD-A compound is realized. The molecular structure 4,4′--(10H,10′H-9,9′-spirobi[acridine]-10,10′-diyl)-dibenzonitrile (SBABz4) is shown in Figure 5.1a. The spiro bridge leads to orthogonal arrangement of acridine [105, 106]. The H atoms of the acceptor force the dihedral angle between the benzonitrile and acridine to open up [107]. This nearly perpendicular conformation between the donor and acceptor decreases the orbital overlap of the highest occupied molecular orbital (HOMO) and the lowest unoccupied molecular orbital (LUMO), which will result in the desired small singlet-triplet gap. Moreover, the spiro-connection was reported to rigidify the molecular structure and, eventually, to stabilize the planarized acridine conformation with the perpendicular arrangement of D-A pair; thus this twisted conformation favors emission via TADF channel [108]. With a full theoretical description of the transition rates of the three-level model system for the excited charge transfer states, we are able to describe the rate of the reverse intersystem crossing k_{RISC} of SBABz4 by two experimentally available observables, the TADF efficiency, ϕ_{TADF}, and the lifetime of the delayed fluorescence τ_{TADF}.

5.2 Deep Blue Emitter and Transition Dipole Moment

The theoretical calculations on the molecule were performed by our collaboration partner at École Polytechnique Fédérale de Lausanne (EPFL) by the group of Prof. Clémence Corminboeuf. The ground-state geometry of SBABz4 was calculated by utilizing density functional theory (DFT), explained in detail in the theoretical Section 5.7. In ground-state geometry, donor (acridine) and acceptor (benzonitrile) moieties are nearly orthogonal to each other (~ 86°). The Kohn-Sham HOMO and LUMO are shown in Figure 5.2. There is a clear spatial separation between HOMO and LUMO. Because the molecule is a composition of two donor and two acceptor units, there are two nearly degenerate HOMOs and LUMOs. The natural transition orbitals (NTOs) demonstrate the charge transfer character of the low-lying excited states of SBABz4 molecule. We also derived the energy of the locally excited triplet state of the donor, and it lies energetically above the degenerate excited singlet charge-transfer S1, S2 (CT) states. More theoretical details on SBABz4 are described in the appendix of this chapter in Section 5.7.

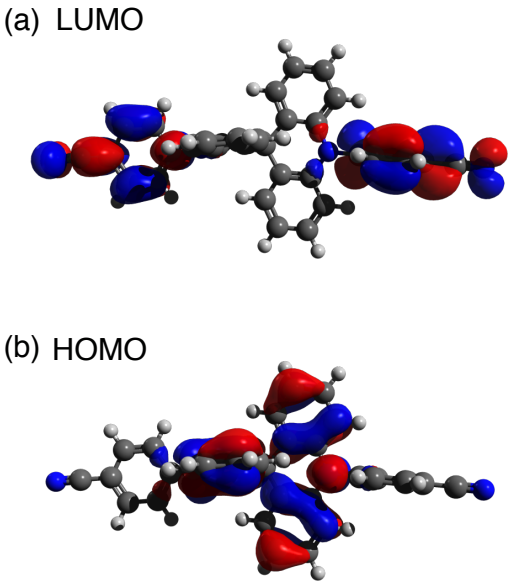

Figure 5.2: Kohn–Sham LUMO (a) and HOMO (b) of SBABz4 of the ground-state geometry of SBABz4. Density functional theory (DFT) calculations have been performed by the group of Prof. Clémence Corminboeuf from École Polytechnique Fédérale de Lausanne (EPFL). By comparing both figures, the spatial separation between HOMO and LUMO is recognizable, as well as the narrow orbital overlap at the A–D linkage.

Orientation of transition dipole moment

To determine the orientation of the transition dipole moment, angular-dependent PL spectrometry as proposed by Frischeisen et al. was performed on a 20 nm thick film of SBABz4:DPEPO (10:90) coevaporated on a glass substrate [109]. The measurements have been conducted by the group of Prof. Wolfgang Brütting at University of Augsburg. As shown in Figure 5.3a, the measurement reveals a fraction of 80% of the emitting dipoles lying within the substrate plane. This result confirms the horizontal orientation of the sticklike SBABz4 molecule as expected. The fraction of horizontal dipoles has a major impact on the device performance as explained in Section 2.2. [34].

5.3 OLED Characteristics

To study the theoretical limit for the performance of the presented devices in more detail, the Augsburg group also performed optical simulations based on the plane wave decomposition as described by Barnes et al. and Penninck et al. and as described by

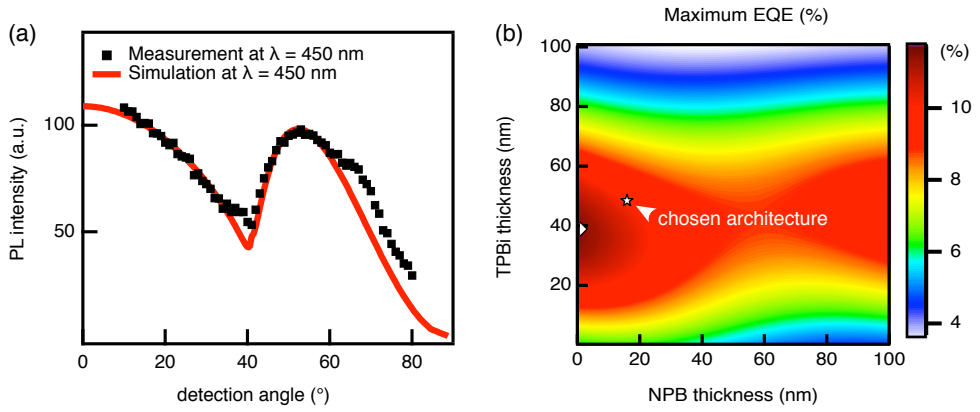

Figure 5.3: (a) Angle-resolved PL intensity of coevaporated 10 wt %SBABz4:DPEPO at a wavelength of 450 nm (squares). The fit (red trace) reveals a fraction of 80% of horizontal dipoles in the film. Note that all emission wavelengths were taken into account in the analysis, but only that for 450 nm is shown here. (b) Simulation of the maximum possible EQE (color-coded on the right) in dependence of the transport layer thicknesses. The marked values (open symbols) reveal that the realized device structure (star symbol) is very close to the theoretical optimum (diamond symbol). Angle-resolved PL and EQE calculations heve been performed by the group of Prof. Brütting at Universitiy of Augsburg

the scattering matrix formalism [110–112]. The software allows for the calculation of the maximum possible EQE in dependence of the film thickness and refractive index in the stack layout assuming balanced charge carrier injection and a singlet–triplet ratio of unity. To optimize the OLED layer stack, simulations for the EQE in dependence of the NPB (hole transport layer) thickness and the TPBi (electron transport layer) thickness between 5 and 100 nm were performed (Figure 5.3b). The transport layers were chosen as they are adjustable with the least influence on the electrical properties of the device. Note that the Purcell effect modifying the intrinsic quantum efficiency of the emitter and the predominantly horizontal emitter orientation are taken into account in the simulation. The optimum device structure in the studied ranges was identified at layer thicknesses of 41 and 5 nm of TPBi and NPB, respectively, yielding a possible EQE of 11.6%. The simulation shows no local maximum with respect to the NPB layer, because of relatively high thicknesses of ITO and PEDOT:PSS in the stack. For experimental reasons, we chose slightly different thicknesses (50 nm of TPBi and 20 nm of NPB) that predict the maximum possible efficiency of 10.0%, which is still very close to the optimum value.

We fabricated OLEDs with a 20 nm thick emitting layer of 10 wt % SBABz4 doped in a matrix of bis[2-(diphenylphosphino)phenyl] ether oxide (DPEPO). The normalized

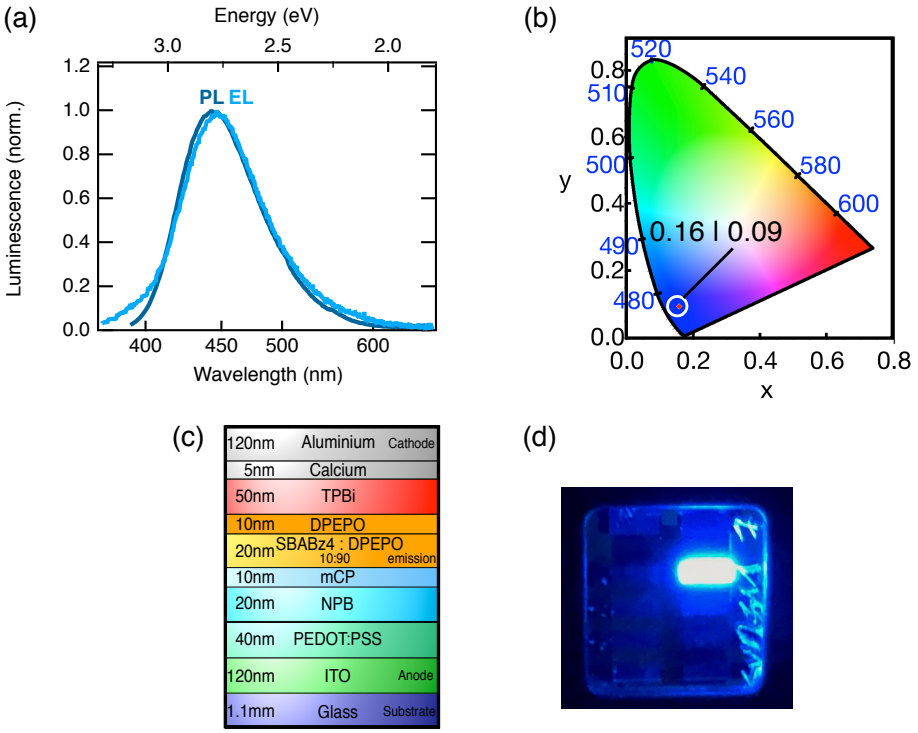

Figure 5.4: (a) Normalized PL and EL spectra of SBABz4. PL was measured on a film with 5wt% SBABz4:DPEPO, while the EL was detected from a fully processed OLED device.(b) CIE-color coordinates (0.16, 0.09). (c) Schematic device stack of 10 wt %SBABz4:DPEPO-based OLED. (d) Shows a photograph of the operating device.

photoluminescence (PL) and electroluminescence (EL) spectra are shown in Figure 5.4a and demonstrate deep blue emission, which is represented by the Commission Internationale de l'Éclairage (CIE) color coordinates (0.16, 0.09) of PL (Figure 5.4b). The optimized layer structure of the device is PEDOT:PSS (40 nm)/NPB (20 nm)/mCP (10 nm)/10 wt %SBABz4:DPEPO/DPEPO (10 nm)/TPBi (50 nm)/Ca (5 nm)/Al (120 nm) (Figure 5.4c). NPB and TPBi serve as hole and electron transport layers (PEDOT:PSS = poly(3,4-ethylenedioxythiophene)-poly(styrenesulfonate), NPB = N,N′-di(1-naphthyl)-N,N′-diphenyl-(1,1′-biphenyl)-4,4′-diamine, mCP = 1,3-bis(N-carbazolyl)benzene, and TPBi = 2,2′,2″v-(1,3,5-benzinetriyl)-tris(1-phenyl-1-H-benzimidazole)). The mCP and DPEPO neat layers are used as electron, hole, and exciton blocking layers, respectively. [24, 113, 114]. For the emission layer, a coevaporated layer of 10% SBABz4:DPEPO is included, where SBABz4 is a dopant in a DPEPO matrix. The emission of a device under electrical operation is shown in the photograph of Figure 5.4d. The emission from the SBABz4:DPEPO device is featureless and consistent with the PL spectrum of a pure SBABz4 film [115]. Emission from the DPEPO matrix is not observed, neither in PL nor in EL.

Device Optimization

A major task on the way to efficient OLED devices is reducing leakage current. In other words, charge carriers need to be confined in the emission layer instead of passing through the device without taking part in the emission. For example, by introducing an electron blocking layer between emission layer and hole transport layer (see mcP-layer in Figure 5.4c). Equivalently, to block holes, the hole blocking layer needs to be inserted between the emission layer and electron transport layer (see DPEPO-layer in Figure 5.4c). To highlight the importance of reducing leakage, we analyzed the $j-V$-characteristics of devices with and without blocking layers by Shockley evaluation (see Equation 2.9 & 2.10). The results of the analysis in Figure 5.5a are summarized in Table 5.1. For small currents, the ohmic behavior of the parallel resistance can be evaluated by a linear dependence between current and voltage. The ohmic linear regime is depicted with the grey dashed lines.

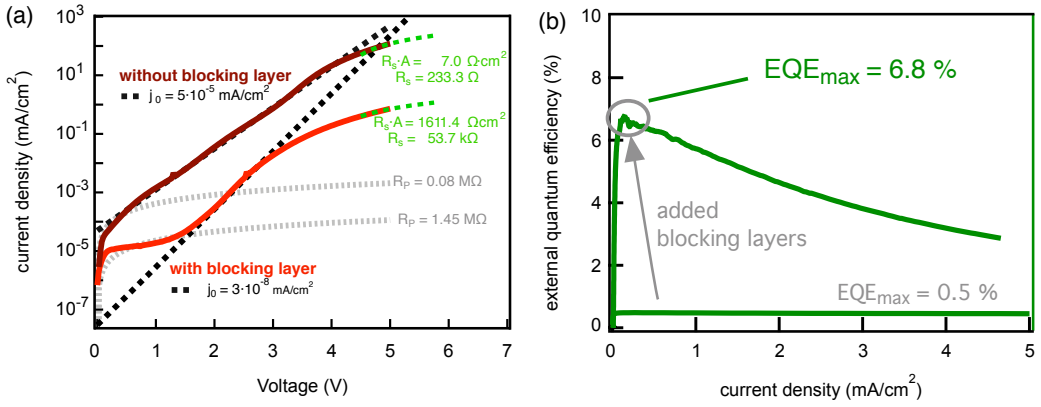

Figure 5.5: (a) $j-V$−characteristic of an SBABz4 device with and without blocking layer. Both devices are analyzed in terms of Shockley equation. The black dashed lines correspond to ideal Shockley equation (see Equation 2.9) in order to extract values for j_0. By fitting the linear $j-V$-regimes, the parallel (R_P, grey) and series resistance (R_S, green) are evaluated. (b) By introducing blocking layers, a total increase of the EQE from $\eta_{\text{ext}} = 0.5\,\%$ to $\eta_{\text{ext}} = 6.8\,\%$ can be achieved.

The blocking layers increase the parallel resistance from $R_p = 0.08\,\text{M}\Omega$ to $R_p = 1.45\,\text{M}\Omega$. Series resistance is dominating $j-V$−curves at higher voltages leading to an increase of $R_S = 7\,\Omega\text{cm}^2$ to $R_S = 1.6{\cdot}\,\text{k}\Omega\text{cm}^2$, with an active area of $A = 0.03\text{cm}^2$. The parameter j_0 is defined by the intersection of the ideal Shockley equation with the current axis. j_0 decreased by three orders of magnitude from $j_0 = 5{\cdot}10^{-5}\,\text{mAcm}^{-2}$ to $j_0 = 3{\cdot}10^{-8}\,\text{mAcm}^{-2}$. Together, all parameters point to decreased leakage currents in the device with block-

ing layers. The EQE is defined as the number of photons per injected electron. If leakage currents are reduced, a severe increase in EQE is realized from $\eta_{ext} = 0.5\,\%$ to $\eta_{ext} = 6.8\,\%$. Comparing this value with the theoretically predicted 10%, we clearly see potential for future device optimization.

	EQE /%	R_P / MΩ	R_S / Ω cm^{-2}	j_0 / mAcm^{-2}
no blocking layer	0.5	0.08	$7.0 \cdot 10^{0}$	$5 \cdot 10^{-5}$
with blocking layer	6.8	1.45	$1.6 \cdot 10^{3}$	$3 \cdot 10^{-8}$

Table 5.1: Shockley analysis of j-V-characteristics shown in Figure 5.5

5.4 Time-Resolved Electroluminescence

Figure 5.6a and b show the time-resolved measurements of SBABz4:DPEPO for PL and EL. The transient curves contain prompt and delayed components, as was shown recently [115]. We extracted the average decay time of the transients from the stretched exponential fits (dotted lines). Note that in the case of transient EL the device is turned on at −1 ms and turned off at 0 ms for trEL measurements (Figure 5.6b, inset). At these switching points, a crosstalk between current leads and detector was unavoidable. This causes oscillating spikes but does not affect the delayed emission after 10^{-5} s. With increasing temperature, the delayed component shows a faster decay for both PL (Figure 5.6a) and EL (Figure 5.6b). To evaluate the temperature activation of the reverse intersystem crossing, we can assume a three-level system consisting of an excited CT singlet (CT^1) and triplet (CT^3) state, as well as a ground state (S_0) (Figure 5.6c). The populations of the CT^1 and CT^3 states are denoted as n(t) and m(t), respectively. The transition rate constants k are marked with solid arrows, while the dashed lines indicate nonradiative loss mechanisms to the ground state (q). In this scheme, the rate constant of reverse intersystem crossing is marked as k_{RISC}. Now we can express the rate equations for n, m:

$$\frac{dn}{dt} = -(k_F + q_{10} + k_{ISC}) \cdot n + k_{RISC} \cdot m \tag{5.1a}$$

$$\frac{dm}{dt} = -k_{ISC} \cdot n + (k_{Ph} + q_{30} + k_{RISC}) \cdot m \tag{5.1b}$$

In the following, we detail the theoretical considerations necessary to solve these rate equations and express k_{RISC} in terms of measurable quantities.

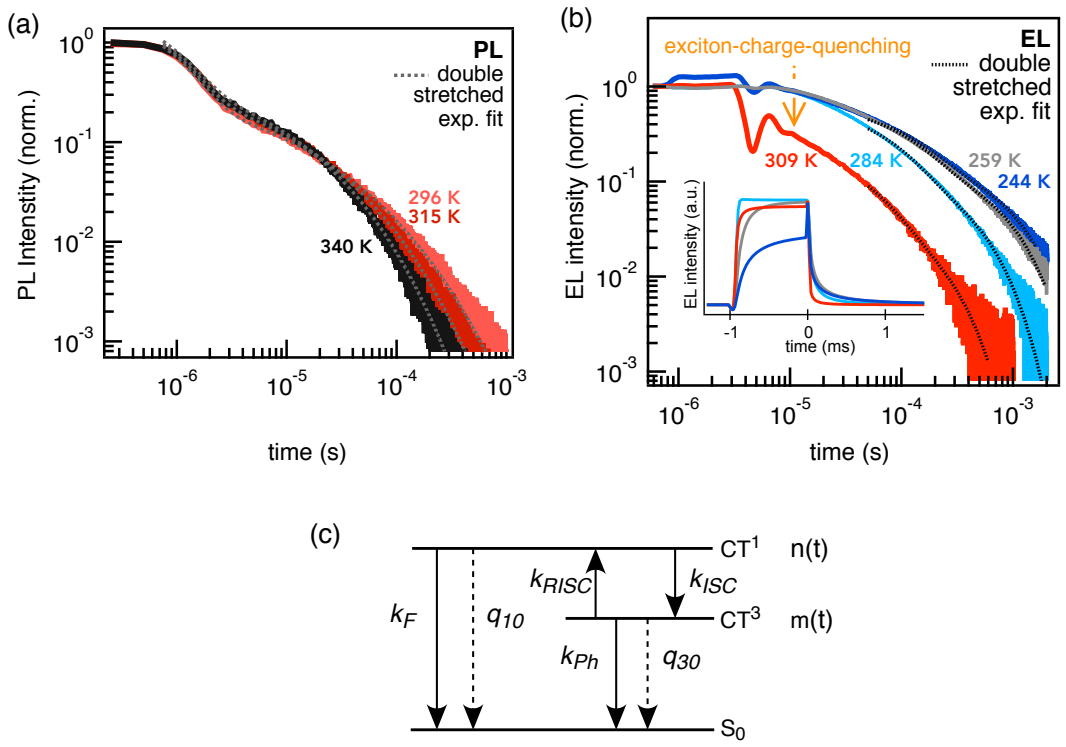

Figure 5.6: (a) Time-resolved Photoluminescence (trPL) and (b) time-resolved Electroluminescence (trEL)-transients. A double stretched exponential fit is applied to extract the temperature dependence of k_{RISC}. The inset shows the trEL transients in lin-lin-scale. (c) Rate model for a three-level system of SBABz4. The dashed lines indicate loss mechanisms to the ground state.

Excursus: Solving Rate Equations for trEL

The subsequent formalism is in accordance with [115], where the rate equation have been solved in the case of Photoluminescence. For PL, the initial values of the rate equations would be $n_0 = N_{\mathrm{PL}}$ and $m_0 = 0$, where N_{PL} is the total number of optically excited excitons. In contrast, for EL the starting parameters are given as $n_0 = 0.25\,N_{\mathrm{EL}}$ and $m_0 = 0.75\,N_{\mathrm{EL}}$, where N_{EL} is the total number of electrically generated excitons. We can set up a system of equations, where the coefficients of Equation 5.1 are written in a $2\,x\,2$ matrix A in the following:

$$A = \begin{pmatrix} a & b \\ c & d \end{pmatrix} \equiv \begin{pmatrix} k_F + q_{10} + k_{ISC} & k_{RISC} \\ k_{ISC} & k_{Ph} + q_{30} + k_{RISC} \end{pmatrix} \tag{5.2}$$

To derive the general solution of the differential Equation 5.1, one needs to find the eigenvalues λ_i of A:

$$\lambda_{1,2} = \frac{1}{2}\left(a+d \pm \sqrt{(a+d)^2 - 4(ad-bc)}\right) = \frac{1}{2}(a+d \pm \xi) \tag{5.3}$$

where

$$\xi \equiv \sqrt{(a+d)^2 - 4(ad-bc)} \tag{5.4}$$

Now, together with $\lambda_{1,2}$ and the initial conditions for Electroluminescence at $t_0 = 0$ we can give the exact solution of the rate Equations 5.1:

$$n(t) = \frac{1}{\xi}\left[(n_0(\lambda_1 - d) - bm_0)\cdot e^{-\lambda_1 t} + (n_0(d-\lambda_2) + bm_0)\cdot e^{-\lambda_2 t}\right] \tag{5.5a}$$

$$m(t) = \frac{1}{\xi}\left[(m_0(d-\lambda_2) - cn_0)\cdot e^{-\lambda_1 t} + (m_0(\lambda_1 - d) + cn_0)\cdot e^{-\lambda_2 t}\right] \tag{5.5b}$$

From measurable quantities to k_{RISC}

We need to define a quantity, which is measurable externally and coupled to the aforementioned equation system. Therefore, the rate of photon emission ν_{em} from the singlet level n can be used. It can be defined as

$$\frac{d\nu_{em}}{dt} = k_F n(t) \tag{5.6}$$

and hence

$$\nu_{em} = \int_0^\infty \frac{d\nu_{em}}{dt} dt = \int_0^\infty k_F n(t) dt \tag{5.7}$$

In a time-resolved experiment like trEL, ν_{em} is connected with the initial populations n_0 and m_0 in the EQE of EL, which is defined as the ratio between the number of photons emitted by the device and the total number of charge carriers (see Section 2.2):

$$\eta_{eqe} = \frac{\nu_{em}}{n_0 + m_0} \tag{5.8}$$

If Equation 5.7 and 5.5 are combined and inserted in η_{eqe}, we obtain

$$\eta_{eqe} = \frac{k_F}{n_0+m_0}\frac{1}{\xi}\left(\frac{n_0(\lambda_1 - d) - bm_0}{\lambda_1} + \frac{n_0(d-\lambda_2) + bm_0}{\lambda_2}\right) \tag{5.9}$$

and hence:

$$\eta_{eqe} = \frac{k_F}{n_0+m_0}\frac{1}{\xi}(n_0 d + m_0 b)\left(\frac{1}{\lambda_2} - \frac{1}{\lambda_1}\right) \tag{5.10}$$

Which can be splitted into prompt component

$$\eta_{eqe,pr} = \frac{k_F}{n_0 + m_0} \frac{1}{\xi} \frac{n_0(\lambda_1 - d) - bm_0}{\lambda_1} \tag{5.11}$$

and delayed component

$$\eta_{eqe,TADF} = \frac{k_F}{n_0 + m_0} \frac{1}{\xi} \frac{n_0(d - \lambda_2) + bm_0}{\lambda_2} \tag{5.12}$$

The ratio between prompt and delayed components results in

$$\frac{\eta_{eqe,pr}}{\eta_{eqe,TADF}} = \frac{n_0(\lambda_1 - d) - m_0 b}{\lambda_1} \cdot \frac{\lambda_2}{n_0(d - \lambda_2) + bm_0} \tag{5.13}$$

For Electroluminescence, the inital parameters are $n_0 = 0.25 \cdot N_{\mathrm{EL}}$ and $m_0 = 0.75 \cdot N_{\mathrm{EL}}$, with N_{EL} being the total number of electrically generated excitons on the SBABz4 molecule:

$$\frac{\eta_{eqe,pr}}{\eta_{eqe,TADF}} = \frac{\lambda_2}{\lambda_1} \frac{0.25(\lambda_1 - d) - 0.75b}{0.25(d - \lambda_2) + 0.75b} \tag{5.14}$$

Now we can apply several approximations based on Photoluminescence quantum yield (PLQY) measurements shown in [115] in order to reduce the complexity of Equation 5.14 and deduce a formalism to evaluate k_{RISC}:

- $q_{10} = 0$ — only radiative decay from singlet, since the prompt PL component is temperature-independent
- $k_{\mathrm{ph}} = 0$ — phosphorescence is not observed at room temperature
- $k_{\mathrm{F}} \approx k_{\mathrm{ISC}}$ — rate of radiative decay from the singlet is close to ISC rate, since the triplet is effectively populated
- $k_{\mathrm{RISC}} \approx q_{30}$ — rate of RISC is in the order of triplet non-radiative rate, since both processes are observed
- $k_{\mathrm{F}} \gg k_{\mathrm{RISC}}$ — rate of singlet radiative decay significantly exceeds RISC, since the observed prompt decay is way faster than TADF

which directly leads to the following relationships in Equation 5.14:

$$\lambda_1 - d \approx \lambda_1 \approx a \quad \text{and} \quad d - \lambda_2 \approx \frac{bc}{a} \tag{5.15}$$

and

$$\frac{\eta_{eqe,pr}}{\eta_{eqe,TADF}} \approx \frac{\lambda_2}{k_{\mathrm{RISC}}} \frac{1}{3 + \frac{k_{\mathrm{ISC}}}{\mathrm{F} + k_{\mathrm{ISC}}}} \tag{5.16}$$

Finally, by assuming $k_{\mathrm{RISC}} \sim \exp(-\Delta E_{\mathrm{kT}}/k_b T)$, we can express RISC rate by the TADF efficiency $\eta_{\mathrm{eqe,TADF}}$ and the decay time of the delayed emission $\tau_{\mathrm{TADF}} = 1/\lambda_2$ through

$$\ln(k_{\mathrm{RISC}}) = \ln\left(\frac{\eta_{\mathrm{eqe,TADF}}}{\tau_{\mathrm{TADF}}}\right) + C_1 = \frac{-E_A}{k_b T} + C_2 \tag{5.17}$$

where C_1 and C_2 are temperature-independent constants.

Combing Theory and Experiment of trEL

$\eta_{\mathrm{eqe,TADF}}$ is evaluated by integrating the delayed part of the transient over time. The resulting area is proportional to the number of detected photons. The decay time τ_{TADF} can be extracted from the double stretched exponential fit with $\alpha = 0.5$ [31]

$$I(t) = A \cdot \exp\left(-\left[\frac{t}{\tau_{\mathrm{pr}}}\right]^{\alpha}\right) + B \cdot \exp\left(-\left[\frac{t}{\tau_{\mathrm{TADF}}}\right]^{\alpha}\right) \tag{5.18}$$

With Equation 5.17, we are able to determine the activation energy E_A from trPL and trEL. Note that Equation 5.17 takes into account only phonon-assisted nonradiative decay of triplets (denoted with q_{30}), which is valid for the contactless trPL measurement. However, additional nonradiative processes, such as exciton-charge quenching, can take place in complete devices. The trEL data show a clear hint for nonradiative exciton-charge recombination. The rapid decrease of intensity at 309 K (orange arrow above the red curve in Figure 5.6b) is at 10^{-5} s. There, the intensity of the transient is lower as compared to other temperatures. At higher temperatures, more charges are available because of a higher current density. Note that the measurements are taken at constant voltage, while the current density is increasing with temperature. Altogether, because of exciton-charge-quenching, Equation 5.17 underestimates k_{RISC} values found from trEL at high concentration of free charges, that is, at high temperatures.

5.5 Arrhenius Evaluation

The Arrhenius plot for RISC derived from temperature dependent trPL and trEL is shown in Figure 5.7. A linear behavior is observed for trPL from 295 to 340 K. The activation energy according to Equation 5.17 is (72 ± 5) meV. This temperature activation is also valid for the EL of the device. The term $\ln(k_{\mathrm{RISC}})$ is increasing with temperature from 244 to 264 K. With higher temperature, the device is suffering from loss mechanisms mentioned above, which are also temperature activated. Because of the enhanced losses at elevated temperatures (> 264 K), the trEL shows a decrease for $\ln(k_{\mathrm{RISC}})$.

These losses are absent in trPL, which leads to the assumption that the emission layer itself is not affected by these losses. In contrast to the experimentally determined activation energy, TD-DFT computations for the ground-state conformation of SBABz4 ($\phi = 86°$) predict a value of $\Delta E_{ST} = 15\,\text{meV}$. If the dihedral angle is deviating from this conformation, the orbital overlap between HOMO and LUMO is increasing. Because the exchange integral J_{ex} is linked to the singlet-triplet gap $\Delta E_{ST} = E_S - E_T = 2J_{ex}$ (see Equation 3.11), the gap between the singlet E_S and triplet E_T energy increases as well [25, 64]. Figure 5.8a shows the calculated singlet-triplet gap ΔE_{ST} in dependence of the

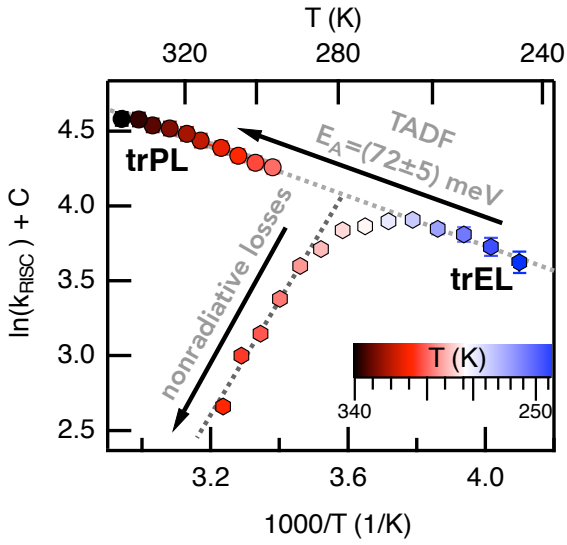

Figure 5.7: Arrhenius plot of k_{RISC} for trPL and trEL data. An activation energy for RISC $\Delta E_A = (72 \pm 5)\,\text{meV}$ can be evaluated.

dihedral angle (red curve). The experimental value is marked in orange. This indicates that the conformation of SBABz4 in an evaporated layer is different from the relaxed molecule in vacuum. Hot evaporation (T= 468 K) of SBABz4 with DPEPO matrix supplies the necessary energy to twist the acceptor in the film (Figure 5.9a). To gain more insight into the influence of the evaporation on the dihedral angle, the collaboration partners of EPFL performed MD simulations [116, 117]. In the calculations, a film of SBABz4:DPEPO with the ratio of 1:9 is generated, with 1000 molecules in total. The system is then equilibrated at 300 K (Figure 5.8b). After equilibrium is reached, 1000 snapshots of the film are averaged to obtain a statistical distribution of the torsion angles between D and A in all SBABz4 molecules. For each molecule in the deposited film, TD-DFT computations are performed to extract a distribution of values for ΔE_{ST}. To include the dielectric effect, we adopt an implicit solvent model in TDDFT com-

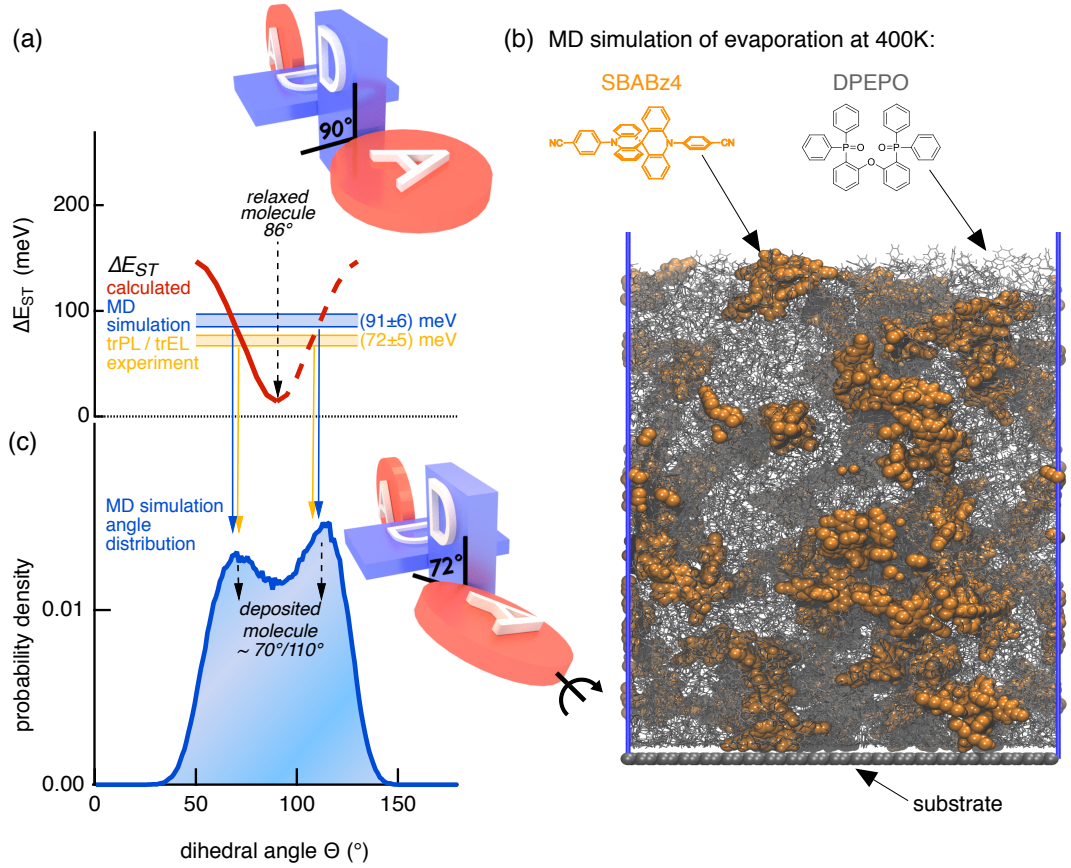

Figure 5.8: (a) Computed singlet-triplet gap ΔE_{ST} (red trace) for SBABz4 in dependence of the dihedral angle θ between A and D (with the other A-D dihedral angle kept fixed at 90°). TD-DFT calculations for a relaxed molecule predict a dihedral angle $\theta = 86°$. Experimental value for ΔE_{ST} (orange); average ΔE_{ST} obtained from MD simulations (blue). (b) MD simulation mimicking the evaporation process for a film of 10 mol % of SBABz4 (orange space-filling models) in DPEPO (gray sticklike models). For each molecule in the deposited film, TD-DFT calculations are performed to extract a mean ΔE_{ST} and the distribution of θ. (c) Probability density of θ averaging 1000 MD simulation snapshots (performed by the group of EPFL).

putations with the dielectric constant $\epsilon_0 = 3$. The mean ΔE_{ST} value, which takes into account all simulated SBABz4 molecules, is 91 ± 6 meV (blue region in Figure 5.8a). The probability density of the dihedral angle in Figure 5.8c also indicates two local maxima at $\theta_1 \approx 70°$ and $\Theta_2 \approx 110°$. These maxima of the angle distribution coincide with the experimental value obtained from trPL and trEL (marked with orange arrows) and with the theoretical value obtained from MD simulations (marked with blue arrows). Combining the experimental value with MD simulation, we conclude that the dihedral angle of the molecule in an evaporated film is different from the relaxed value of

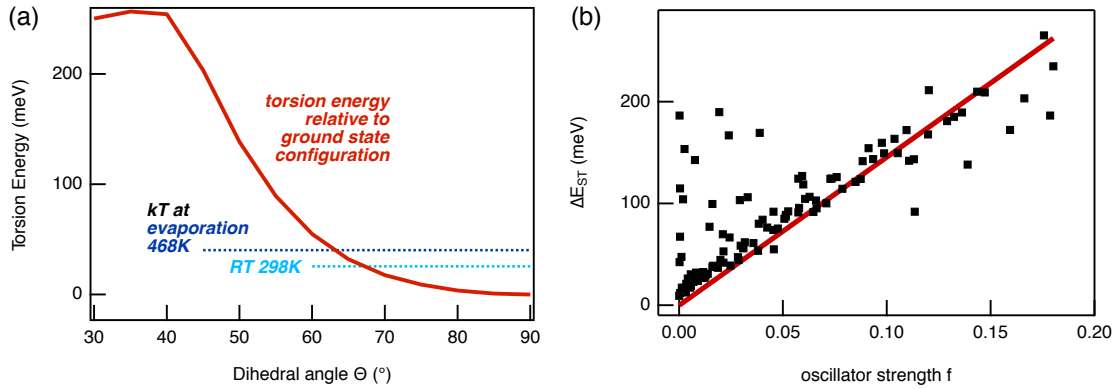

Figure 5.9: (a) Relative energy of SBABz4 with different dihedral angles (benzene-acridine) in constrained-relaxation dihedral scan (b) The oscillator strength f and singlet-triplet gap ΔE_{ST} for each molecule from MD simulation (black dots). f is larger for molecules with twisted donor-acceptor conformation and hence larger singlet-triplet gap. The red line is a guide to the eye. (Calculations have been performed by the group of EPFL)

$\Theta = 86°$. The actually dominant dihedral angles in the evaporated film have an impact on the oscillator strength f. Figure 5.9b shows f and singlet-triplet gap ΔE_{ST} for each molecule obtained from MD simulation. SBABz4 in the relaxed conformation shows only weak emission properties. The favored conformation in the film is substantial to reach efficient emission, while the increased singlet-triplet gap also constricts the efficiency of the RISC process of SBABz4. The observation that the trEL and trPL traces in Figure 5.6a,b can only be fitted by stretched exponential functions and not by ordinary exponentials is a direct result of the distribution of dihedral angles and thus singlet-triplet gaps and oscillator strengths. We expect that earlier (later) emitting molecules have larger (smaller) ΔE_{ST} and larger (smaller) f.

5.6 Conclusion

In this work, we presented a novel sticklike molecule SBABz4 with A-DxD-A structure for deep blue emitting OLED applications. It enables TADF under optical and electrical excitation. In a coevaporated SBABz4:DPEPO film, the horizontal orientation of the emission transition dipole moment was found to be 80 %, which is essential for enhanced light outcoupling. A detailed analysis of the underlying rate equations for temperature-dependent transient PL and EL revealed an activation energy of $\Delta E_{ST} = 72 \pm 5$ meV. The OLED device layer stack was optimized for maximum EQE by optical modeling of the transport layer thicknesses, which was reproduced experi-

mentally. By implementing advanced molecular dynamics and TD-DFT simulations, we recreated the OLED coevaporation process and explained the experimental results by the actual molecular conformation in the coevaporated thin film. We can thus link the activation energy to a mean dihedral angle of $\theta \approx 70-75°$ between the donor and acceptor units, which deviates decisively from $\theta = 86°$ for a relaxed molecule in vacuum. The later would offer a lower ΔE_{ST}, but would also result in a vanishing oscillator strength f for radiative transitions. Thus, the optimal emitter design and deposition for the next-generation OLEDs requires finding a balance between the low activation energy for efficient TADF and sufficient oscillator strength for high total emission.

5.7 Additional Theoretical Details

The ground state geometry of SBABz4 is optimized utilizing density functional theory (DFT) with B3LYP density functional, D3BJ dispersion correction and 6-31G(d,p) basis set [118–120]. For the description of excited states, we employ linear-response time-dependent density functional theory with Tamm-Dancoff approximation (TDA/TD-DFT) along with the state-of-the-art γ-tuned LCBLYP functional with 6-31G(d,p) basis set to compute the excitation energies and oscillator strengths [121]. The range separation parameter γ was tuned to minimize the difference between minus highest occupied molecular orbital (HOMO) energy and vertical ionization potential. The value of γ is 0.165 Bohr^{-1} for SBABz4. All computations are done in gas phase.

5.8 Additional Experimental Details

PL Measurements. The PL samples were evaporated on glass substrates with a weight ratio of 10:90 (SBABz4:DPEPO,20 nm). Time-resolved and steady-state PL were detected with a calibrated fluorescence spectrometer (Edinburgh Instruments FLS980). Three excitation sources were used: continuous broad-spectrum xenon lamp Xe1, microsecond xenon flash lamp μF920, and an 80 ps pulsed UV diode laser EPL with 375 nm. Temperature was controlled in a cryostat (Janis ST-100) under active vacuum with $p < 10^{-5}$ mbar.

Contributions to this Chapter

Sebastian Weißenseel[1] (S.W.), Andreas Sperlich[1] and Vladimir Dyakonov[1] designed the experiments. S.W. prepared the devices and films, measured (time-resolved) electroluminescence and device characteristics and evaluated the data.

Liudmila Kudriashova[1] measured (time-resolved) Photoluminescence.
Nikita A. Drigo[2], Mohammad Khaja Nazeeruddin[2] designed and synthesized the molecule.
Markus Schmid[3], Thomas Morgenstern[3] and Wolfgang Brütting[3] measured angular-dependent Photoluminescence and contributed theoretical EQE predictions.
Kun-Han Lin[4] , Antonio Prlj[4,5] , Clémence Corminboeuf [4] performed TD-DFT and MD calculations.

[1]Experimental Physics VI, Julius-Maximilian University of Würzburg, 97074 Würzburg, Germany
[2]Group for Molecular Engineering of Functional Materials, École Polytechnique Fédérale de Lausanne (EPFL), Sion CH-1951, Switzerland
[3]Experimental Physics IV, University of Augsburg, Augsburg 86159, Germany
[4]Laboratory for Computational Molecular Design, and [5]Laboratory of Theoretical Physical Chemistry, EPFL, Lausanne CH-1015, Switzerland

6 Magnetic Field Dependence of Spin Resonance Linewidth in TADF based OLEDs[1]

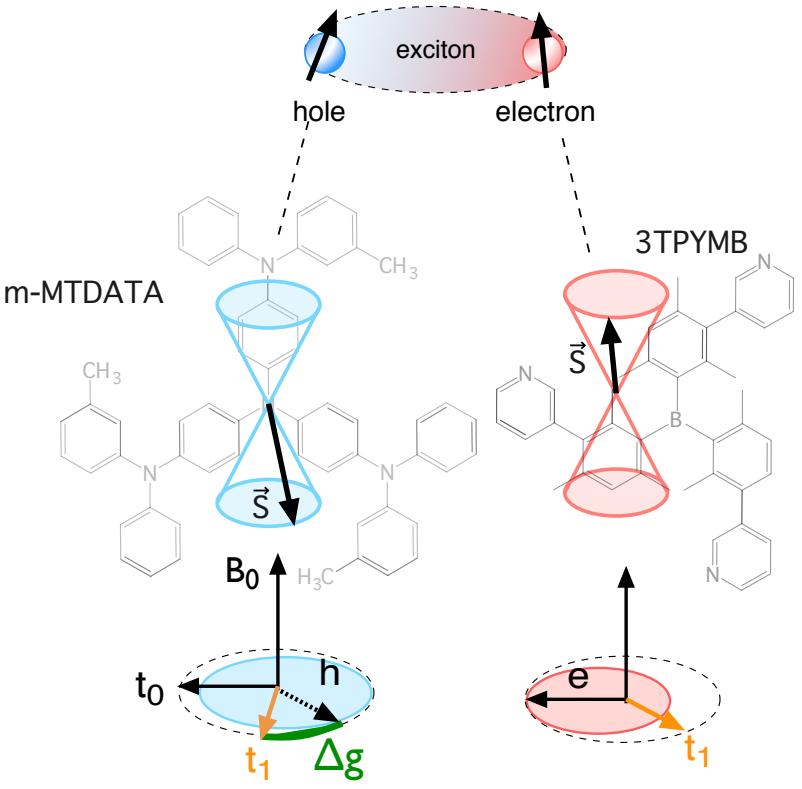

The Δg-mechanism (green) in TADF compounds. Adaped from [63].

[1] This chapter is based on
Sebastian Weißenseel, Rebecca Bönnighausen, Nikolai Bunzmann, Andreas Sperlich, Vladimir Dyakonov. *In preparation*

Abstract

Here, we present a spin sensitive study of organic light emitting diodes (OLEDs) based on thermally activated delayed fluorescence (TADF). We analyze the singlet-to-triplet up-conversion via reverse intersystem crossing (RISC) with multi-frequency electroluminescence detected magnetic resonance (ELDMR). The idea behind these experiments is that the static magnetic field applied to devices under test modifies only the energy levels of triplet states due to Zeeman splitting, thus changing the emission rates. We observed that resonant microwave radiation, applied to TADF based OLEDs by a stripline, led to a change in Electroluminescence. In detail, we shine light on the difference between inter- and intra-molecular TADF systems by applying a broad range of resonance frequencies. With this method, we gain knowledge about the magnetic field dependence of the linewidth of the ELDMR signal. Surprisingly, by evaluating the resonance linewidth for various TADF compounds, we obtain different results with respect to a driving force of RISC, the so-called $\Delta g-$mechanism.

6.1 Introduction

A physical quantity, which describes the interaction of a spin system with its environment is the electronic g-tensor [73, 75]. If the spin environment is complex and especially different in spatial directions, the diagonal components of the tensor g_{xx}, g_{zz} and g_{yy} have not the same value. This particular phenomenon is then called g-anisotropy. Furthermore, if a spin system is considered, in which the total spin S is composed of two individual spins $S = s_1 + s_2$, the g-factor of both individual spins s_i can be different. This important effect is based on two interacting spins with two *distinct* g-factors. The difference is defined as $\Delta g = g_2 - g_1$ and named the Δg-mechanism. If the precession of one of the charge carriers is faster, it is possible that a change of the multiplicity of the total spin takes places due to rephrasing of the spin vector along the magnetic field axis [63]. In short, the predominantly spin-forbidden conversion from triplet state (total Spin $S = 1$) to singlet singlet (total Spin $S = 0$) and vice versa is more favorable. The deviation of the g-factor from the value of a free electron g_e can be caused by effects of spin-orbit coupling (SOC) [73, 75], an effect which is highly discussed in the community of modern organic light emitting diodes (OLEDs) for being the adjusting screw in efficiency limitations. In these OLED devices, which are based on thermally activated delayed fluorescence (TADF), such an efficiency limiting process is the thermal up-conversion of triplets to singlets, the reverse intersystem crossing (RISC) [23, 62]. The singlet yield due to up-conversion is limited by the RISC rate

k_{RISC}. Now, SOC can heavily affect k_{RISC} of TADF OLEDs via the Δg-mechanism [63]. However, to generate a non-vanishing influence on the (R)ISC-rate k_{RISC}, the radiationless spin-flip transition from singlet to triplet state should involve a change of orbital-character. This well-known phenomenon can be found in literature, described as the El-Sayed rule [122, 123]. In detail, a transition from a $^1(n\pi^*)$-state to $^3(\pi\pi^*)$-state is said to be very fast, while the transitions between the same orbital type are relatively slow, e.g a transition from $^1(\pi\pi^*)$ to $^3(\pi\pi^*)$. Here n stands for a n-type orbital and π for a π-orbital (see Section 2.1). In the second case, the spin-orbit matrix element $\langle^1\mathrm{CT}|\,H_{SO}\,|^3\mathrm{CT}\rangle \approx 0$ [122, 123]. In some TADF compounds a spin-vibronic coupling leads to non-vanishing SOC matrix element, when a vibrationally assisted intersystem crossing is introduced [124, 125]. However, in this work, the inter-molecular (D:A) TADF systems m-MTDATA:BPhen and m-MTDATA:3TPYMB are investigated (Figure 6.1a, b), which are well studied in literature [62, 63, 72, 126]. The emission of these systems originates from a so-called exciplex, where the hole and the electron are located separately on two different molecules. The examination of exciplex-based systems offers the advantage of replacing one unit, e.g. the acceptor, without changing the other, e.g. the donor. In addition, an intra-molecular TADF emitter, DMAC-DPS, is studied [24, 97, 100, 101, 114, 127].

Here, the triplet to singlet up-conversion of the TADF emitters is analyzed by an advanced magnetic resonance technique over a broad range of magnet field. The results give an insight into the importance of electronic g-factor of the emitting species and provide experimental proof of SOC-contributions to the RISC process. We analyze the magnetic field dependent linewidth of multi-frequency ELDMR to deduce a value for Δg, the g-factor difference responsible for the Δg-mechanism.

6.2 Materials and Devices

In this work we investigate OLEDs based on two different approaches: inter-molecular and intra-molecular TADF systems. The molecular structure of the inter-molecular TADF compounds are shown in Figure 6.1a and b. The exciplex (D:A) TADF systems use the same molecule as an acceptor. From this fact it is obvious how simple it is to change the acceptor without having to change the whole device structure. The device structure is depicted in Figure 6.1c. For both material system we applied layer thicknesses of PEDOT:PSS (40 nm) / Donor (30 nm) / Donor:Acceptor (1:1) (70 nm) / Acceptor (30 nm) / Ca (5 nm) / Al (120 nm). The molecule based on the intra-molecular approach DMAC:DPS is shown in Figure Figure 6.1d. It is based on three units, namely, two donor

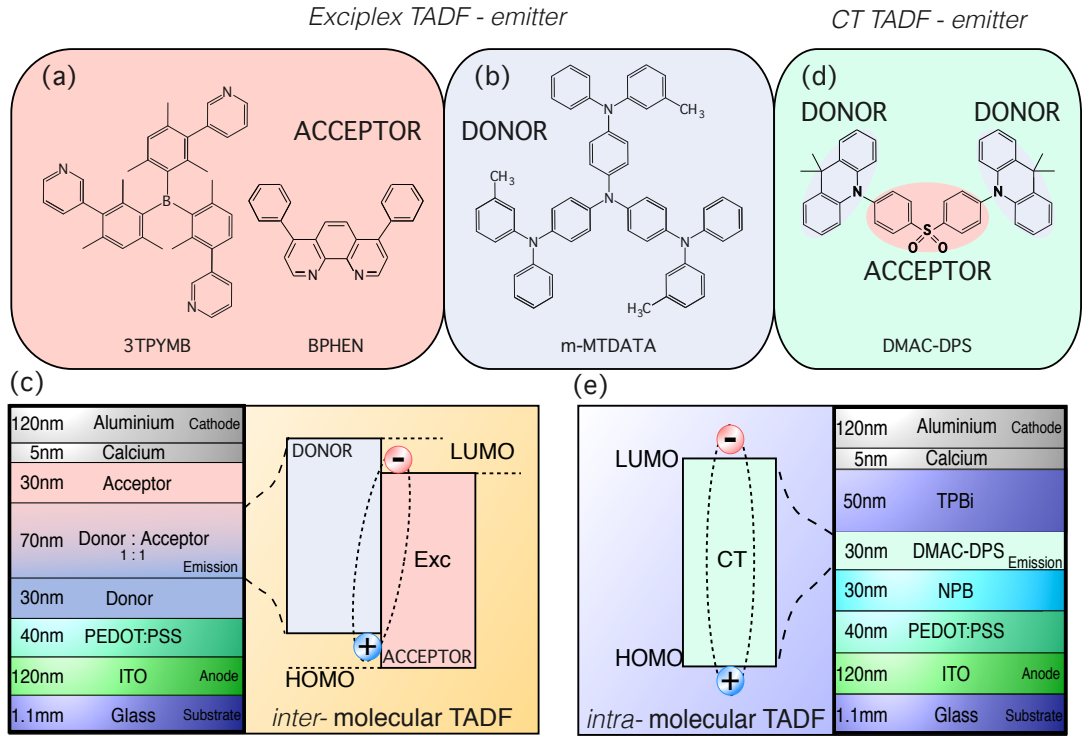

Figure 6.1: Molecular structures of the investigated TADF materials. (a) Two acceptor molecules: 3TPYMB and BPhen (b) Donor molecule m-MTDATA (c) Exemplary device structure for inter-molecular TADF OLEDs with mixed Donor:Acceptor layer with a ratio of 1:1. (d) TADF emitter with (D-A-D) structure, DMAC-DPS. (e) Device structure of the intra-molecular-based OLED. Here, the exciton is extended upon donor and acceptor units of the emitter molecule, resulting in a charge transfer state (CT).

(D) units consisting of 9,9-dimethyl-9,10-dihydroacridine and one acceptor (A) unit as diphenylsulphone.

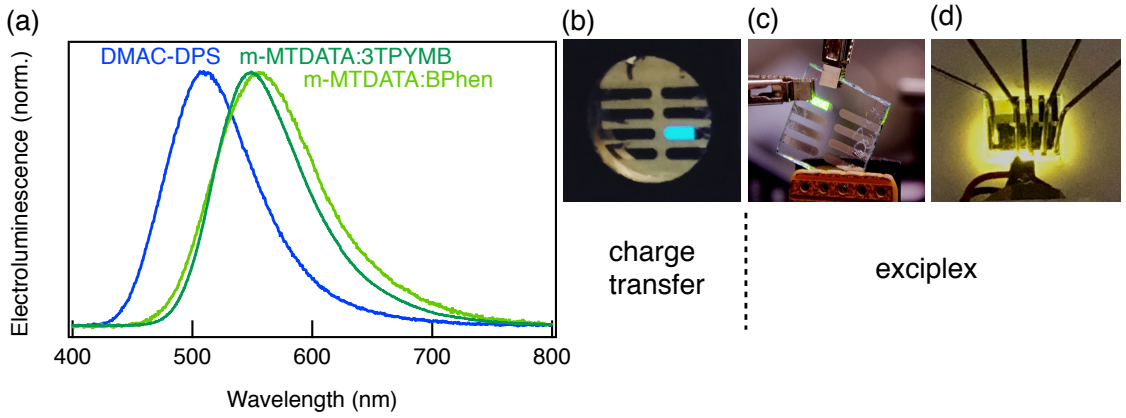

Figure 6.2: (a) Normalized Electroluminescence (EL) of the three TADF based devices (b) DMAC-DPS is a sky-blue charge transfer emitter. (c) m-MTDATA:3TPYMB and (d) m-MTDATA:BPhen are based on the exciplex approach and emit in the green spectral region.

The three units are linked as a D-A-D-structure with perpendicular dihedral angles between them [24]. This special design leads to a vanishing overlap between the highest occupied molecular orbital (HOMO) and the lowest unoccupied molecular orbital (LUMO), which is desired for small singlet-triplet gaps ΔE_{ST} to enhance the RISC process. The emissive excited state of such a D-A-D is called a charge transfer state (CT) and is spread solely on a single molecule. The device structure is PEDOT:PSS (40 nm) / NPB (30 nm) / DMAC:DPS (30 nm) / TPBi (50 nm) / Ca (5 nm) / Al (120 nm) as shown in Figure 6.1e. In contrast, the D:A systems extend over two molecules and the emissive state is called an exciplex state. If an external voltage is applied, charge carriers are injected into the cathode (electrons) and anode (holes). After passing the transport layers by hopping transport, the carriers form excitons with a triplet-to-singlet ratio of 3:1 in the emission layer. Due to the thermally activated triplet-to-singlet up-conversion, the emission of TADF systems is broadened compared to pure fluorescence emitter based devices. The EL of all three devices is shown in Figure 6.2a. The emission of both exciplexes is in the green spectral region. In contrast, the emission of the CT-emitter DMAC:DPS is sky-blue. Fotographs of the emitting devices are depicted in Figure 6.2b-d.

6.3 Magnetic Field Dependance of Spin Resonance Linewidth

One way to identify influences of the g-factor on TADF based triplet-to-singlet up-conversion, is to apply spin-sensitive methods, in our case an advanced version of electron spin resonance, ELDMR [128–131]. This technique provides access to measure spin-transitions in a fully processed device and detect them optically via a photodetector. A detailed description of the ELDMR can be found in Section 4.4.1. A huge advantage of this technique is, that the detection is solely sensitive to states, which are involved in the emissive pathway. Hence, the triplet populations, which are sensitive to a magnetic field due to Zeeman interaction, are manipulated by resonant microwave radiation. The resonance condition between the microwave and the Zeeman splitting is written as [73]:

$$h\nu_{\mathrm{mw}} = g\mu_B B_0 \Delta m_s \tag{6.1}$$

where h is Planck's constant, ν_{mw} is the microwave frequency, g is the g-factor of the exciplex spin, μ_B is the Bohr magneton, B_0 the external magnetic field and Δm_s is the change of the magnetic spin quantum number m_s. ELDMR detects only the specific triplet states, which did undergo RISC to the emissive singlet state. The measurement

of ELDMR on TADF systems has been reported previously [129–131]. Now, we developed a setup to measure OLED devices on a broad range of resonance positions from $B_0 \sim 30\,\mathrm{mT}$ to $\sim 1.4\,\mathrm{T}$, which corresponds to a microwave frequency range of $\nu_{\mathrm{mw}} = 1\,\mathrm{GHz}$ to $39\,\mathrm{GHz}$. If two different g-factors of charge carriers, which form the exciplex, are considered, for example g_1 for electron and g_2 for hole, then the difference in resonance position ΔB of the charge carriers is linearly increasing when the resonance position is changed to higher microwave frequencies ν_{mw}. From equation 6.1, we can calculate the difference of two g-factors $\Delta g = g_2 - g_1$ and how it is connected to the difference of the magnetic field resonance positions ΔB [132]:

$$\Delta B = \left(\frac{\Delta g}{g_1 \cdot g_2}\right) \frac{h\nu_{\mathrm{mw}}}{\mu_B} \tag{6.2}$$

If an ELDMR experiment is measured at low frequencies ν_{mw}, the influence of Δg is negligible. The linewidth of the resonance is then primarily broadened by hyperfine and dipolar interactions [133]. With increasing resonance position to higher frequency bands, the magnetic field dependence of the linewidth is dominated by the Δg- mechanism. In this work, we detect the electroluminescence of TADF devices and apply multi-frequency ELDMR. From the magnetic field dependence of the ELDMR broadening, we are able to extract a value of Δg for the three different material systems introduced above. A representative measurement with the donor:acceptor device based on m-MTDATA:BPhen is shown in Figure 6.3a. The resonance frequency of this measurement is $\nu_{\mathrm{mw}} = 1\,\mathrm{GHz}$. A Gaussian fit is applied to the experimental data to evaluate the full width at half maximum (FWHM) of the spectrum. The FWHM at 1 GHz of m-MTDATA:BPhen is found to be FWHM= 2.3 mT. As an exemplary overview, all multifrequency-ELDMR curves from m-MTDATA:BPhen are shown together on one magnetic field axis up to $B_0 = 1.4\,T$ in Figure 6.3b. Since the microwave transmission properties of the microwave stripline is slightly frequency dependent due to standing waves in the microwave transmission line, the intensity of each spectrum can not be evaluated. All further ELDMR spectra are normalized to compare the linewidth at different resonance frequencies. To compare the magnetic field spectra taken at low field ($\nu_{\mathrm{mw}} = 1\,\mathrm{GHz}$) and high field ($\nu_{\mathrm{mw}} = 38\,\mathrm{GHz}$), we subtracted the resonant magnetic field position B_0 and generated a new axis $B - B_0$. This plot is shown in Figure 6.4a. The red and the yellow curve compare the two measurements from m-MTDATA:BPhen. As can easily be seen, the two curves have both the same shape and the same linewidth. In this case, there is no broadening of the linewidth observable for this exciplex system, since both Gaussian fits show a linewidth of FWHM= 2.3 mT. Now, if only the acceptor is changed from BPhen to 3TPYMB, the situation is completely different. At first we

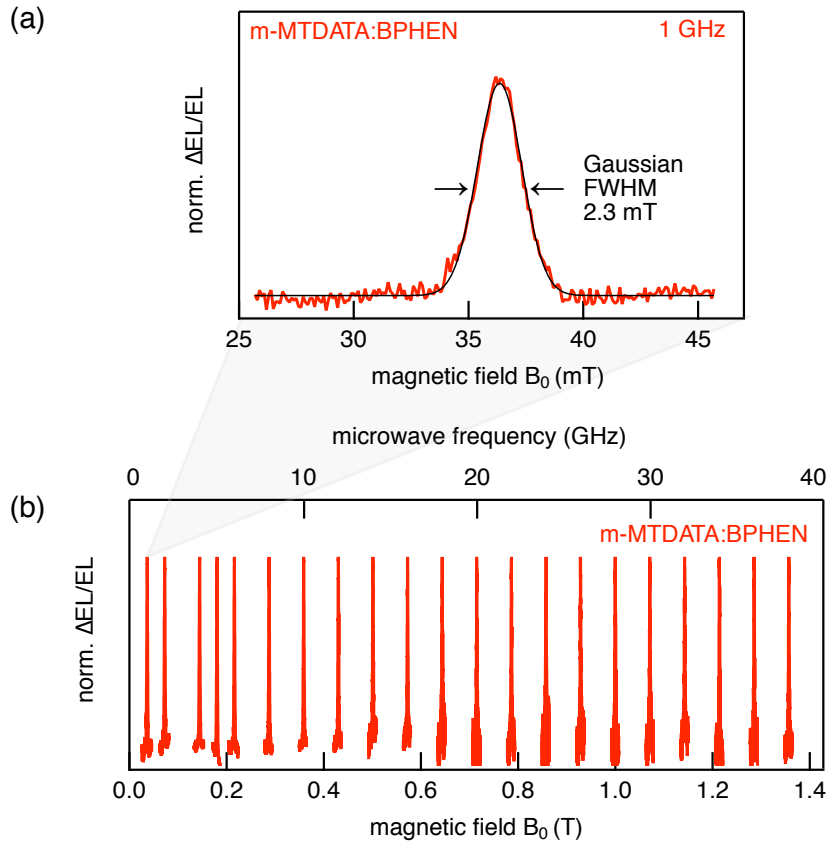

Figure 6.3: (a) Exemplary ELDMR spectrum (red curve) of the intermolecular TADF system m-MTDATA:BPhen at ν_{mw} = 1 GHz. The spectrum is evaluated by a Gaussian fit (black curve), to extract the full width at half maximum FWHM= 2.3 mT. (b) The multi-frequency ELDMR measurements of m-MTDATA:BPhen at various resonant frequencies from ν_{mw} = 1 GHz to 38 GHz.

have to note that the linewidth at $\nu_{mw} = 1\,GHz$ has increased from FWHM= 2.3 mT in m-MTDATA:BPhen to FWHM= 3.7 mT in m-MTDATA:3TPYMB. Secondly, if the resonance position is increased to $\nu_{mw} = 38\,GHz$, the total linewidth of this exciplex system clearly shows a significant linewidth broadening with increasing magnetic field B_0 from FWHM= 3.7 mT to FWHM= 4.4 mT. Remarkably, in both cases an exciplex is the emitting species, but it looks like the spin resonance behavior in ELDMR measurement is not equal. This contradiction will be discussed later. As a third test device, the intramolecular TADF emitter DMAC-DPS was examined. The ELDMR results differ from the two exciplex devices. The resonance curve here is represented by a Lorentzian instead of a Gaussian shape (light blue curve in Figure 6.4a). With a value of FWHM= 1.3 mT, the linewidth is smaller compared to both exciplex systems. The increase of the linewidth as shown for m-MTDATA:3TPYMB is also observable for DMAC-DPS. The linewidth is rising from FWHM= 1.3 mT at $\nu_{mw} = 1\,GHz$ to FWHM= 2.3 mT at $\nu_{mw} = 38\,GHz$. If all measurements are evaluated, the fit parameter of the FWHM linwidth can be plotted versus the resonant magnetic field B_0 to show the dependence of the ELDMR-linewidth. Figure 6.4b now shows clear signs, that m-MTDATA:BPhen shows no magnetic field dependent broadening in the investigated B-field range. In contrast, m-MTDATA:3TPYMB and DMAC:DPS show severe broadening from $\nu_{mw} = 1\,GHz$ to 39 GHz. For all measurements the devices have been placed in a cryostat under constant nitrogen flow at 220 K to minimize degradation effects. Also, to prevent power broadening during ELDMR sweep, the microwave power did not exceed $P_{mw} = 100\,mW$. A more in-depth analysis of the multifrequency-ELDMR broadening regard to the Δg-mechanism is provided in the following section.

6.4 Evaluation of Δg

To properly extract spin parameters like a value of Δg from a magnetic resonance spectrum, Stoll et al. developed a Matlab software toolbox called EasySpin [78]. The software allows spectral simulation and analysis of EPR data by finding the resonance fields of a given spin system by solving the spin Hamiltonian (See Section 3.2). The simulation of cw EPR spectra of disordered systems in EasySpin are done by the simulation function `pepper`. The following starting parameters must be specified in advance:

- `Sys.S=[1/2 1/2];` % specifies the system as two spin $s = 1/2$ carrying particle.
- `Sys.g=[2.002; 2.005];` % sets the g-factors of each spin $s = 1/2$ particles. Here, $\Delta g = 3 \times 10^{-3}$.
- `Sys0.D=[D];` % sets the dipolar interaction to the value given for D in MHz.

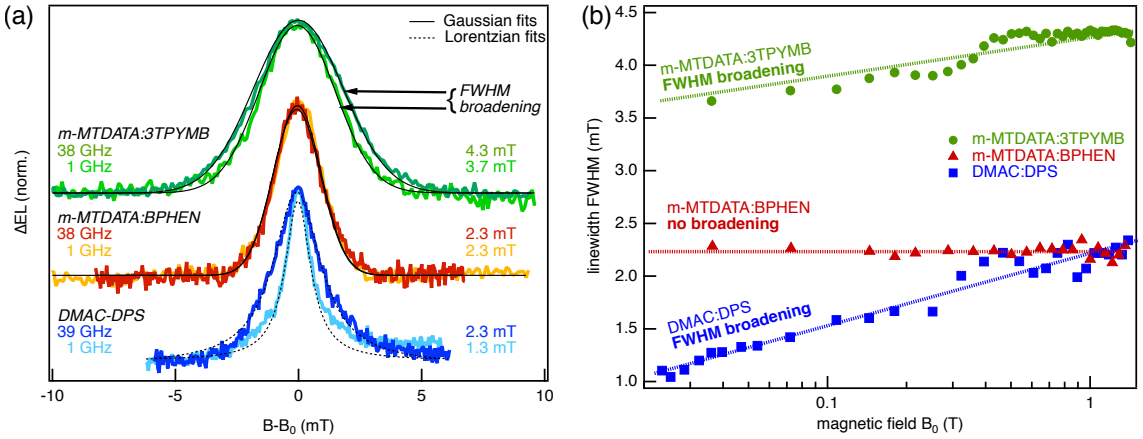

Figure 6.4: : (a) ELDMR spectra of three different material systems: m-MTDATA:3TPYMB (green), m-MTDATA:BPhen (red/orange) and DMAC-DPS (blue). The magnetic field axis is shifted by the resonant magnetic field B_0 to compare low and high frequencies. The resonance of the Donor:Acceptor systems are represented with Gaussian fits, the resonance of the CT-resonance is fitted with a Lorentzian. (b) Magnetic field dependence of the ELDMR-linewidth. While m-MDATA:3PYMB and DMAC-DPS show a significant line-broadening with increasing magnetic field, the linewidth of m-MTDATA:BPhen shows no sign of magnetic field dependent broadening in the investigated range from $\nu_{mw} = 1\,\text{GHz}$ to 39 GHz.

- `Sys0.A=[A]; %` sets the hyperfine interaction to the value given for A in MHz.

- `Sys0.lw=[2.3 0]; %` sets the value for the Gaussian linewidth to 2.3 mT. In contrast, for a Lorentzian linewidth, the second value in the brackets needs to be defined instead.

The parameter of interest here is the difference of the two g-factor values. The influence of Δg is visualized more pronounced in the first derivative spectrum. There, the distance between the magnetic field positions of the maximum and minimum peak increases, when going from low to high microwave frequencies (see Figure 6.5a and b). A EasySpin simulation is shown for $\nu_{mw} = 1\,\text{GHz}$ in Figure 6.5b (i). A splitting of the g-factors was exemplary set to $\Delta g = 3 \times 10^{-3}$, where $g_1 = g_e$ and $g_2 = g_e + \Delta g$ and g_e is the g-factor of a free electron. Since the interest in this work is only on the g-factor, the values for dipolar D and hyperfine A interactions are set to zero and taken into account by a phenomenological fixed linewidth (see above for `Sys0.lw`). If the spectrum is compared to the case in (ii) and (iii), where the resonance position is $\nu_{mw} = 15\,\text{GHz}$ and 39 GHz, a clear shift of the peaks is visible. The dashed line is a guide to the eye at

$g = g_e$. When moving to even higher D-Band frequencies, at $\nu_{mw} = 120\,\text{GHz}$, the EPR line shows a clear splitting. However, this frequency is not accessible in the used setup.

Global fitting of multi-frequency ELDMR

Besides simulations, EasySpin also provides the option of data evaluation by least-square fits. In this fit procedure, each of the spin parameters, which have been explained above, can be used as a fit parameter or a fixed parameter. To keep the fit as simple as possible, D and A are set to zero and treated as a fixed linewidth again, since no magnetic field dependence of these parameters is expected in the examined field range. In addition two g-factors are taken as the second and third fit parameter. To go one step further, we chose three exemplary spectra with different frequency of the data set shown in Figure 6.4 and applied a so-called *global* fit. With this method, all three spectra are fitted at once, or in other words, simultaneously. Global fits should be applied, when datasets "share" a certain parameter. Note that for all spectra, the center of the spectrum was shifted to the resonant magnetic field of the free electron g-factor, since the real g-factor is not known in the experiment and we are not able to assign separate values to the electron and hole. Nevertheless, only the difference in g-factors is desired.

The global fits are shown in Figure 6.5c-e. As shown earlier, the exciplex system m-MTDATA:BPhen shows no FWHM broadening with increasing resonance frequency ν_{mw}. From this fact, it is obvious that the global fit for this material system outputs a vanishingly small value for Δg. The black arrows are a guide to the eye and indicate the low value of $\Delta g = 5.3 \times 10^{-7}$. The Gaussian linewidth for all three measurements is FWHM= 2.3 mT. In contrast, again by only changing the electron acceptor, the exciplex system m-MTDATA:3TPYMB shows a $\Delta g = 2.4 \times 10^{-3}$ at a Gaussian linewidth of FWHM= 3.7 mT (Figure 6.5d). A closer look to the low and high peaks indicates a shift with increasing resonance frequency. With such high value of Δg, a clear splitting of the line would be observed for m-MTDATA:3TPYMB like seen in Figure 6.5b (iv), if the total linewidth of the spectrum would show the same underlying linewidth as m-MTDATA:BPhen. But another different field-independent broadening mechanism is apparently more dominant in m-MTDATA:3TPYMB compared to m-MTDATA:BPhen. The total increase of the linewidth at $\nu_{mw} = 1\,\text{GHz}$ from 3TPYMB to BPhen may be due to the increased number of nuclei leading to a higher influence of hyperfine centers on the total linewidth. Those hyperfine centers could be the higher number of nitrogen and hydrogen atoms in 3TPYMB compared to BPhen. Nevertheless, with the present study, only magnetic field dependence of the linewidth is examined. For further study

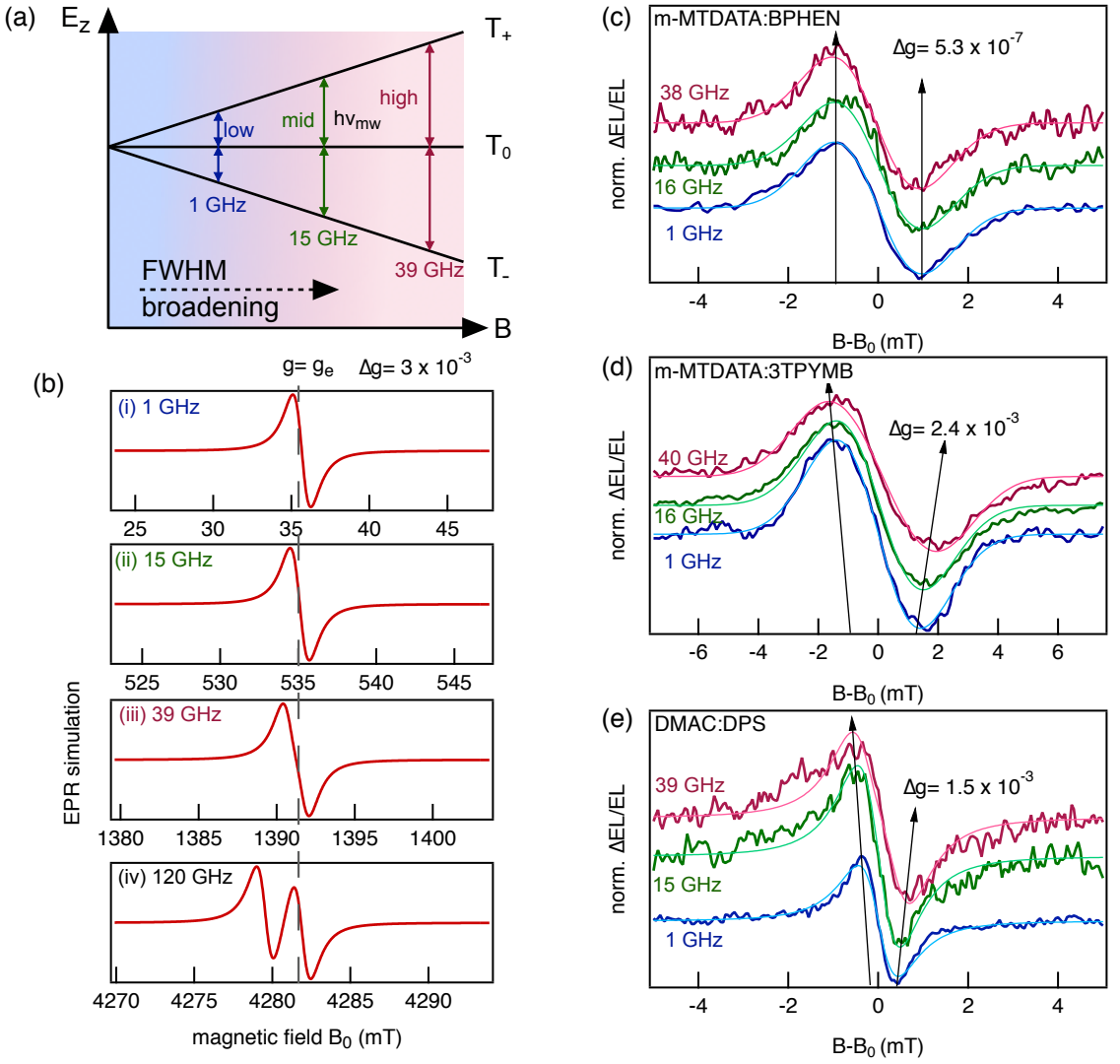

Figure 6.5: (a) Energetic splitting of triplet states via Zeeman interaction. Three exemplary resonance positions (low, mid and high frequency ν_{mw}) are chosen to evaluate the magnetic field dependence of the linewidth due to Δg by a global fit from ELDMR measurements. (b) Exemplary EPR simulations for (i) $\nu_{\mathrm{mw}} = 1\,\mathrm{GHz}$ (ii) 15 GHz (iii) 39 GHz and (iv) 120 GHz for $\Delta g = 3 \times 10^{-3}$ at g-factor $g = g_e$ (c) A global fit is performed simultaneously to the first derivative of all ELDMR spectra of each material system to deduce a value of Δg. The black arrows are a guide to the eye. Vanishing influence was found for m-MTDATA:BPhen with $\Delta g = 5.3 \times 10^{-7}$. (d) m-MTDATA:3TPYMB exhibts $\Delta g = 2.4 \times 10^{-3}$. (e) DMAC:DPS shows g-factor difference of $\Delta g = 1.5 \times 10^{-3}$.

a two-microwave field experiment can be conducted, a so-called hole-burning experiment. It delivers insight into inhomogeneously broadened spectra [94, 95].

6.5 Discussion

The effect of SOC becomes relevant when there are interactions of similar magnitude in the vicinity or when nearly degenerate states exist. Both cases may be the cause of the SOC induced spinflips in TADF molecules. The results of this study underline these arguments by the existence of Δg – a spin-orbit induced line broadening parameter [133]. Nevertheless, it co-exists with non-zero hyperfine effects, which also allow triplet-to-singlet up-conversion. This finding is derived from the field-independent linewidth fraction, which we attribute to hyperfine splitting. Here, we cannot deduce a value of the hyperfine splitting parameter, but give an upper estimate of the total hyperfine influence on the ELDMR linewidth. In absence of Δg in m-MTDATA:BPhen the FWHM= 2.3 mT, which should originate from unresolved hyperfine interactions superimposed with dipolar couplings, both, from the exciplexes with its surrounding nuclei, or in the later case, with neighboring electron/hole spins. For m-MTDATA:3TPYMB the field independent linewidth fraction was found to be FWHM= 3.7 mT. In general, for spin relaxation to occur, there must be a coupling between the mechanical motion of the molecules, such as vibrations, and the magnetic moment of the spins. The type of this coupling and its strength determines the relaxation times and therefore the strength in spin-flip rate. Our results point towards the manifold of TADF emitters. Every material combination, be it donor:acceptor compounds or CT-TADF emitter, contributes to the success of a spin-flip with its own native environment, sometimes more SOC dominated, sometimes more driven by fluctuating HFI fields. The great discrepancy in the line shapes particularly emphasises that fact. For further studies, it might be usefull to explore even higher magnetic field values, to fully dissolve the g-values of all materials. Similarly, the application of pulsed EPR can also provide information as to which of the two processes may be more dominant.

6.6 Conclusion

In conclusion, we probed three state-of-the-art TADF material combinations by their magnetic field dependent resonance linewidth. The resonance lines have been studied intensively in a broad range in microwave frequency from 1 to 40 GHz and simulated with the help of the Matlab tool EasySpin. The donor-acceptor compounds m-MTDATA:BPhen and m-MTDATA:3TPYMB both show severe differences despite their

molecular similarity. m-MTDATA:BPhen exhibits no field-dependent broadening due to low $\Delta g = 5.3 \times 10^{-7}$ and a lower hyperfine influence than m-MTDATA:3TPYMB. This material combinations shows the highest overall linewidth and the strongest broadening due to $\Delta g = 2.4 \times 10^{-3}$. In general, we can summarize that the hyperfine fraction of the linewidth is diminished in CT-TADF emitters compared to exciplex based devices. This type of emitter seem also to be driven by strong SOC effects with $\Delta g = 1.5 \times 10^{-3}$. The result highly encourages the diversity of TADF systems and underline that general statements on the working principle of the RISC driving mechanism have to be made carefully and always considered distinctively for each material combination.

Contributions to this Chapter

Sebastian Weißenseel[1] (S.W.), Andreas Sperlich[1] and Vladimir Dyakonov[1] designed the experiments.
S.W. and Rebecca Bönnighausen[1] prepared the devices and films, measured electroluminescence, device characteristics and magnetic resonance.
S.W. evaluated the data.

[1]Experimental Physics VI, Julius-Maximilian University of Würzburg,
97074 Würzburg, Germany

7 Long-lived Spin-polarized Intermolecular Exciplex States in Thermally Activated Delayed Fluorescence-based Organic Light-emitting Diodes [1]

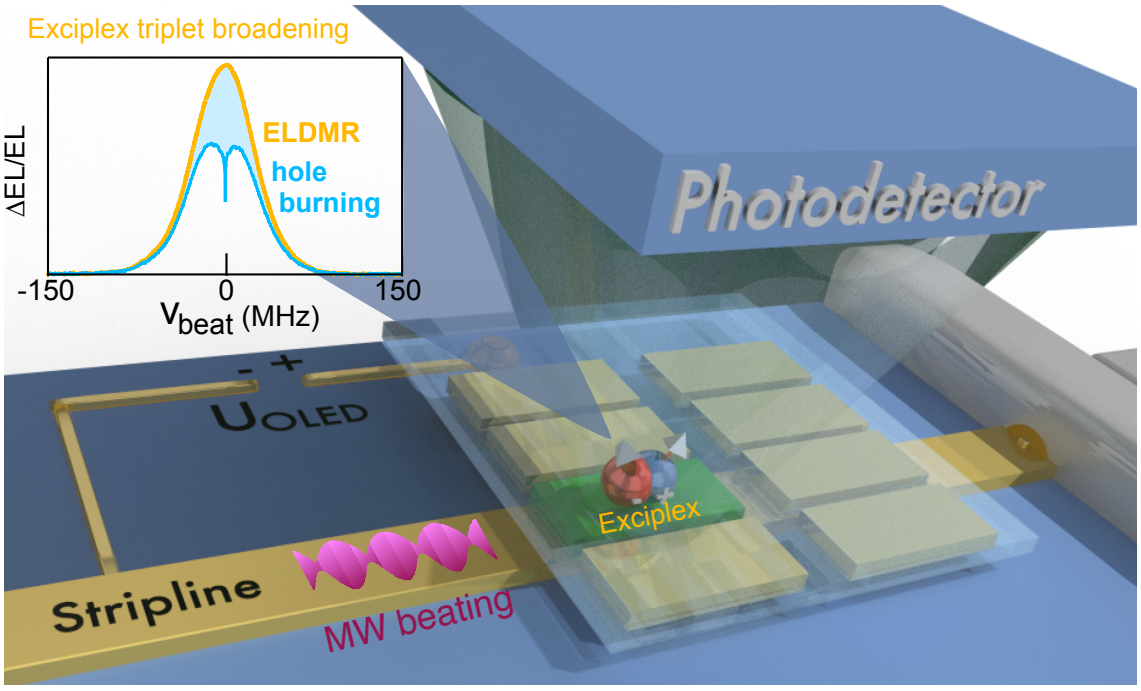

[1] This chapter is based on
Sebastian Weißenseel, Andreas Gottscholl, Rebecca Bönnighausen, Vladimir Dyakonov, Andreas Sperlich. **Long-Lived Spin-Polarized Exciplex States in Thermally Activated Delayed Fluorescence-Based Organic Light-Emitting Diodes.** *Science Advances, 7, eabj9961 (2021)*
doi: 10.1126/sciadv.abj9961

Abstract

We investigate spin-spin interactions in organic light-emitting diodes (OLEDs) and show them to have a strong influence on thermally activated delayed fluorescence (TADF), which takes place via intermediate charge-separated exciplex states. Due to the disordered nature of the donor: acceptor blends, the recombining spin pairs are spatially non-uniformly distributed, resulting in a non-coherent electroluminescence (EL) response to the resonantly induced spin flips and a broad signal. We find that with the two-frequency ELDMR technique, being essentially spectral hole-burning, it is possible to significantly reduce the spectral linewidth by a factor of 5000, i.e. from 62 MHz to 12 kHz. With the hole burning method applied to electroluminescence devices for the first time, we gain access to the dipolar and hyperfine interactions with the complex environment of TADF material. By probing narrow spectral "holes", we are now able to achieve a much more detailed understanding of the spin-spin interactions of the exciplex excited state responsible for the EL emission. By decoupling them from the heterogeneous nuclear environment, we unveil the homogeneous linewidth, which is limited by a spin dephasing time of at least 30 ns. Finally, we observe coherent population oscillations (CPO) – the phenomenon known for two-level quantum systems oscillating at the beat frequency between the pump and probe. We extract an upper limit of the spin relaxation time of 50μs which is longer than the reverse intersystem crossing time constant that limits the quantum efficiency of the OLED. As a result, it is plausible that TADF OLEDs exhibit a high spin polarization of involved triplet exciplexes in operating conditions at room temperature.

7.1 Introduction

The technological development of organic light-emitting diodes (OLEDs) has undergone a remarkable development and the market share of OLED displays in television and smart device applications is growing significantly. Initially started with fluorescence-based emitters with a maximum internal quantum efficiency (IQE) of 25% [9–11], phosphorescent molecular emitters with enhanced spin-orbit coupling (SOC) enabled much higher device efficiencies through singlet-to-triplet intersystem crossing (ISC) [13]. In order to achieve 100% IQE with molecular systems which do not contain heavy elements, the concept of TADF, originally known as E-type delayed fluorescence (DF) [18–21] has been successfully employed in devices and substantially impacted OLED development over the last decade [22–25]. In the TADF or E-type DF process, the first excited singlet state is populated by a thermally activated transition from the first

excited triplet state. The mechanism for harvesting nonradiative triplet states is described as reverse intersystem crossing (RISC). [97, 99–101, 134]. Upon injection of electrons and holes from the contacts in the active layer, which consists of donor and acceptor molecules, intermolecular exciplex states are formed.
In general, such Coulomb-bound quasiparticles can be either in the singlet (spin-0) or triplet (spin-1) state, where the latter should be accurately described by the spin Hamiltonian and, very importantly, can also be selectively controlled, e.g. by an external magnetic field or electron paramagnetic resonance (EPR), to track the population transfer to singlet manifold. Of two possible spin orientations of the exciplex state, EPR can selectively influence (flip) only the spin-1 state, while the effect of the latter is observed in a change of a radiative spin-0 exciplex state recombination. The missing puzzle piece is the connection between these two spin states, as RISC is a first-order spin-forbidden process [124, 135]. However, it can be thermally activated, i.e. as a result of electron-phonon interactions or through the admixture of other spin states, which, for example, enhance spin-orbit coupling, through a Δg-mechanism [63, 82, 83, 136], or due to hyperfine interaction with magnetic nuclei (protons, nitrogen etc.) [29].
In a spin resonance experiment, microwaves with a properly chosen energy (frequency) flip the spin orientation and connect the $m_s = \pm 1$ and $m_s = 0$ substates of a triplet exciplex, which in turn facilitates population transfer to an emissive spin-0 exciplex final state. However, the underlying spin physics is quite complex as the spin-spin interactions in such electron-hole pairs depend strongly on the molecular environment, as well as on the details of how these excited states are created, e.g. optically excited or by injection from electrodes [129–131]. The strength of the spin-spin interaction determines the energy gap between the states $m_s = \pm 1$ and $m_s = 0$, the so-called zero-field splitting (ZFS), and in practice is determined by a spatial distance. As expected, the radii of the e-h pairs in the disordered organic systems have a very broad distribution. Hence, the sought-after spectroscopic precision of the EPR method for manipulating spin states compromises by the fact that the excited spin-pairs (charge transfer states, exciplexes) are broadly distributed in a heterogeneous mixture of molecules, which leads to inhomogeneously broadened envelopes instead of discrete resonance transitions (spin flips) and makes it difficult to access the parameters of the spin Hamiltonian. Here we analyze the role of spin-spin interactions in the light emission of a fully processed OLED using EPR, while tracking the integral electroluminescence (EL) upon injection of a constant current. Most importantly, we were able to disentangle the complexity associated with a broad distribution of spin pairs and propose an original technique to select the fractions of e-h pairs and reconstruct the details of the inhomogeneously broadened ELDMR envelope in this way. For this purpose, a second

microwave source is used in the hole-burning experiment, which pumps and saturates the spin system at a fixed frequency during the probe frequency sweep. Remarkably, this pump-probe method not only allows the separation and addressing of the individual spin packets in the inhomogeneously broadened ELDMR spectrum, but also the observation of coherent population oscillations (CPO), which are observed as spikes with a very narrow linewidth [137–148]. The hole-burning effect is discussed in a picture of the decoupling of the triplet exciplex spin state from the heterogeneous molecular environment, while the CPO is discussed in a picture of a two-level quantum system oscillating with the beat frequency between pump and probe.

7.2 Materials and Spin Physics

The results presented in this work were obtained on OLEDs based on the donor:acceptor system m-MTDATA:BPhen in a device configuration PEDOT:PSS (40 nm) / m-MTDATA (30 nm) / m-MTDATA: BPhen (70 nm, 1 : 1 ratio) / BPhen (30 nm) / Ca (5 nm) / Al (120 nm), as shown in Figure 7.1a, with the pure m-MTDATA and BPhen layers as hole and electron transport layers, poly(3,4-ethylenedioxythiophene):poly(styrenesulfonate) (PEDOT:PSS) as hole injection layer and a mixed layer of m-MTDATA and BPhen as emission layer. A typical j-V-EL curve is shown in Figure 7.1b. The photoluminescence (PL) spectra of the pure materials are shown in Figure 7.1c. The EL spectrum of the device made from the mixed layer is clearly red-shifted and much broader compared to the emission spectra of the pristine molecules. The former is due to the formation of a bound exciplex state at the interface of the two molecules, with the electron localized at the lowest unoccupied molecular orbital (LUMO) of the acceptor BPhen and the hole localized at the highest occupied molecular orbital (HOMO) of the donor m-MTDATA, as schematically shown in the inset of Figure 7.1c [22, 149–151]. The much larger width is probably due to the broad energetic distribution of the emitting states, which we address below.

The electron and the hole both possess a spin of $s = 1/2$. If these particles form a bound exciton, charge-transfer state or an exciplex, the total spin will be either $S = 0$ or $S = 1$. The Hamilton operator, which was introduced in Section 3.2, describing the triplet state is according to [77]:

$$\mathscr{H} = - \underbrace{\boldsymbol{S}_a^T \boldsymbol{J} \boldsymbol{S}_b}_{\substack{e^- e^- \text{ exchange} \\ \text{interaction}}} + \underbrace{\boldsymbol{g} \mu_B \boldsymbol{S} \boldsymbol{B}}_{\substack{\text{Zeeman} \\ \text{interaction}}} - \underbrace{\boldsymbol{S}^T \boldsymbol{D} \boldsymbol{S}}_{\substack{\text{dipolar} \\ \text{interaction}}} + \underbrace{\boldsymbol{S}^T \boldsymbol{A} \boldsymbol{I}}_{\substack{\text{hyperfine} \\ \text{interaction}}} \tag{7.1}$$

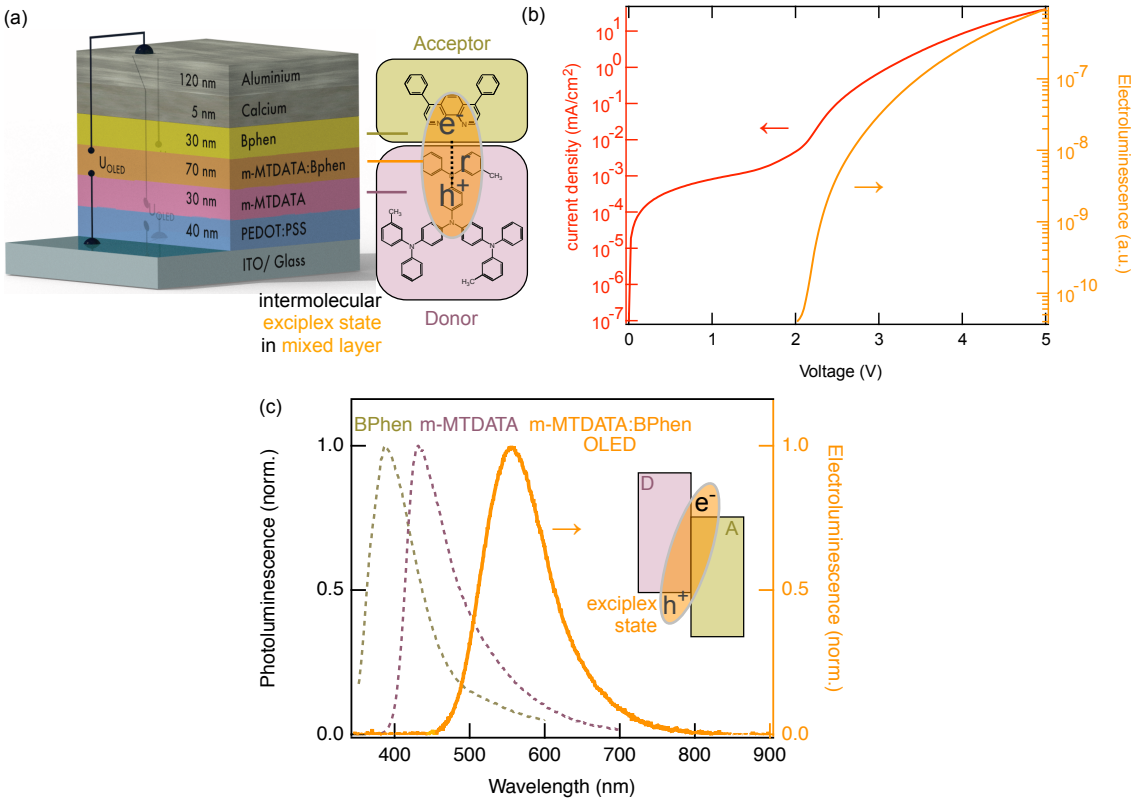

Figure 7.1: (a) Schematic of the m-MTDATA:BPhen OLED architecture. (b) j-V-EL characteristics of a typical m-MTDATA:BPHen device (c) Photoluminescence spectra of pure materials (left axis, dashed lines) and electroluminescence spectrum of an OLED device (right axis, solid orange line). The inset shows the scheme of a bound exciplex state formed at the donor:acceptor interface.

The first interaction term describes the exchange interaction of the two spins S_a, S_b through the orbital overlap of their wave functions, where the exchange integral J determines the energy gap ΔE_{ST} between singlet and triplet energy levels. The second term is the electron-Zeeman interaction with the static external magnetic field B, g is the Landé factor, μ_B is the Bohr magneton, S is the spin operator. The third and fourth terms describe dipolar spin-spin interactions: the electron-spin zero-field interaction (ZFS) and the electron-nucleus hyperfine interaction (HFI), with their respective tensors D for the ZFS and A for the HFI. Quadrupole interaction and nuclear Zeeman splitting are neglected in this work. A schematic representation of ZFS and HFI is shown in Figure 7.2b. The triplet states $m_s = 0$ and $m_s = \pm 1$ are split by the ZFS parameter D. Its magnitude in frequency units is given by the distance r_{ab} between the two interacting spins [84]:

$$D = -\frac{\mu_0 \mu_B^2}{4\pi h} \frac{g_a g_b}{r_{ab}^3} (3cos^2\theta - 1) \tag{7.2}$$

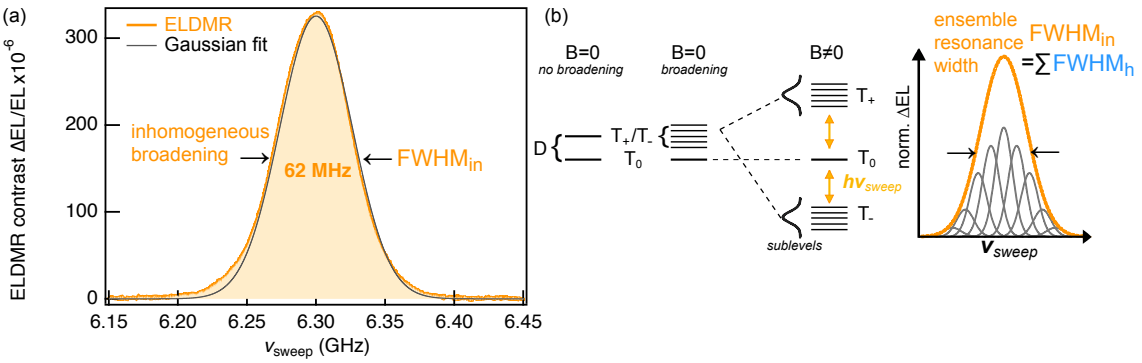

Figure 7.2: (a) Electroluminescence detected magnetic resonance spectrum (orange line) of the m-MTDATA:BPhen OLED in the magnetic field of $B = 225\,\mathrm{mT}$ and the Gaussian fit (black line) with a linewidth of FWHM = 62 MHz. (b) Triplet sublevels with zero-field splitting D may exhibit broadening. The sublevels split in an external magnetic field, resulting in an inhomogeneous lineshape under resonant microwave irradiation with frequency ν_{sweep}.

where g_a and g_b are the Landé factors for spins a and b, θ is the angle between the direction of the magnetic field and the radius vector connecting the two spins. The hyperfine term is given by the interaction of the exciplex triplet with the effective magnetic field of the surrounding magnetic nuclei. This leads to a further splitting of the triplet electronic energy sublevels, where each nucleus contributes with $A_{0,i}$ and the HFI term in Equation 7.1 should be extended by the summation over all nuclei. The total number N_{tot} of HFI-sublevels for i non-equivalent nuclei is then given by $N_{\mathrm{tot}} = (2I+1)^i$. For i equivalent nuclei several HFI-levels degenerate and the total number decreases to $N_{\mathrm{eq}} = (2i \cdot I + 1)$ [73]. Further general details on Hyperfine interaction are given in Section 3.2.4.

In conventional EPR, the external magnetic field is swept at a fixed microwave frequency, resulting in microwave absorption and spin-flip in the sample if the resonance criteria are met. In our work, we study the change in EL under magnetic resonance conditions instead of microwave absorption and this is then called ELDMR. The fully processed OLED is coupled to a stripline circuit that serves as an antenna and generates microwaves that enable frequency sweep at a fixed magnetic field. The relative strength of the effect is evaluated by the ELDMR contrast $\Delta EL/EL$. A detailed description of the ELDMR can be found in Section 4.4.1. In previous publications [129, 130] the singlet-triplet energy gap $\Delta E_{\mathrm{ST}} = 58\,\mathrm{meV}$ was estimated for the MTDATA:BPhen blend, which is by far the largest energy contribution among the spin-spin interaction terms

in Equation 7.1. An example ELDMR spectrum of an m-MTDATA:BPhen OLED device at $T = 220\,\mathrm{K}$ and at $B = 225\,\mathrm{mT}$ is shown in Figure 7.2a, with the microwave frequency ν_{sweep} varied from 6.15 GHz to 6.45 GHz at $B = 225\,\mathrm{mT}$. The spectrum exhibits a featureless shape, which can be fitted with Gaussian with a full width at half maximum of $\mathrm{FWHM}_{\mathrm{Inhomo}} = 62\,\mathrm{MHz}$. This indicates that the ELDMR spectrum is inhomogeneously broadened. The working hypothesis that we verify in the following is that we are dealing with an ensemble of triplet states with different spin-spin interaction parameters and thus transition frequencies, showing up themselves as a featureless envelope, as schematically shown in 7.2b. With knowledge of the details of the broadening of the ELDMR spectrum, e.g., due to the distribution of the spin-spin interaction, the broadening of the EL spectrum can also be better understood and potentially eliminated once it is assigned to a controllable structural or morphological parameter.

7.3 Hole Burning Measurements

To explore the origin of spectral broadening, we apply a two-frequency ELDMR technique realized by introducing a second frequency (ν_{pump}) fixed within the ELDMR spectrum while simultaneously sweeping the frequency ν_{sweep} during the measurement, as schematically shown in Figure 7.3. As illustrated in Figure 7.3a, the dip occurs when the pump microwave field excites transitions between triplet spin sub-levels, and when the power is sufficiently high, it saturates them. The width of the dip is associated to the energetic span of the energy sub-levels in the energy diagram (Figure 7.3a). In Figure 7.3b, a continuous wave (cw) ELDMR spectrum is shown (orange curve). Applying a second microwave frequency results in a sharp dip at the position of the applied pump frequency of $\nu_{\mathrm{pump}} = 6.3$ GHz (Figure 7.3b, blue curve). This so-called "hole-burning" technique is widely used in optical absorption and fluorescence spectroscopy, as well as in spin resonance, but it has never been reported in electroluminescence-detected spin resonance [137–148]. Details on the experiment are given in Section 4.4.2 and 3.3.5 of this thesis.

Characterizing the Hole

To unveil the shape of the "spectral hole" in Figure 7.3b, we subtract the ELDMR spectra recorded with one and two microwave frequencies. (blue shaded region). The resulting spectrum has a distinct shape (Figure 7.3c), with a broad signal and a narrow spike on top. The latter is assigned to the so-called coherent population oscillations (CPO), whose origin will be discussed in detail later. The broad spectrum can be perfectly fitted by the sum of Gaussian and Lorentz functions with respective contributions of

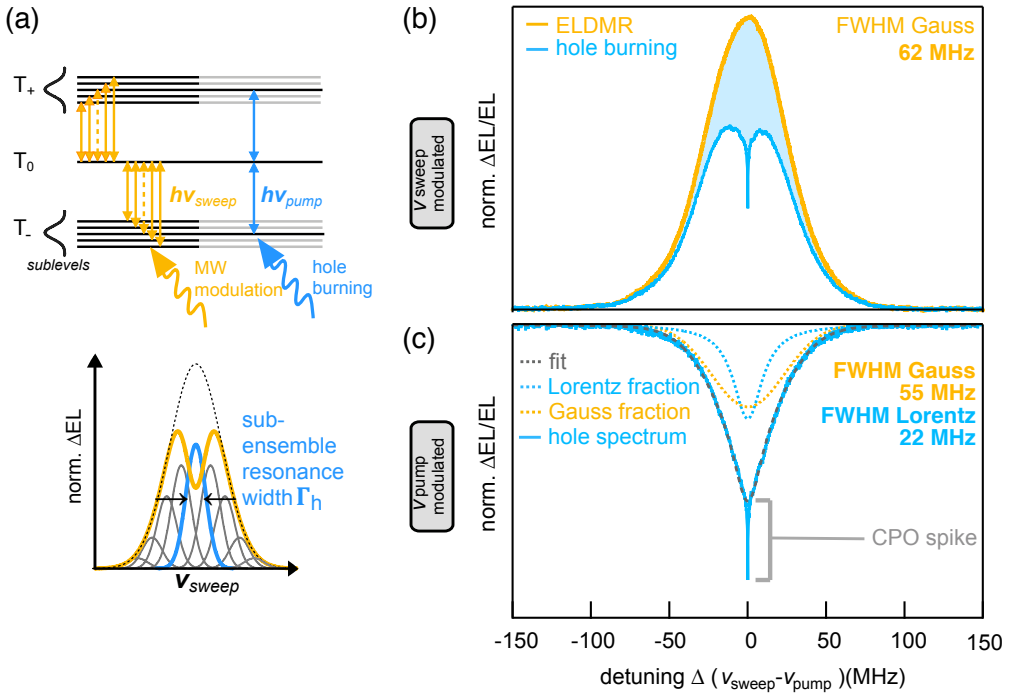

Figure 7.3: Schematic diagram of a hole-burning experiment and the resonant transitions between energetically broadened triplet sublevels with simultaneous applying of a variable (orange arrows) and fixed microwave frequency (blue arrows). (b) ELDMR spectrum (orange) and hole burning (HB) spectrum (blue) of m-MTDATA:BPhen for the frequency sweep of $\nu_{\text{sweep}} = \pm 150\,\text{MHz}$ and $\nu_{\text{pump}} = 6.3\,\text{GHz}$. The sweep frequency ν_{sweep} is modulated "on-off" for lock-in detection and the pump frequency ν_{pump} is kept in continuous wave (cw) mode. (c) The directly measured hole spectrum by modulating the fixed frequency (pump) instead of the swept frequency (probe), as in (b). The signal consists of a broad Gaussian peak ($\text{FWHM}_{\text{Gauss}} = 55\,\text{MHz}$), a narrower Lorentzian peak ($\text{FWHM}_{\text{Lor}} = 22\,\text{MHz}$), and a very narrow spike in the center ($\text{FWHM}_{\text{spike}} = 12\,\text{kHz}$). The fitting curve (dashed black) is a superposition of a Gaussian (dashed orange) and a Lorentzian (dashed blue) contributions.

$\text{FWHM}_{\text{Gauss}} = 55\,\text{MHz}$ and $\text{FWHM}_{\text{Lor}} = 22\,\text{MHz}$, represented by the dashed lines in Figure 7.3c. The Gaussian (55 MHz) background is also known for other spin systems, e.g. color center in diamonds [144], where the exact origin is unclear but possibly results from spin diffusion. This occurs through overlap of individual spin packets (Figure 7.3a) and leads to an inhomogeneous broadening. Therefore, we subtract this contribution to focus on the Lorentzian (22 MHz) spectrum with the homogeneous linewidth determined by a characteristic spin dephasing time t_{deph}, discussed in Section 7.4. Note that the "hole" spectral shape is independent of which of the two frequencies is on/off modulated, ν_{sweep} or ν_{pump}, but since the pump frequency directly saturates a particular transition in the triplet sub-ensemble, we have used it in Figure 7.3c and in the following.

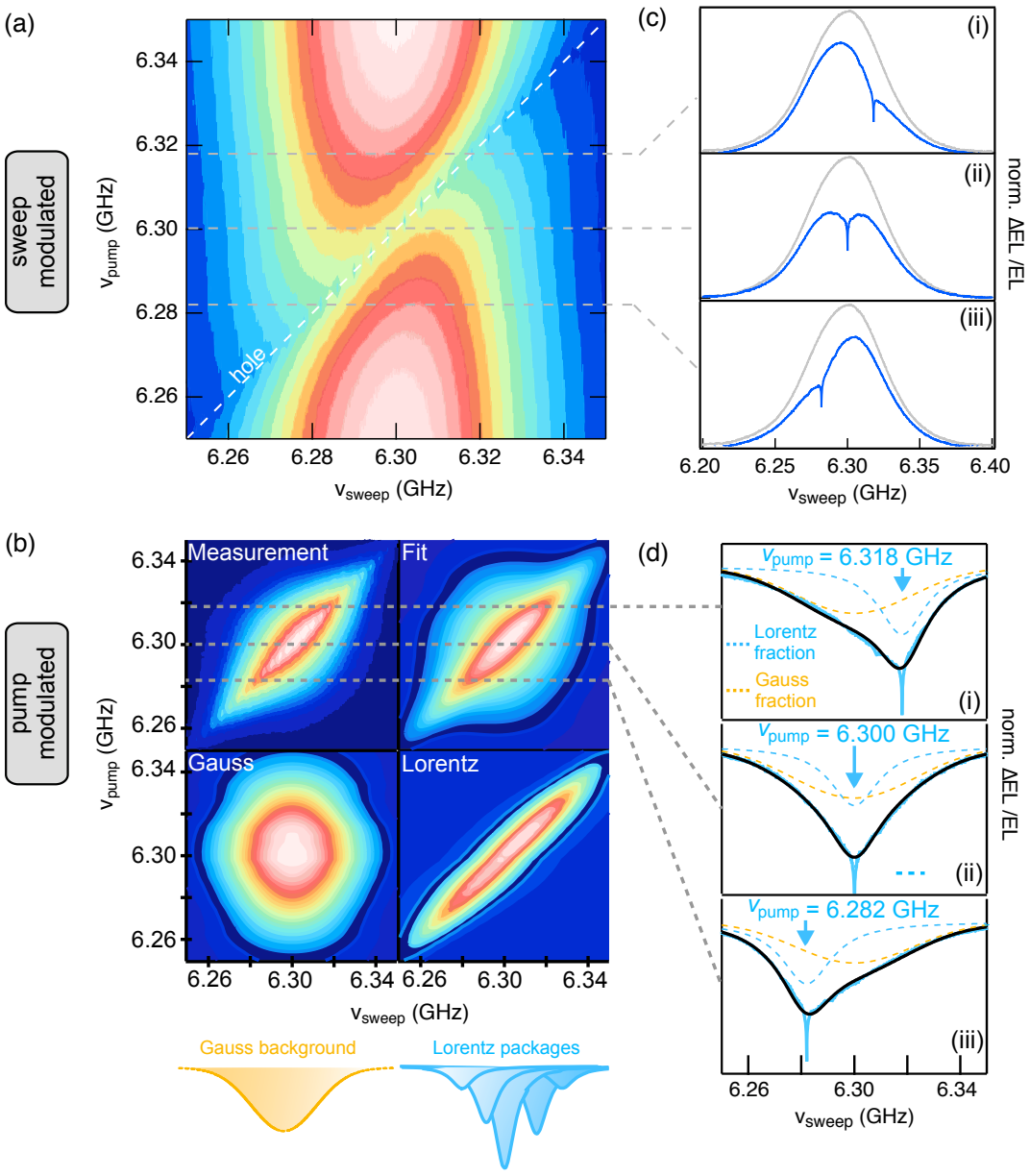

Figure 7.4: Spectral analysis of the hole by varying the pump frequency ν_{pump}. (a) Color map of the hole spectrum as a function of ν_{sweep} and ν_{pump} for on-off-modulation of ν_{sweep} and (b) ν_{pump}. The fitmap in (b) is the sum of the lower two maps. The Gaussian fit is centered at $\nu_{\mathrm{sweep}} = 6.30\,\mathrm{GHz}$. The Lorentzian fit is shifting with ν_{pump}, as shown schematically at the bottom. (c) and (d) are hole contributions as function of ν_{pump}.

We recorded hole burning spectra at a variety of pump frequencies. The measured data can be visualized by a 2D-map, with the x-axis as ν_{sweep} and the y-axis ν_{pump} in a frequency range from 6.250 GHz to 6.350 GHz. With this method, we can compare holes at the edge of the spectrum (e.g. at $\nu_{\mathrm{pump}} = 3.282$ GHz) with holes at the center of the ELDMR spectrum ($\nu_{\mathrm{pump}} = 6.300\,\mathrm{GHz}$). In literature it was shown for systems

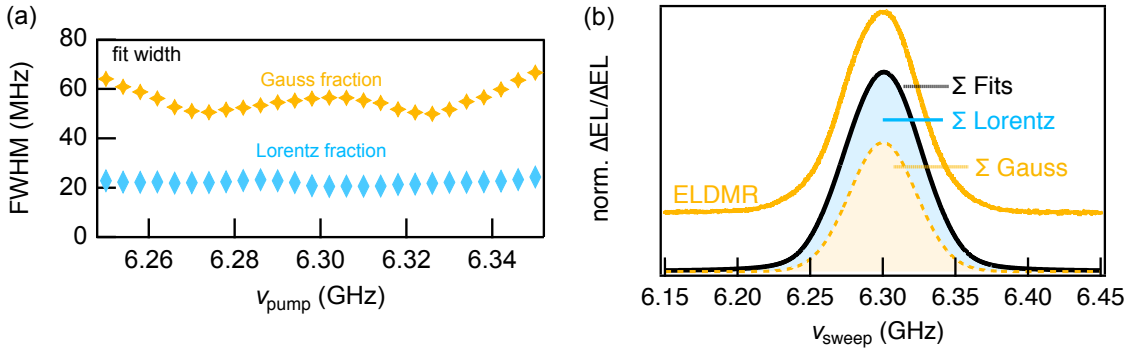

Figure 7.5: (a) Analysis of the fit parameter from the fits shown in Figure 7.4. FWHM for Gauss and Lorentz contributions as a function of ν_{pump}. (b) Reconstruction of the ELDMR signal from the Lorentzian and Gaussian contributions. The sum of all fits has the same linewidth as the ELDMR spectrum FWHM$_{sum}$ = 62 MHz.

with a high ZFS value of several GHz [148], that symmetric holes appear at the opposite side of the spectrum. This indicates that the underlying observed resonant states are coupled by a large D value via the $m_s = 0$ triplet state. In other words, a hole burning experiment at the $m_s = 0$ to $m_s = +1$ transition directly affects the intensity of the $m_s = 0$ to $m_s = -1$ transition. Remarkably, this behaviour is not observed in the present material system. No symmetric holes are visible in the 2D maps in Figure 7.4a and c. The two 2D-maps show, that the hole can be moved through the ELDMR spectrum, without causing any holes on the opposite side. Figure 7.4a and b compare the two possible modulation modes, on-off-modulation of ν_{sweep} and ν_{pump}. Next to the maps exemplary vertical cuts are shown in Figure 7.4c and d for three different pump frequencies ν_{pump}. We can show, that all spectra of Figure 7.4b are composed of a Gaussian and Lorentzian contribution. The 2D-map of the fits is shown next to the "measurement" in Figure 7.4b, the Gaussian and Lorentzian contributions are given below. The red area in the map indicates that the Gaussian contribution to the hole spectrum always exhibits the same center-frequency of 6.3 GHz. The Lorentzian contribution is directly moving with the pump frequency position ν_{pump} of the hole. However, the width of the Gaussian background (55 MHz) is slightly less than the total measured ELDMR linewidth, which is 62 MHz, which could indicate a different origin. To verify this, we evaluated the two contributions separately and used them to reconstruct the experimental ELDMR spectrum. The individual linewidths for Gaussian and Lorentzian contributions are shown in Figure 7.5a. While the FWHM$_{Lor}$ remains constant at 22 MHz and does not change with ν_{pump}, the FWHM$_{Gauss}$ varies between 50 and 62 MHz in the applied range of pump frequencies. As shown in Figure 7.5b, we can perfectly reconstruct the ELDMR spectrum by summing all contributions in the pump frequency range studied. This illustrates that the inhomogeneous broadening of the ELDMR spectrum can be

due to the broad distribution of triplet exciplex states with different spin-spin interactions on the one hand, but possibly also to the spectral spin diffusion of the overlapping spin packets. These broadening mechanisms are discussed in Section 7.6.

Microwave Power Dependence of the Hole

When investigating broadening mechanisms, it is inevitable to discuss influences of the microwave power on the overall linewidth of the resonance signal. A power series of the hole burning experiment is shown in Figure 7.6a. In the case of sweep modula-

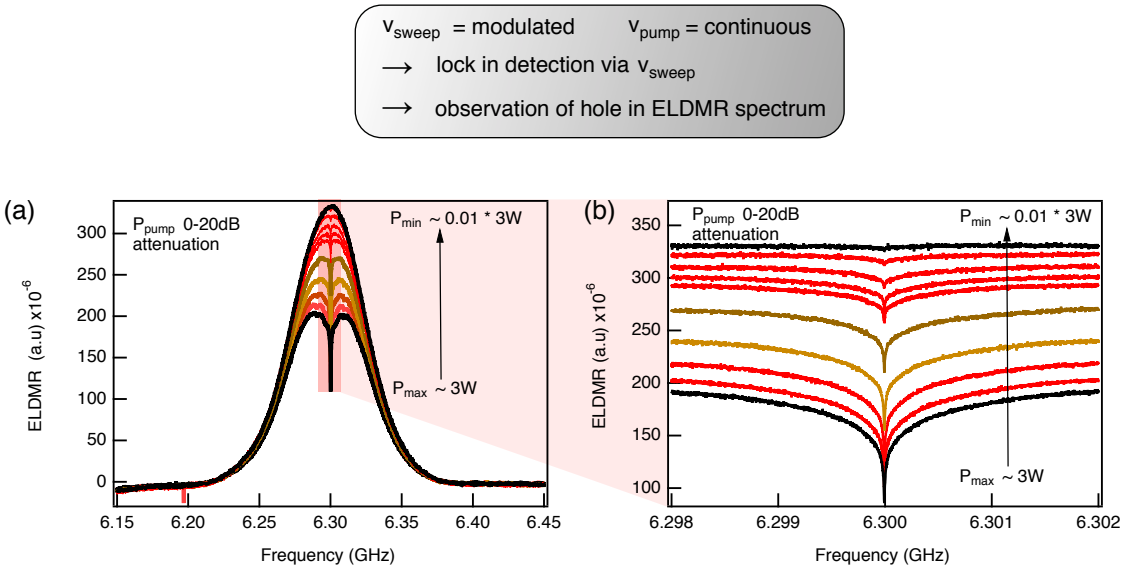

Figure 7.6: Microwave power dependence of hole burning with on/off modulation of ν_{sweep} with a sweep power of $P_{\text{sweep}} \sim 1\,W$. (a) The observation of a prominent hole in the ELDMR spectrum is given at the full available pump power of $P_{\text{max}} \sim 3\,W$. The power can be decreased by an adjustable attenuator. At 1% of the maximum power, the hole is completely vanishing. (b) A zoomed-in measurement of the hole at 6.300 GHz.

tion, by decreasing microwave power of a maximum $P_{\text{pump}} \sim 3\,W$ to $0.03\,W$, the hole burning spectrum approaches the ELDMR spectrum. A detailed view is given in the zoomed-in measurement in Figure 7.6b. Again, to spectroscopically analyze the influence of the microwave power, it is more expressive to detect the EL via modulation of the pump frequency. The power series of the pump modulated experiment is shown in Figure 7.7a. The direct observation of the hole allows to apply again a fit composed of Gaussian and Lorentzian and extract the width and the fit area of the hole. The fit area is shown in Figure 7.7b. The intensity of a magnetic resonance experiment is expected to increase proportional to $\sqrt{P}$ until the spin system is driven to saturation [73]. Both the Gaussian and the Lorentzian fraction of the hole burning signal increase linearly

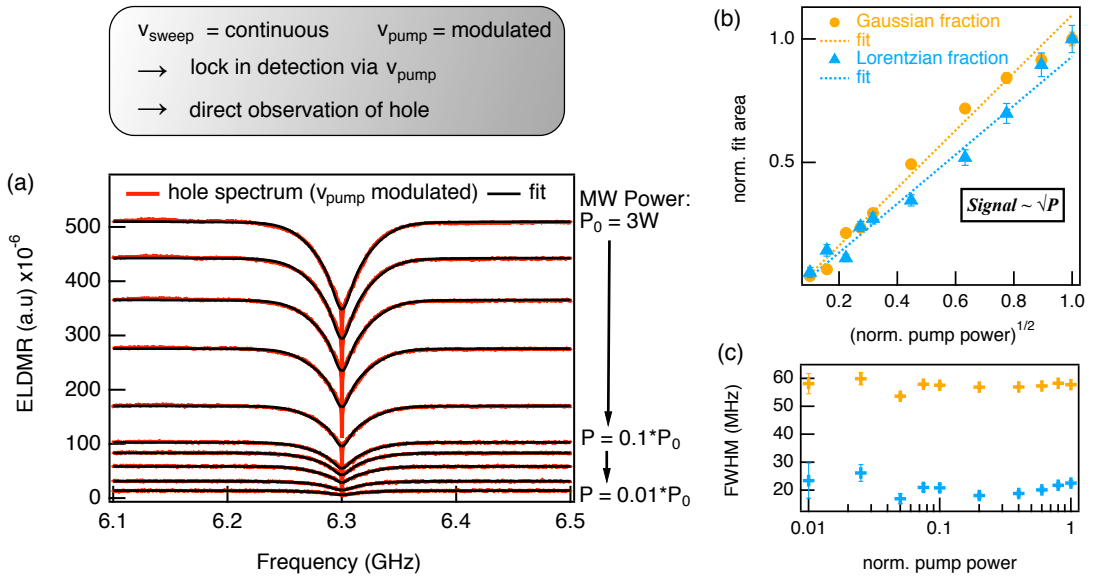

Figure 7.7: Microwave Power dependence of the hole-spectrum with on/off modulation of ν_{pump}. (a) Hole spectra for varying pump powers. (b) The hole intensity is proportional to the square root of the microwave power of the pump generator. There is no saturation of the intensity visible. (c) There is no change in the linewidth of the hole spectrum with increasing microwave power of ν_{pump}, which excludes power broadening.

with $\sqrt{P}$ and do not show any signs of saturation. This experimental fact states that even under very high intensity of microwave pump power $P_{\text{pump}} \sim 3\,W$, the hole burning experiment is not able to saturate the triplet sub-resonance completely. If we want to deduce the linewidth limiting processes from the hole burning experiment, we must exclude any influence on the linewidth by microwave radiation. A detailed look on Figure 7.7c shows that the linewidths of both, the Lorentzian and the Gaussian fraction, show no change under variation of the pump power over two orders of magnitude.

7.4 Coherent Population Oscillations

In the above-mentioned hole burning experiment, we apply two microwave-fields. From a classical point of view, when two electromagnetic waves with close frequencies interfere, a beating oscillation of the intensity occurs with a beating frequency $\nu_{\text{beat}} = |\nu_{\text{sweep}} - \nu_{\text{pump}}|$, where ν_{beat} is the detuning between pump and probe frequencies. It is an analogue to acoustics, where a beating between two frequencies is expressed by a modulation in loudness. We can visualize the microwave beating with the help of an oscilloscope. Due to technical limitations in time resolution, we exemplarily chose

microwaves in the MHz range, to visualize the microwave beating. The two microwave sources have been merged together by a microwave combiner and connected directly to the oscilloscope. The beatings are shown for three different beating frequencies in Figure 7.8.

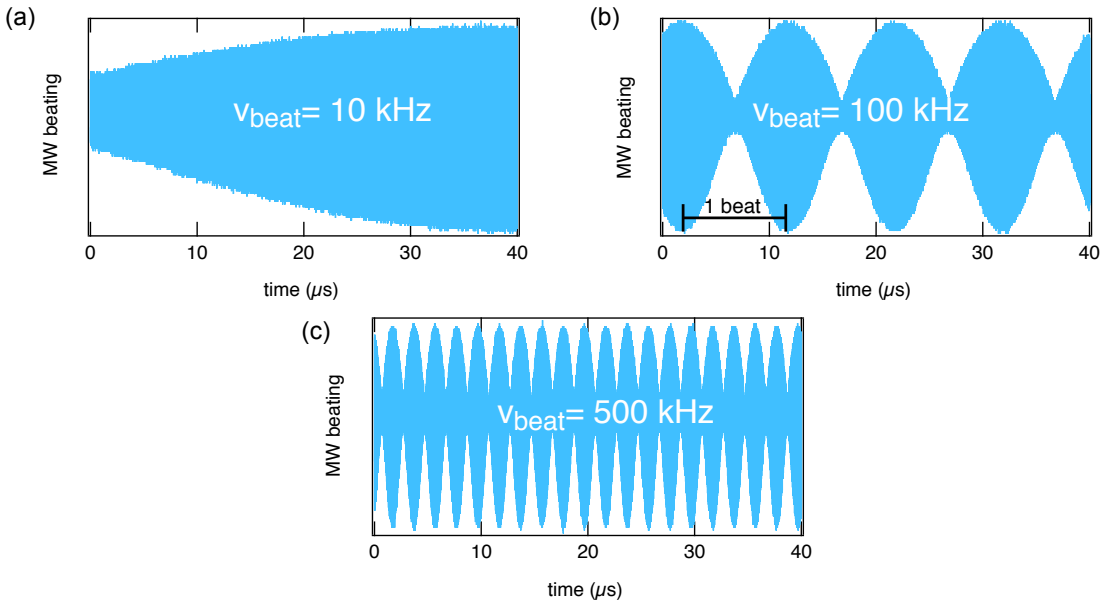

Figure 7.8: Exemplary measurements of microwave beating. The beating frequency is given by $\nu_{beat} = |\nu_1 - \nu_2|$. To visualize the microwave beating with an oscilloscope, the frequencies have been chosen in the MHz range: $\nu_1 = 100.00\,\text{MHz}$ and (a) $\nu_2 = 100.01\,\text{MHz}$ (b) $\nu_2 = 100.10\,\text{MHz}$ (c) $\nu_2 = 100.50\,\text{MHz}$.

However, here, we make use of the microwave beating to produce a modulation of the brightness of the OLED. While the application of a single microwave resonance frequency tends to equilibrate the population of spin sublevels, the simultaneous application of two frequencies can cause the triplet population to oscillate, especially when the beat frequency is in the range of or lower than the inverse spin relaxation time of the spin system. The effect is therefore called coherent population oscillation (CPO) and has been reported for various inorganic spin systems in the past [144, 152–154]. In a lock-in detected ELDMR experiment, as in this work, these oscillations are time-averaged, but this leads to the beat frequency ν_{beat}-dependent depth of the burned spectral hole. If the lifetime of the spin state is controlled by a transverse dephasing time t_{deph} and a longitudinal relaxation time t_{relax}, these time constants will determine the eigenfrequencies of the spin state, and in the case of a forced oscillation with the variable beat frequency, the "hole" depth will be affected. In a continuous-wave (cw) detuning scan, the beating microwave power is varied in beating frequency from several Hz to MHz, and we observe such a very narrow spike on the top of the

hole, as shown in Figure 7.9a. Such CPOs are also known from laser spectroscopy when two electromagnetic waves are simultaneously applied to a two-level system As discussed above, the hole-homogeneous linewidth $\mathrm{FWHM}_h = 22\,\mathrm{MHz}$ allows to estimate the lower limit for the dephasing time

$$t_{\mathrm{deph}} = \frac{2}{\pi \mathrm{FWHM}_h} > 30\,\mathrm{ns} \tag{7.3}$$

while the width of the spike corresponds to the longitudinal relaxation rate. The dephasing time agrees well with the dephasing times estimated from pulsed Rabi experiments measured on similar OLED systems [155, 156]. When switching from frequency space to experimental time, we can assume a simple decay model. The net magnetization of a sub-ensemble of $S = 1$ states formed at $t_0 = 0$, decays exponentially with dephasing time constants t_{deph} and t_{relax}. In the external magnetic field, the triplets also undergo precession with Larmor frequency $\nu_L = \omega_L/2\pi$. Together we can write for the intensity of the net magnetization of a sub-ensemble:

$$I(t) = \left[A \cdot \exp\left(\frac{-t}{t_{\mathrm{deph}}}\right) + B \cdot \exp\left(\frac{-t}{t_{\mathrm{relax}}}\right) \right] \cdot sin(\omega_L \cdot t) \tag{7.4}$$

With intensities A and B. The fast Fourier transform (FFT) of this equation is shown in Figure 7.9b. The fast decay of t_{deph} results in a broad line, while the FFT of the long decay with t_{relax} reproduces the narrow spike. By zooming in the peak in Figure 7.9c & d, it turns out that the shape of the spike is more complex and cannot be perfectly fitted with a single Lorentzian function (Figure 7.9c). Due to inhomogeneous broadening of the involved triplet levels, several frequency contributions are possible here, but the issue cannot be fully elucidated. More details are given in Section 7.5. Nevertheless, the narrowest line is well resolved. The frequency obtained from the Lorentzian fit in Figure 7.9d is $\mathrm{FWHM}_{\mathrm{relax}} = 12\,\mathrm{kHz}$. Additionally, the modulation sidebands of the on-off-modulation with $\nu_{\mathrm{mod}} = 911\,\mathrm{Hz}$ of ν_{pump} appear in Figure 7.9d which rules out the possibility that on-off modulation effects are responsible for the multi-Lorentzian contributions to CPO in the kHz to MHz range. To simulate this system, the model of Mrozek et al. is modified and applied for the present material system in Section 7.5 [144]. From the narrowest width we can estimate an upper limit of the spin relaxation time at a temperature of 220 K:

$$t_{\mathrm{relax}} = \frac{2}{\pi \mathrm{FWHM}_{\mathrm{relax}}} < 50\,\mu\mathrm{s} \tag{7.5}$$

It seems quite counterintuitive to observe population oscillations with a decay time shorter than the RISC time constant, being a slow process that connects triplet and

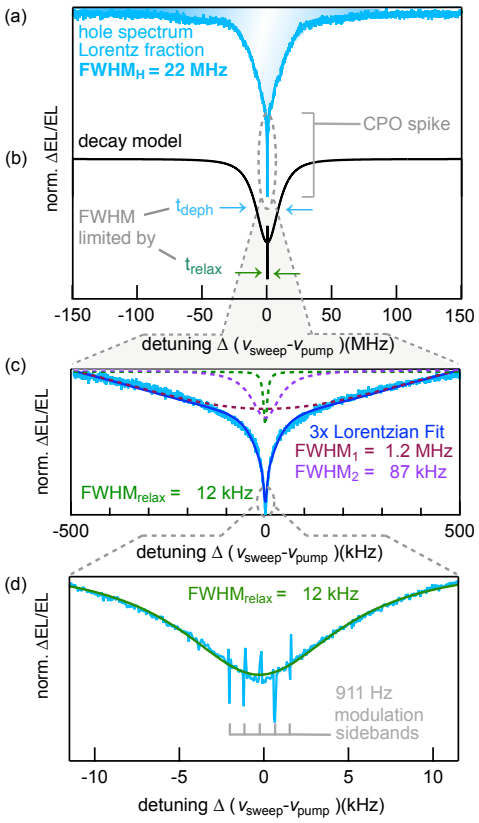

Figure 7.9: Coherent Population Oscillations (CPO) (a) Lorentz fraction of the hole spectrum with CPO spike. We subtracted the Gaussian background from Figure 7.3c for clarity. (b) FFT of the decay model. The FWHM is limited by transversal dephasing time t_{deph} and longitudinal relaxation time t_{relax} (c) Zoomed-in measurement of the hole spectrum. The spike can be described with by one Lorentzian, which results from CPO between triplet levels due to microwave beating between ν_{sweep} and ν_{pump}.

singlet states. According to [130] it is in the range of 30 – 200 ns, therefore the thermalization time of a spin ensemble will be faster than the thermal activation (RISC). This is also supported by the fact that no Rabi oscillations were observed in a pulsed EDMR experiment [155]. However, in a hole-burning experiment, the spin system is driven continuously with an externally forced modulation at the beat frequency. In general, it can be concluded that the spin resonance hole burning experiment in some way samples the temporal behavior of the spin system with the beat frequency ν_{beat}.

7.5 Simulation of Coherent Population Oscillations

To simulate the spike in the hole burning spectrum Mrozek et al. [144] applied a rate-equation model on a two-level quantum system, of which populations oscillates at the beat frequency ν_{beat} between the pump ν_{pump} and sweep ν_{sweep} frequency. In our case the quantum system is more complex. Since the exciplex *triplet* state is observed via ELDMR, we expect a three level system with a small zero-field splitting D. We adapted the model of Mrozek et al. and expanded it to a three level system. Let us denote the triplet population n_i^0 of the i-th triplet state in a quasi equilibrium state under *continuous* microwave radiation $p(t) = p_0$, without *external* driven oscillation. Whereas, the *time-dependent* populations of the triplet states under a oscillating microwave field $p(t) \sim cos(2\pi\nu_{\text{beat}}t)$ are given as $\rho_i(t)$. The change in time of the triplet population is given by $\dot{\rho}_i$. Additionally, the relaxation rates of these levels to recover equilibrium state are considered as γ_i. An oscillating microwave field $p(t)$ drives transitions between the triplet states at the beat frequency ν_{beat}. In the experiment, the net direction of a transition (absorption vs emission) between the sublevels depends on the sign of the population difference of the sublevels. Thus, we can define the rate equation of each triplet sub-level as

$$\dot{\rho}_+ = -\gamma_+(\rho_+ - n_+^0) - p(t)(\rho_+ - \rho_0) \tag{7.6a}$$

$$\dot{\rho}_0 = -\gamma_0\,(\rho_0 - n_0^0) + p(t)(\rho_+ - \rho_0) - p(t)(\rho_0 - \rho_-) \tag{7.6b}$$

$$\dot{\rho}_- = -\gamma_-\,(\rho_- - n_-^0) + p(t)(\rho_0 - \rho_-) \tag{7.6c}$$

where the time dependent microwave field $p(t)$ is given by [144]

$$p(t) = \left\{1 + F\frac{\gamma^2}{\gamma^2 + (\nu_{\text{beat}})^2}\,cos\left[(\omega_0 + \Delta\omega)\,t + \phi\right]\right\} \cdot p_0 \tag{7.7}$$

where p_0 is the pump rate of the system, $\Delta\omega = 2\pi\nu_{\text{beat}}$ is the detuning between the pump and the probe frequency. F is a contrast ratio between the pump and the probe powers. The value γ is calculated by $\frac{1}{\gamma} = \frac{1}{\gamma_-} + \frac{1}{\gamma_0} + \frac{1}{\gamma_+}$. Figure 7.10 shows a simulation of rate Equations 7.6 with the relaxation rates $\gamma_+ = 2\,\text{MHz}$, $\gamma_0 = 10\,\text{kHz}$, $\gamma_- = 220\,\text{kHz}$ (see Figure 7.11b). This set of rates is found to match the envelope of the experimental data. The pump rate is given in units of a Rabi-frequency $p_0 = 222\,\text{Hz}$ and ratio between the pump and the probe $F = 2$. For high values of $\Delta\nu$, the second term in Equation 7.7 vanishes, $p(t)$ approaches a constant value and the triplet system approaches the equilibrium. Since in the present study the hole burning signal was detected via lock-in amplification, the oscillations can not be detected directly. The lock-in detector averages over several phases ϕ of the oscillation (see Equation 7.7). A direct observation of

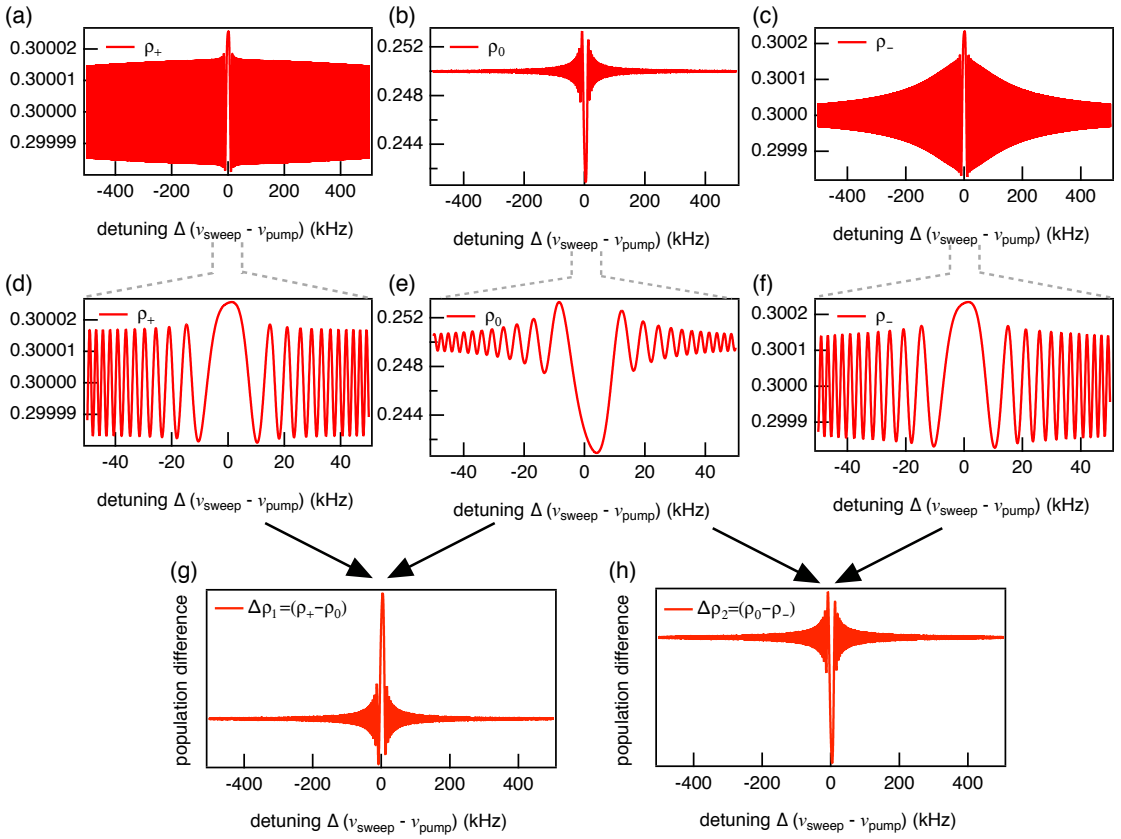

Figure 7.10: Simulation of the Coherent Population Oscillations from equation 7.6. (a)-(c) Simulation of the triplet populations. (d)-(f) zoomed-in populations. (g) and (h) population difference $\Delta\rho_1 = (\rho_+ - \rho_0)$ between the $m_s = 0$ and the $m_s = +1$ and the difference $\Delta\rho_2 = (\rho_0 - \rho_-)$ of the $m_s = 0$ and the $m_s = -1$. The envelope depends on the relaxation rates of the triplet sublevels.

the oscillation with an oscilloscope like done by Mrozek et al. [144] was not achievable due to low signal to noise ratio. The relative change of PL, in other words the ODMR contrast $\Delta PL/PL$ in this particular Nitrogen-vacancy (NV^-) color center in diamond is more than one magnitude stronger than the ELDMR contrast observed for the present TADF based OLED device. Nevertheless, to mimic the averaging effect of the lock-in detector, we calculated the sum of the simulated population differences and applied a low pass filter. The applied model is shown in comparison with the experimental data in Figure 7.11a. It is notable, that one frequency contribution alone can not explain the whole CPO peak. Several line contributions are conceivable, since due to the inhomogeneity of the spin system also non-resonant triplets take part in the oscillations. Likewise, a Gaussian broadening of the states is directly observed in the hole spectrum by the Gaussian fraction in Figure 7.3b.

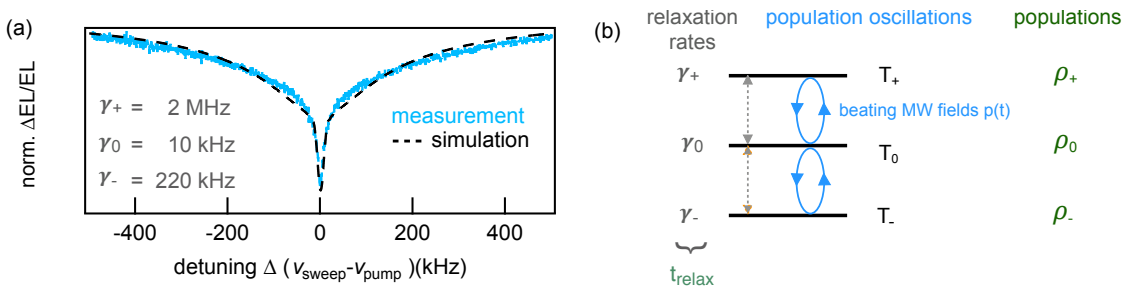

Figure 7.11: (a) Comparison of the CPO simulation and the measurement on a 1 MHz broad detuning sweep. (b) The beating MW fields result in an oscillation of the microwave power. The time dependent power p(t) creates a forced oscillation of the triplet populations. The oscillation frequency of each sublevel is limited by the relaxation rate of each level.

7.6 Broadening Mechanisms: Dipolar and Hyperfine Interactions

After discussing the homogeneous linewidth and CPOs as they are revealed by hole burning, we now focus on broadening mechanisms that lead to the full spectral linewidth of ELDMR. In Section 7.3 we ruled out line broadening effects by high microwave power. In addition, Section 6.4 in Chapter 6 described the influence of Δg on the ELDMR linewidth. Due to a low $\Delta g = 5.3 \times 10^{-7}$ we conclude negligible small influence of Δg on the ELDMR experiment for m-MTDATA:BPHEN. Now, the contribution of dipolar interaction within triplet spin states and then hyperfine interactions with surrounding nuclei are discussed with respect to their influence on the ELDMR linewidth.

Dipolar Interactions

Magnetic resonance spectra of a spin triplet (S = 1, D > 0) ensemble with random orientation show broad spectra of two peaks with two shoulders – so-called powder patterns (see Section 3.3) [73, 157]. The spectral separation of the peak positions is D and the shoulder positions are separated by 2D. We exemplarily simulated triplet spectra for varying D values in Figure 7.12a. We now compare them to the ELDMR spectrum in Figure 7.2a. The spectrum is inhomogeneously broadened to an extent that no peaks and shoulders can be discerned to directly determine the dipolar interaction. Thus, we now derive two different approaches to extract an estimate of the dipolar interaction D.

First, we assume that for a spin triplet with D > 0, the total linewidth of the ELDMR spectrum cannot be narrower than the triplet shoulder separation of 2D. Since no obvi-

ous shoulders are discernible, we use 2×FWHM as an upper limit for 2D or D < 62 MHz. Second, we estimate D by analyzing the fitted hole burning spectra from Figure 7.4b. The intensity of the Lorentzian fits of the hole spectra are plotted in Figure 7.12b. Two overlapping broadened peaks can be discerned. We assume the following model to simulate this spectrum. The main peaks of a triplet powder pattern have a spectral separation of D with additional shoulders with separation 2D. Line broadening can wash out this structure and hide the triplet powder pattern underneath the inhomogeneously broadened Gaussian ELDMR signal. We use EasySpin to simulate a triplet powder pattern with D = 50 MHz without broadening (black trace), with FWHM = 5 MHz broadening (dark grey) and the homogeneous hole linewidth of FWHM_h = 22 MHz. Remarkably, the experimental intensities can be reproduced extremely well with the latter and including simulation uncertainties we derive $D = 50 \pm 5$ MHz for the ZFS. Instead of only delivering an upper limit, this method offers a more direct and precise estimate of D by disentangling inhomogeneously broadened spectra. From the strength of ZFS it is possible to deduce a mean separation distance between electron-hole as [84]

$$r_{e-h}[\mathrm{nm}] = \sqrt[3]{78.05/D[\mathrm{MHz}]}\ \mathrm{nm} \simeq 1.1 - 1.2\,\mathrm{nm} \tag{7.8}$$

The estimated distance is in the expected range for donor:acceptor based exciplexes. In comparison, charge-transfer states (CT) in organic photovoltaic exhibits ZFS < 5 MHz resulting in $r_{e-h} > 2$ nm [158]. Moreover, TADF-CT emitter show less delocalization than exciplexes and ZFS is at least an order of magnitude higher (D > 500 MHz, r_{e-h} < 1 nm) [29, 124].

Hyperfine Interactions with ^{1}H and ^{14}N

To estimate the hyperfine coupling, we need to consider paramagnetic nuclei that can interact with the exciplex state. For m-MTDATA:BPhen this includes ^{1}H protons with a nuclear spin of I = 1/2 and ^{14}N nitrogen nuclei with $I = 1$. We can ignore ^{13}C and other paramagnetic isotopes due to their low abundance. The phenyl rings and the methyl groups of the donor molecule m-MTDATA contribute with $i_H = 48$ protons, while the acceptor BPhen adds $i_H = 16$. Furthermore, m-MTDATA and BPhen contain $i_N = 4$ and $i_N = 2$ nitrogen nuclei, respectively (see Figure 7.1a).
The isotropic hyperfine coupling constant A depends on the overlap of the electronic wavefunction and such nuclei, the so-called Fermi contact interaction [85]. In organic molecular systems, excited spin states such as charge carriers or triplet excitons and exciplexes delocalize over extended molecules or along polymer chains. Wider delocalization includes more interacting nuclei but decreases the average coupling constant

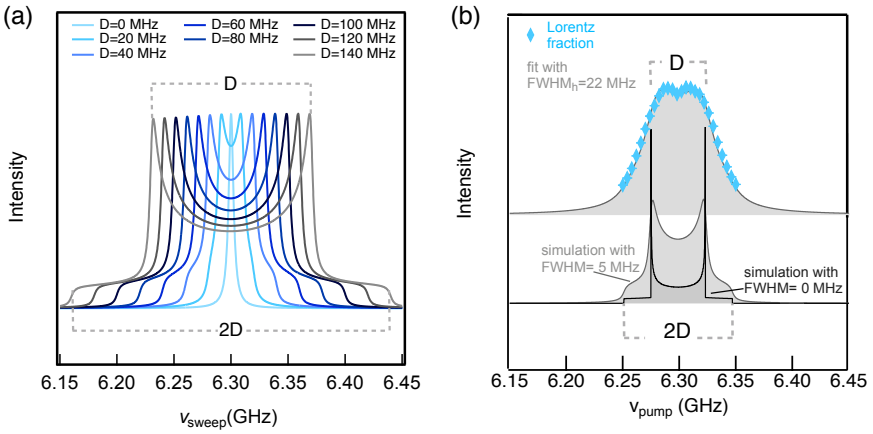

Figure 7.12: (a) Simulation of a triplet spectrum with different values of the dipolar interaction parameter D. The value for D is varied from 0 MHz to 140 MHz. The peaks are separated by D, while the lower-intensity shoulders are separated by 2D. (b) The intensity of the Lorentzian fits of Figure 7.4b (blue diamonds) exhibits two maxima. The data can be simulated (grey line) with a triplet powder pattern with a ZFS of $D = 50$ MHz (peak-to-peak separation) if a homogeneous linewidth of $\mathrm{FWHM}_h = 22$ MHz is assumed. For comparison: the same triplet powder pattern is simulated with FWHM= 5 MHz and FWHM= 0 MHz (grey spectra).

A. We discuss literature examples for ^{1}H and ^{14}N HFI and compare them to the presented exciplex system to restrict the range of possible values for A.

Electron-proton hyperfine interactions have been shown to influence the linewidth of electron spin resonance experiments for various material systems [159–162]. Investigations of charge-separated states in polymer:fullerene bulk-heterojunctions considering ^{1}H protons along the side of polymer chains revealed upper limits for $A_{H,max}$ in the range of $2-3$ MHz [160] or $4-5$ MHz for different polymers [161]. For exciplexes in a donor:acceptor TADF system 5.5 MHz have been determined as an upper limit for $A_{H,max}$ [156]. These moderately small upper limits for HFI constants are caused by the negligible electronic wavefunction overlap with protons that are located at the edges of molecules and are not part of the conjugated electron system. Furthermore, as these are upper limits, average values for A_H will be even lower in these systems. Meanwhile, the molecular extent of these systems is approximately comparable to m-MTDATA:BPhen, which would be an argument to expect A_H of similar magnitude.
The HFI with ^{14}N nuclei directly incorporated within the conjugated system can be much larger. For a donor-bridge-acceptor molecule with triplet biradical character and two equivalent nitrogen nuclei, $A_N = 20$ MHz was reported [163]. Further examples

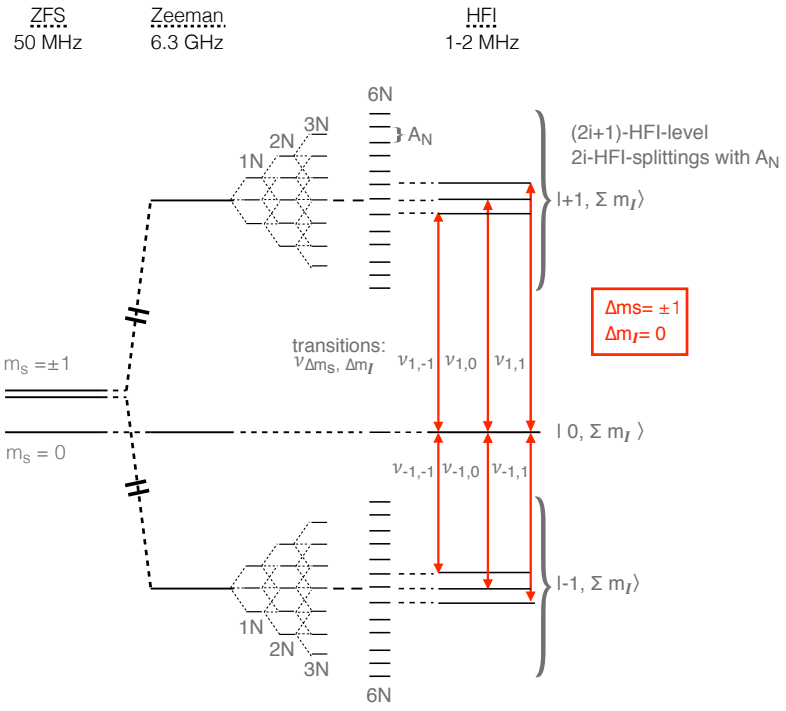

Figure 7.13: (a) Energy diagram of for a triplet exciplex including all relevant spin-spin interactions (not to scale). In absence of a magnetic field B, only the ZFI $D = 50 \pm 5$ MHz between the $m_s = 0$ and the $m_s = \pm 1-$ states is present. At a resonant magnetic field of $B = 225$ mT the $m_s = \pm 1$ level further split into an upper and a lower triplet level by the Zeeman interaction of 6.3 GHz. These levels possess a hyperfine structure depending on the number and interaction strength of surrounding magnetic nuclei. Transition rules allow only $\Delta m_s = \pm 1$ changes while maintain $\Delta m_I = 0$. Hyperfine levels overlap due to finite resonance widths. Note, that a hole burning experiment saturates multiple HFI levels, but not all at once.

for strong A_N HFI are the triphenylamine-derivative cation with $A_N = 25$ MHz [164] or the trioxytriphenylamine cation with $A_N = 25$ MHz [165]. The exciplex triplets discussed in this work have a wider wavefunction delocalization interacting with up to $i_N = 6$ nitrogen nuclei per exciplex. Therefore, smaller values for A_N are to be expected ($A_N \leq 25$ MHz), but the dominating HFI with the exciplex remains HFI with ^{14}N. The number of ^{14}N nuclei $i_N = 6$ leads to $n_{eq} = 13$ HFI-levels if equivalent contribution of all ^{14}N is assumed. With this assumption, we can derive an upper limit of the interaction strength, by dividing the $\text{FWHM}_{\text{ELDMR}}$ by the number of possible splittings. For $n_{\text{eq}} = 13$ HFI-levels, we expect $2 \cdot i_N = 12$ splittings with magnitude A_N (Figure 7.13). We obtain an upper limit for the A_N by the following assumptions:

- Considering only A_N and ignoring A_H, the width of the inhomogeneously broadened spectrum is dominated by D and A_N

- For $n_{eq} = 13$ HFI-levels, we expect $2 \cdot i_N = 12$ splittings with magnitude A_N (Figure 7.13)
- Compare the difference of the lowest and highest frequency transitions in Figure 7.12
- lowest frequency is given by: $g\mu_B B + D + \sum A_N I = g\mu_B B + D + 6A_N$
- highest frequency is given by: $g\mu_B B - D - \sum A_N I = g\mu_B B - D - 6A_N$
- difference of the two: $2D + 12A_N$
- shoulder-to-shoulder powder pattern linewidth corresponds to $\sim 2\times$ FWHM$_{\mathrm{ELDMR}}$

Together we estimate the HFI strength by the maximum shoulder position and the difference between the highest and lowest transition frequency to

$$A_N \leq \frac{2 \cdot FWHM_{\mathrm{ELDMR}} - 2 \cdot D}{2 i_N} = 2\,\mathrm{MHz} \tag{7.9}$$

The interaction with one ^{14}N-nucleus results in $A_{N,i=1} \leq 12$ MHz, while for six ^{14}N-atoms $A_{N,i=6} \leq 2$ MHz (Figure 7.13, right). Together with the assumption from the literature, with the hole burning and ELDMR results we can give an upper limit of $A_N \leq 12$ MHz for the exciplex hyperfine interaction. For further verification of this estimation, we apply an EasySpin simulation in the following.

Simulation of Line Broadening due to Hyperfine Interactions

As a next step, we include hyperfine interactions into EasySpin simulations to explain the Gaussian broadening of the ELDMR spectrum and describe it by unresolved hyperfine interactions. The number of nuclei interacting with an m-MTDATA:BPhen exciplex will be determined by the ^{14}N nuclei ($i_N = 6$), directly incorporated into the conjugated system, and the surrounding protons ^{1}H ($i_H = 64$). As mentioned earlier, we expect that the ^{14}N predominates the linewidth. In the following we thus discuss an example that considers only the influence of the nitrogen. Slightly different parameters would still yield the same result: a distribution of electron-nuclei interactions leads to Gaussian lineshapes with unresolved hyperfine interactions. In Figure 7.13 we discussed that a hole burning experiment excites only a subset of all available triplet levels. Exemplary, here we assume a mean interaction of three nitrogen nuclei and omit the influence of the protons. Further, a distribution of A_N due to disorder in the organic film is to be expected. The dihedral angles of the phenyl rings of the donor and acceptor molecules

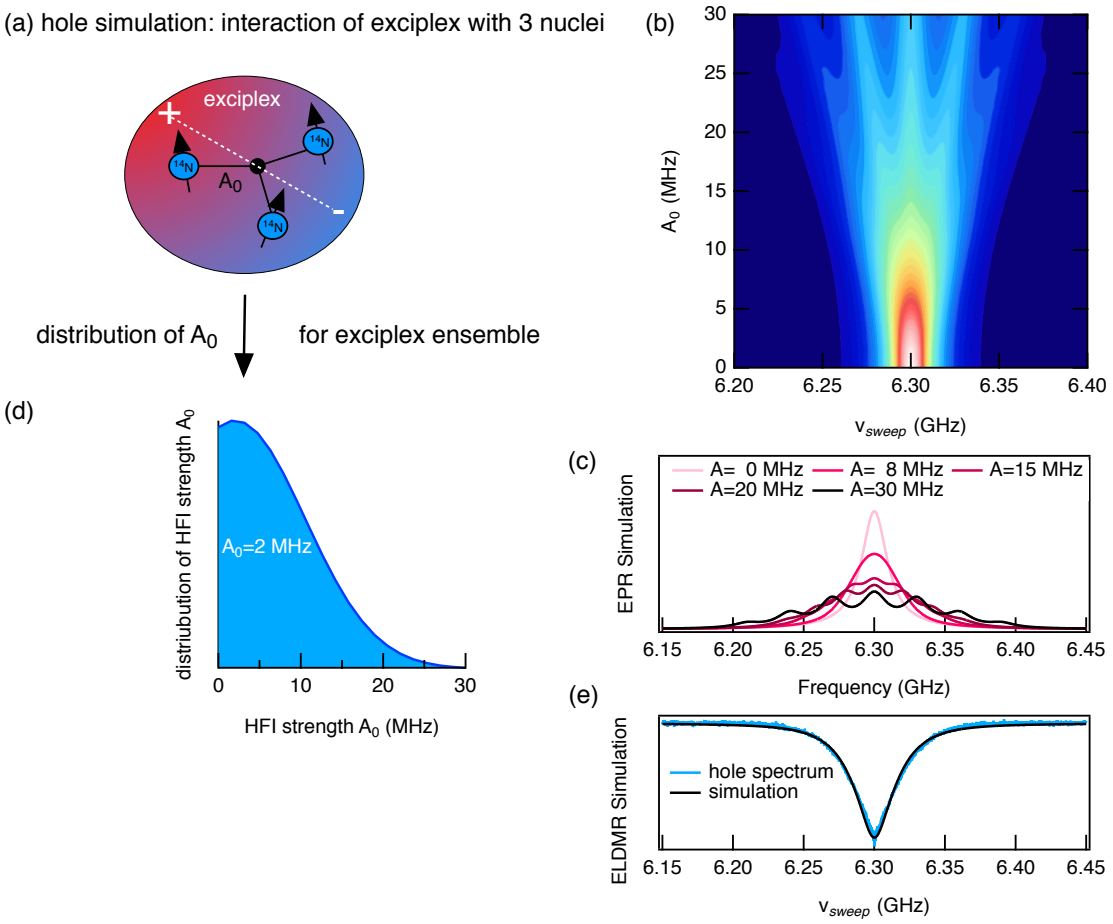

Figure 7.14: EasySpin simulation of a triplet sub-ensemble with interaction of three nuclei. (a) Schematic configuration of three nitrogen nuclei interacting equivalently with the exciplex. The disorder in an organic film suggests a distribution of A_N values due to variations in the dihedral angles of phenyl groups. (b) 2D-map of several HFI simulated spectra with HFI strengths varying from 0 MHz to 30 MHz. (c) Exemplary HFI spectra with varying HFI strengths A_N (d) Weighting function for A_N (e) By summation of all spectra from Figure (b) with weighted intensity for A_N, a mean value of A_N = 2 MHz was found to explain the line shape of the hole spectrum.

vary, which results in a change of geometry that can break the conjugation and prevent wavefunction delocalization over the full molecule. This again changes the spin density of the exciplex at the spatial coordinates of the nuclei and HFI strength A_N. Here, we calculate the triplet spectra for an exciplex interacting with three nuclei (Figure 7.14) with a variation of A_N from 0 MHz to 30 MHz. The homogeneous linewidth is fixed to FWHM$_h$ = 22 MHz. Exemplary spectra are shown in Figure 7.14b and c. The intensity is weighted with a distribution with A_N = 2 MHz and $A_{N,FWHM}$ = 20 MHz. The distribution is shown in Figure 7.14d. The summation of the weighted spectra is shown in Figure 7.14e black curve. Maximum values up to 30 MHz are needed to explain the broad shoulders of the hole spectrum. If the mean value of the distribution is

shifted to higher values, discrete hyperfine shoulders form in the simulation in Figure 7.14e. Since these features are not observed in the hole spectrum, we conclude that our estimation of $A_N \leq 2\,\mathrm{MHz}$ is appropriate.

7.7 Discussion

Finally, in order to relate the evaluated relaxation time back to the spin states which are responsible for the operation of the OLED device, the consequences of a long t_{relax} of the exciplex triplet states will now be discussed. We start with injecting charge carriers into the device which are in principle not spin-correlated. The exciplex singlet and triplets are formed spin-statistically with a 1:3 ratio. The singlets decay within nanoseconds after an electron and a hole meet at the donor:acceptor interface with total spin $S = 0$. The exciplex triplets need to undergo RISC in order to emit a photon. The observation of a long spin relaxation time t_{relax} in the electrically driven OLED devices and thus high spin polarization in the triplet sublevels clearly indicates that the RISC rates of the $m_s = 0$ and $m_s = \pm 1$ triplets must be different.

The RISC timescale of $30 - 220\,\mathrm{ns}$ of the present material system is much shorter than the spin relaxation $t_{\mathrm{relax}} < 50\,\mu\mathrm{s}$ [130]. This means, that the spin-polarization is not quickly equalized and present even in the electrically driven device. Comparing the observed time constant with other organic devices, their t_{relax}-time is in the same order of magnitude with $30\,\mu\mathrm{s}$, measured by electrically and optically detected magnetic resonance (EDMR, ODMR) [166–169]. The much larger ZFS of $D = (50 \pm 5)\,\mathrm{MHz}$ decouples the electron spin system from the nuclear environment, which results in a long spin relaxation time. It is also worth mentioning that this decoupling takes place even without an external magnetic field, since ZFS outperform HFI. It is also interesting to compare the RISC time constants of other TADF systems. The time constants for donor:acceptor exciplex molecular TADF materials were reported around $0.5\mu\mathrm{s}$ - $30\mu\mathrm{s}$, which is in all cases shorter than the here observed t_{relax} [22, 115, 170–176]. In this case, a strong spin polarization between the $m_s = 0$ and $m_s = \pm 1$ levels can be expected for all TADF systems with long t_{relax}. This has far-reaching consequences for OLED efficiency, especially at high current densities in the efficiency roll-off range, where long-lived triplet sates cause triplet-triplet annihilation [24, 97, 171]. Fast spin relaxation is desirable for future TADF systems, which can be achieved, for example, by increasing spin-orbit coupling.

On the other hand, the short spin dephasing time $t_{\mathrm{deph}} > 30\,\mathrm{ns}$ most likely has no influence on the operation of the OLED. The coupling of nitrogen and protons is known to be the reason for rapid loss of phase coherence [177] with short t_{deph}. The fact that

the spin dephasing constant is quite shorter than the RISC rate suggests that t_{deph} does not affect the RISC process of the exciplex ensemble in a TADF OLED.

7.8 Conclusion

To conclude, for the first time we showed ELDMR hole burning spectroscopy in a model donor-acceptor system m-MTDATA:BPhen that enables TADF in OLEDs. The two microwave double-resonance technique delivers insight into the highly inhomogeneously-broadened triplet states in an electrically driven OLED device by analysing the spectral hole. We found that the homogeneous linewidth of $\mathrm{FWHM}_h = 22\,\mathrm{MHz}$ of these triplet states is limited due to spin dephasing with a characteristic time constant of $t_{\mathrm{deph}} > 30$ ns. Coherent population oscillations are found to cause a sub-natural spike on top of the hole spectrum of $\mathrm{FWHM}_{relax} = 12\,\mathrm{kHz}$, from which we estimate a spin-relaxation time $t_{\mathrm{relax}} < 50\,\mu\mathrm{s}$. Remarkably, a Gaussian background was observed in the hole spectrum, which is presumably due to a zero-field interaction of the underlying exciplex states of $D = 50 \pm 5\,\mathrm{MHz}$, indicating exciplex states of 1.1 nm - 1.2 nm extent. Unresolved hyperfine interactions with surrounding nitrogen and hydrogen nuclei are of a magnitude of $\mathrm{A}_N, \mathrm{A}_H < 2\,\mathrm{MHz}$. Ultimately, spectral overlap of the spin packages causes decoherence and shortening of t_{deph}, while maintaining z-magnetization. The long t_{relax} (<50 μs) $\gg t_{\mathrm{RISC}}$ (30 - 200 ns) means that the OLED spin system will be highly spin-polarized even when operated at ambient temperatures.

Contribution to this Chapter

Sebastian Weißenseel[1] (S.W.), Andreas Gottscholl[1], Rebecca Bönnighausen[1], Andreas Sperlich[1] and Vladimir Dyakonov[1] designed the experiments.
S.W. prepared the devices and films, measured electroluminescence, device characteristics and magnetic resonance.
S.W. evaluated the data.

[1]Experimental Physics VI, Julius-Maximilian University of Würzburg,
97074 Würzburg, Germany

8 Summary

Spin states build the relevant basis for the working principle of organic light-emitting diodes (OLEDs). The direct investigation of these states under electrical operation has rather been a white spot in the literature. In this work, the goal was to contribute to fill this gap and to investigate the involvement of spin states in the fundamental processes in organic semiconductors. The variety of materials studied in this work stems from the recent approach of using molecules whose emissive states can be thermally activated to enhance OLED efficiency. The so-called thermally activated delayed fluorescence (TADF) enables an energetic up-conversion from dark triplet states to luminous singlet states. The spin-spin interactions responsible for this mechanism are investigated in this work by using methods based on the spin-sensitive electron paramagnetic resonance (EPR). In particular, this method has been applied in an advanced manner to electrically driven OLEDs. The paramagnetic resonance has been detected by electroluminescence, which gives the method its name: Electroluminescence detected magnetic resonance (ELDMR).

An entry into the first experimental study of this thesis was provided by the investigation of the novel deep blue TADF emitter SBABz4, whose emission properties strongly depend on the geometrical arrangement of its molecular units. SBABz4 was designed and synthesized by collaborators at the École Polytechnique Fédérale de Lausanne (EPFL), Switzerland. The peculiarity of the design was the stick-like geometry of the molecule, which significantly influences the out-coupling efficiency from the OLED device. The horizontal orientation of the emission transition dipole moment was found by collaboration partners from Augsburg to be 80 %. This thesis showed that the process of reverse intersystem crossing (RISC) strongly depends on the emitters dihedral angle θ between its donor and acceptor unit. The spin-spin interaction that sets the energy gap ΔE_{ST} between singlet and triplet thus strongly depends on this angle. Theoretical simulations of the collaboration partners showed that a perfect tuning between maximum angle ($\theta \sim 90°$) for efficient up-conversion and minimum angle for efficient emission properties ($\theta \sim 0°$), i.e. oscillator strength f, is necessary. The energy gap between singlet and triplet was determined to be $\Delta E_{\mathrm{ST}} = 72 \pm 5\,\mathrm{meV}$ by transient electroluminescence and transient photoluminescence. Activation energy could be linked

to a mean dihedral angle of $\theta \approx 70 - 75°$ between the donor and acceptor units, which deviates decisively from $\theta = 86°$ for a relaxed molecule in vacuum. The work highlights the importance of balancing a small energy gap for efficient TADF with sufficient oscillator strength for future design concepts for upcoming OLED generations.

To generate a deeper physical understanding of commercially available TADF molecules, the magnetic resonance based method ELDMR was applied in a second study. The underlying physics of the thermal up-conversion of the triplets to singlets still raises open questions in the literature. At this point of the thesis, the magnetic field dependence of the linewidth of the ELDMR spectra was evaluated. The information from this allows conclusions to be drawn about mechanisms involved in the RISC process. The Δg-mechanism could be identified as a companion in RISC process. A value for the g-factor difference Δg between electron and hole was obtained for the following material combinations: While for m-MTDATA:BPHEN no broadening was observed due to low $\Delta g = 5.3 \times 10^{-7}$, m-MTDATA:3TPYMB ($\Delta g = 2.4 \times 10^{-3}$) and DMAC-DPS ($\Delta g = 1.5 \times 10^{-3}$) show strong hints of spin-orbit-coupling effects contributing to RISC. The results underline the great diversity of TADF emitters and emphasize that generalized statements on the working principle of the RISC driving mechanism have to be made carefully.

In a final study, we investigated the ELDMR linewidth of the TADF material m-MTDATA:BPHEN in more detail to get to the bottom of the origin of the inhomogeneity of the ELDMR spectrums width $\mathrm{FWHM_{Inhomo}} = 62\,\mathrm{MHz}$. A method that was particularly well suited for this purpose was the double-resonance experiment of spectral microwave hole burning. In this advanced EPR method, an irradiating pump microwave frequency saturated individual EPR transitions, which then no longer participated in the probe frequency detected ELDMR. The saturation of these states generated a spectral hole in the ELDMR spectrum, from the shape of which further properties could be drawn about the TADF material. The innermost of the hole is limited by the spin relaxation times of the underlying exciplex state. The hole was found to consist on the one hand of a broad homogeneous line of $\mathrm{FWHM_h} = 22\,\mathrm{MHz}$, and on the other hand of a spectral peak with a sub-natural line width of $\mathrm{FWHM_{relax}} = 12\,\mathrm{kHz}$. The latter has its origin in beating effects in the OLED spin system due to an oscillating microwave field, which is created by beating of the two microwave radiations of the pump and the probe frequency. The homogeneous linewidth delivered a lower limit to a transversal dephasing time $t_{\mathrm{deph}} > 30\,\mathrm{ns}$, while the peak linewidth could be referred to as an upper limit of the longitudinal relaxation time $t_{\mathrm{relax}} < 50\,\mu\mathrm{s}$. With the aid of spectral microwave hole burning, the spin-spin interactions in this particular TADF system could be fur-

ther deciphered, leading to a deeper understanding of the broadening mechanisms of the triplet-sublevels.

Ultimately, this work demonstrates the inevitability of understanding spin-spin interactions in organic light-emitting diodes if their physically relevant processes are to be fully understood. While the new deep blue emitter has enabled further research expertise to be gained at the key weak point of display applications, namely the blue OLED emitters themselves, the spin-sensitive methods applied to the commercial emitters contributed to the fundamental understanding of OLED knowledge in general. Altogether, this information provides a small piece of the puzzle to the larger understanding of *how* the triplet-to-singlet up-conversion is accomplished in TADF based OLEDs and may be considered as a guideline to improve the next-generation OLED materials.

Zusammenfassung

Spin-Zustände bilden die entscheidende Grundlage für das Funktionsprinzip moderner organischer Leuchtdioden (OLEDs). Ihre direkte Untersuchung im elektrischen Betrieb war bisher eher ein weißer Fleck in der Literatur. In dieser Arbeit war es das Ziel, dazu beizutragen, diese Lücke zu schließen und die Beteiligung dieser Spin-Zustände an den fundamentalen Prozessen in organischen Halbleitern zu untersuchen. Die Vielfalt der in dieser Arbeit untersuchten Materialien resultiert aus dem neueren Ansatz, Moleküle zur Steigerung der OLED-Effizienz einzusetzen, deren optische Zustände thermisch aktiviert sind. Die sogenannte thermisch aktivierte verzögerte Fluoreszenz (TADF) ermöglicht eine energetische Aufwärtskonversion von dunklen Triplett-Zuständen zu leuchtenden Singulett-Zuständen. Die für diesen Mechanismus verantwortlichen Spin-Spin-Wechselwirkungen werden im Rahmen der Arbeit mit Methoden untersucht, die auf der spinsensitiven Elektron Paramagnetische Resonanz (EPR) basieren. Insbesondere wurde diese Methode schrittweise auf elektrisch betriebene OLEDs angewendet und die magnetische Resonanz durch Elektrolumineszenz nachgewiesen, was der Methode ihren Namen verleiht: Elektrolumineszenz detektierte magnetische Resonanz.
Der Einführung in die erste experimentelle Studie dieser Arbeit erfolgte mit der Untersuchung des neuartigen tiefblauen TADF-Emitter SBABz4, dessen Emissionseigenschaften stark von der geometrischen Anordnung seiner molekularen Einheiten abhängen. Das Molekül wurde von Mitarbeitern der École Polytechnique Fédérale de Lausanne (EPFL) in der Schweiz entworfen und synthetisiert. Die Besonderheit des Designs ist die stäbchenförmige Geometrie des Moleküls, die die Auskopplungseffizienz aus dem OLED-Bauelement maßgeblich beeinflusst. Die horizontale Orientierung des Emissionsübergangs-Dipolmoments wurde von Kooperationspartnern aus Augsburg zu 80 % bestimmt.
Die vorliegende Arbeit zeigte, dass der untersuchte Prozess der umgekehrten Interkombination (engl.: *reverse intersystem crossing, RISC*) stark vom Flächenwinkel θ des Emitters zwischen seiner Donor- und Akzeptoreinheit abhängt. Die Spin-Spin-Wechselwirkung, welche die Energielücke ΔE_{ST} zwischen Singulett und Triplett einstellt, hängt also stark von diesem Winkel ab. Theoretische Simulationen der Kollaborationspartner zeigten, dass eine perfekte Abstimmung zwischen maximalem Winkel ($\theta \sim 90°$) für effiziente Aufwärtskonversion und minimalem Winkel für effiziente Emissionseigenschaften ($\theta \sim 0°$), d. h. Oszillatorstärke f, notwendig ist. Die Energielücke zwischen Singulett und Triplett wurde durch transiente Elektrolumineszenz und transiente Photolumineszenz zu $\Delta E_{\mathrm{ST}} = 72 \pm 5\,\mathrm{meV}$ bestimmt. Die Aktivierungsenergie konnte mit einem mittleren Flächenwinkel von $\theta \approx 70 - 75°$ zwischen den Donor- und Akzeptor-

einheiten verknüpft werden, der entscheidend von $\theta = 86°$ für ein entspanntes Molekül im Vakuum abweicht. Die Arbeit unterstreicht die Bedeutung der Balance zwischen einer kleinen Energielücke für effiziente TADF und ausreichender Oszillatorstärke für zukünftige Designkonzepte kommender OLED-Generationen.
Um ein weitergehendes physikalisches Verständnis über kommerziell erhältliche TADF-Moleküle zu generieren, wurde in einer weiteren Studie die auf magnetischer Resonanz basierende Methode ELDMR angewendet. Die zugrunde liegende Physik der thermischen Aufwärtskonversion der Tripletts zu Singulett wirft in der Literatur noch offene Fragen auf. An dieser Stelle der Arbeit wurde die Magnetfeldabhängigkeit der Linienbreite der ELDMR-Spektren ausgewertet. Die daraus gewonnenen Informationen lassen Rückschlüsse auf die am RISC-Prozess beteiligten Mechanismen zu. Der Δg-Mechanismus konnte als ein Begleiter im RISC-Prozess identifiziert werden. Für die folgenden Materialkombinationen wurde ein Wert für die g-Faktor-Differenz Δg zwischen Elektron und Loch ermittelt: Während für m-MTDATA:BPHEN aufgrund des niedrigen $\Delta g = 5{,}3 \times 10^{-7}$ keine Verbreiterung beobachtet wurde, zeigen m-MTDATA:3T-PYMB ($\Delta g = 2{,}4 \times 10^{-3}$) und DMAC-DPS ($\Delta g = 1{,}5 \times 10^{-3}$) starke Hinweise auf Spin-Bahn-Kopplungseffekte, die zu RISC beitragen.
In einer letzten Studie wurde die ELDMR-Linienbreite des TADF-Materials m-MTDATA:BPHEN genauer untersucht, um dem Ursprung der Inhomogenität der ELDMR- Spektren mit einer Breite $\mathrm{FWHM_{Inhomo}} = 62\,\mathrm{MHz}$ auf den Grund zu gehen. Eine Methode, die sich für diesen Zweck besonders gut eignete, ist das Doppelresonanz-Experiment des spektralen Mikrowellen-Lochbrennens. Bei dieser besonderen EPR-Methode wurden einzelne EPR-Übergänge durch eine eingestrahlte Pump-Mikrowellenfrequenz gesättigt, die dann durch eine Sondenfrequenz nicht mehr an der eigentlichen magnetischen Resonanz teilnahmen. Die Sättigung dieser Zustände erzeugte ein spektrales Loch im ELDMR-Spektrum, aus dessen Form weitere Eigenschaften über das TADF-Material abgeleitet werden konnten. Das Innerste des Lochs wird durch die Spin-Relaxationszeiten des zugrunde liegenden Exciplex-Zustands begrenzt. Es wurde festgestellt, dass das Loch einerseits aus einer breiten homogenen Linie mit $\mathrm{FWHM_h} = 22\,\mathrm{MHz}$ und andererseits aus einem spektralen Peak mit einer sub-natürlichen Linienbreite von $\mathrm{FWHM_{relax}} = 12\,\mathrm{kHz}$ besteht. Letztere hat ihren Ursprung in Schwebungseffekten im OLED-Spin-System aufgrund eines oszillierenden Mikrowellenfeldes, welches durch Schwebung der beiden Mikrowellenfelder der Pump- und der Sondenfrequenz entsteht. Die homogene Linienbreite lieferte eine untere Grenze für eine transversale Dephasierungszeit $t_{\mathrm{deph}} > 30\,\mathrm{ns}$, während die Spike-Linienbreite auf eine obere Grenze der longitudinalen Relaxationszeit $t_{\mathrm{relax}} < 50\,\mu\mathrm{s}$ bezogen werden könnte.
Mithilfe des spektralen Mikrowellenlochbrennens konnten die Spin-Spin-Wechselwirk-

ungen in diesem speziellen TADF-System weiter entschlüsselt werden, was zu einem tieferen Verständnis der Verbreiterungsmechanismen der Triplett-Sublevels führte.

Letztendlich hebt diese Arbeit die Bedeutung von Spin-Spin-Wechselwirkungen in organischen Leuchtdioden hervor, wenn deren physikalisch relevante Prozesse vollständig verstanden werden sollen. Während mit dem neuen tiefblauen Emitter weiteres Wissen über die Achillesferse der Displayanwendungen gewonnen wurde, nämlich blauen OLED-Emitter selbst, trugen die auf kommerzielle Emitter angewendeten Spin-sensitiven Methoden zum grundlegenden Verständnis des allgemeinen OLED-Wissens bei. Diese Informationen liefern ein kleines Puzzlestück zum größeren Bild, wie die Triplett-zu-Singulett Aufwärtskonversion in TADF-basierten OLEDs erreicht wird. Sie können als Leitfaden zur Verbesserung der OLED-Materialien der nächsten Generation betrachtet werden.

Bibliography

[1] S. Hofmann, Josephine; Piele, Alexander; Piele, Christian;: Bauer, Wilhelm; Riedel, Oliver; Rief. Arbeiten in der Corona-Pandemie - Auf dem Weg zum New Normal. Technical report, Fraunhofer-Institut für Arbeitswirtschaft und Organisation -IAO-, Stuttgart; Deutsche Gesellschaft für Personalführung -DGFP-, Frankfurt am Main (2020).

[2] Research and Markets. Display Market with COVID-19 Impact Analysis by Product (Smartphones, Wearables, Television Sets, Signage, Tablets), Resolution, Display Technology (LCD, OLED, Direct-View LED, Micro-LED), Panel Size, Vertical, and Geography - Global Forecast to 2026. Technical report (2021).

[3] Displaysupplychain. OLED Smartphone Panel Revenues (2018). webpage: https://www.displaysupplychain.com/blog/oled-panel-revenues-to-grow-19-in-2019. date accessed: 2021-05-04.

[4] Omdia. Sales of OLED TVs worldwide from 2018 to 2019 and forecast to 2024 (2019). webpage: https://de.statista.com/statistik/daten/studie/246239/umfrage/prognose-zum-absatz-von-oled-fernsehgeraeten/. date accessed: 2021-05-04.

[5] Idc.com. Forecast for sales of wearables worldwide from 2014 to 2024 (2020). webpage: https://de.statista.com/statistik/daten/studie/417580/umfrage/prognose-zum-absatz-von-wearables/. date accessed: 2021-05-04.

[6] Arinsider. AR glasses global penetration (2021). webpage: https://www.statista.com/statistics/610496/smart-ar-glasses-shipments-worldwide/. date accessed: 2021-05-04.

[7] C. Lian, M. Piksa, K. Yoshida, S. Persheyev, K. J. Pawlik, K. Matczyszyn and I. D. Samuel. Flexible organic light-emitting diodes for antimicrobial photodynamic therapy. *npj Flexible Electronics*, **3**, 1 (2019). ISSN 23974621. doi: 10.1038/s41528-019-0058-0.

[8] J. Barsotti, A. G. Rapidis, I. Hirata, F. Greco, F. Cacialli and V. Mattoli. Ultra-thin, Ultra-Conformable, and Free-Standing Tattooable Organic Light-Emitting Diodes. *Advanced Electronic Materials*, **7**, 3, 1 (2021). ISSN 2199160X. doi: 10.1002/aelm.202001145.

[9] A. R. Brown, K. Pichler, N. C. Greenham, D. D. C. Bradley, R. H. Friend and A. B. Holmes. Optical spectroscopy of triplet excitons and charges excitations in PPV LEDs. *Chemical Physics Letters*, **210**, 1-3, 61 (1993).

[10] V. Cleave, G. Yahioglu, P. Le Barny, R. H. Friend and N. Tessler. Harvesting Singlet and Triplet Energy in Polymer LEDs. *Advanced Materials*, **11**, 4, 285 (1999). ISSN 0935-9648. doi: 10.1002/(SICI)1521-4095(199903)11:4<285::AID-ADMA285>3.0.CO;2-N.

[11] L. S. Swanson, J. Shinar, A. R. Brown, D. D. C. Bradley, R. H. Friend, P. L. Burn, A. Kraft and A. B. Holmes. Electroluminescence-detected magnetic-resonance study of polyparaphenylenevinylene (PPV)-based light-emitting diodes. *Physical Review B*, **46**, 23, 15072 (1992). ISSN 0163-1829. doi: 10.1103/PhysRevB.46.15072.

[12] C. Adachi, M. A. Baldo, M. E. Thompson and S. R. Forrest. Nearly 100light-emitting device. *Journal of Applied Physics*, **90**, 10, 5048 (2001). ISSN 0021-8979. doi: 10.1063/1.1409582.

[13] B. Minaev, E. Jansson, H. Ågren and S. Schrader. Very high-efficiency green organic light-emitting devices based on electrophosphorescence. *Natural transition orbitals The Journal of Chemical Physics*, **125**, 1, 164112 (2006). doi: 10.1063/1.2388263.

[14] J. C. Koziar and D. Cowan. Photochemical Heavy-Atom Effects1. **2499**, 10, 334 (1978).

[15] S. P. McGlynn, R. Sltnseri and N. Christodouleas. External heavy-atom spin-orbital coupling effect. I. The nature of the interaction. *The Journal of Chemical Physics*, **37**, 8, 1818 (1962). ISSN 00219606. doi: 10.1063/1.1733374.

[16] R. D. Costa, E. Ortí, H. J. Bolink, S. Graber, C. E. Housecroft and E. C. Constable. Light-emitting electrochemical cells based on a supramolecularly-caged phenanthroline-based iridium complex. *Chemical Communications*, **47**, 11, 3207 (2011). ISSN 13597345. doi: 10.1039/c0cc05084a.

[17] D. Cortés-Arriagada, L. Sanhueza, I. González, P. Dreyse and A. Toro-Labbé. About the electronic and photophysical properties of iridium(iii)-pyrazino[2,3-f][1,10]-phenanthroline based complexes for use in electroluminescent devices. *Physical Chemistry Chemical Physics*, **18**, 2, 726 (2015). ISSN 14639076. doi: 10.1039/c5cp05328e.

[18] S. Boudin. Phosphorescence des solutions glycériques d'éosine influence des iodures. *Journal de Chimie Physique*, **27**, 285 (1930). ISSN 0021-7689. doi: 10.1051/jcp/1930270285.

[19] G. N. Lewis and D. Lipkin. Reversible photochemical processes in rigid media. a study of the phosphorescent state. *Journal of the American Chemical Society* (1941). ISSN 15205126. doi: 10.1021/ja01856a043.

[20] C. A. Parker and C. G. Hatchard. Triplet-singlet emission in fluid solutions. Phosphorescence of eosin. *Transactions of the Faraday Society*, **57**, 1894 (1961). ISSN 0014-7672. doi: 10.1039/tf9615701894.

[21] J. Saltiel, H. C. Curtis, L. Metts, J. W. Miley, J. Winterle and M. Wrighton. Delayed Fluroescence and Phosphorescence of Aromatic Ketones in Solution. *Journal of the American Chemical Society*, **92**, 2, 410 (1970). ISSN 0002-7863. doi: 10.1021/ja00705a617.

[22] K. Goushi, K. Yoshida, K. Sato and C. Adachi. Organic light-emitting diodes employing efficient reverse intersystem crossing for triplet-to-singlet state conversion. *Nature Photonics*, **6**, 4, 253 (2012). ISSN 1749-4885. doi: 10.1038/nphoton.2012.31.

[23] H. Uoyama, K. Goushi, K. Shizu, H. Nomura and C. Adachi. Highly efficient organic light-emitting diodes from delayed fluorescence. *Nature*, **492**, 7428, 234 (2012). ISSN 00280836. doi: 10.1038/nature11687.

[24] Q. Zhang, B. Li, S. Huang, H. Nomura, H. Tanaka and C. Adachi. Efficient blue organic light-emitting diodes employing thermally activated delayed fluorescence. *Nature Photonics*, **8**, 4, 326 (2014). ISSN 1749-4885. doi: 10.1038/nphoton.2014.12.

[25] A. Endo, M. Ogasawara, A. Takahashi, D. Yokoyama, Y. Kato and C. Adachi. Thermally Activated Delayed Fluorescence from Sn4+-Porphyrin Complexes and Their Application to Organic Light Emitting Diodes - A Novel Mechanism for

Electroluminescence. *Advanced Materials*, **21**, 47, 4802 (2009). ISSN 09359648. doi: 10.1002/adma.200900983.

[26] C. M. Marian. Mechanism of the Triplet-to-Singlet Upconversion in the Assistant Dopant ACRXTN. *The Journal of Physical Chemistry C*, **120**, 7, 3715 (2016). ISSN 1932-7447. doi: 10.1021/acs.jpcc.6b00060.

[27] F. B. Dias, J. Santos, D. R. Graves, P. Data, R. S. Nobuyasu, M. A. Fox, A. S. Batsanov, T. Palmeira, M. N. Berberan-Santos, M. R. Bryce and A. P. Monkman. The Role of Local Triplet Excited States and D-A Relative Orientation in Thermally Activated Delayed Fluorescence: Photophysics and Devices. *Advanced Science*, **3**, 12, 1600080 (2016). ISSN 21983844. doi: 10.1002/advs.201600080.

[28] X. K. Chen, S. F. Zhang, J. X. Fan and A. M. Ren. Nature of highly efficient thermally activated delayed fluorescence in organic light-emitting diode emitters: Nonadiabatic effect between excited states. *Journal of Physical Chemistry C*, **119**, 18, 9728 (2015). ISSN 19327455. doi: 10.1021/acs.jpcc.5b00276.

[29] T. Ogiwara, Y. Wakikawa and T. Ikoma. Mechanism of Intersystem Crossing of Thermally Activated Delayed Fluorescence Molecules. *The Journal of Physical Chemistry A*, **119**, 14, 3415 (2015). ISSN 1089-5639. doi: 10.1021/acs.jpca.5b02253.

[30] J. E. Lennard-Jones. The electronic structure of some diatomic molecules. *Transactions of the Faraday Society*, **25**, 668 (1929). ISSN 0014-7672. doi: 10.1039/tf9292500668.

[31] A. Köhler and H. Bässler. *Electronic Processes in Organic Semiconductors*. Wiley-VCH Verlag GmbH Co. KGaA, Weinheim, Germany (2015). ISBN 9783527685172. doi: 10.1002/9783527685172.

[32] F. Hund. Zur Deutung verwickelter Spektren, insbesondere der Elemente Scandium bis Nickel. *Zeitschrift für Physik* (1925). ISSN 14346001. doi: 10.1007/BF01328319.

[33] F. L. Pilar. Molecular Quantum Mechanics, 2nd Edition (Atkins, P. W.). *Journal of Chemical Education* (1984). ISSN 0021-9584. doi: 10.1021/ed061pa248.2.

[34] W. Brütting, J. Frischeisen, T. D. Schmidt, B. J. Scholz and C. Mayr. Device efficiency of organic light-emitting diodes: Progress by improved light outcoupling. *physica status solidi (a)*, **210**, 1, 44 (2013). ISSN 18626300. doi: 10.1002/pssa.201228320.

[35] N. J. Turro, V. Ramamurthy and J. C. Scaiano. *Modern molecular photochemistry of organic molecules*. Wiley Online Library (2012).

[36] M. Kasha. Characterization of electronic transitions in complex molecules. *Discussions of the Faraday Society*, **9**, 14 (1950). ISSN 0366-9033. doi: 10.1039/df9500900014.

[37] E. U. Condon. Nuclear Motions Associated with Electron Transitions in Diatomic Molecules. *Physical Review*, **32**, 6, 858 (1928). ISSN 0031-899X. doi: 10.1103/PhysRev.32.858.

[38] E. Fermi. *Nuclear physics: a course given by Enrico Fermi at the University of Chicago*. University of Chicago Press (1950). ISBN 978-0226243658.

[39] H. Bässler. Charge Transport in Disordered Organic Photoconductors a Monte Carlo Simulation Study. *physica status solidi (b)*, **175**, 1, 15 (1993). ISSN 03701972. doi: 10.1002/pssb.2221750102.

[40] R. A. Marcus. On the Theory of Oxidation-Reduction Reactions Involving Electron Transfer. I. *The Journal of Chemical Physics*, **24**, 5, 966 (1956). ISSN 0021-9606. doi: 10.1063/1.1742723.

[41] A. Miller and E. Abrahams. Impurity conduction at low concentrations. *Physical Review*, **120**, 3, 745 (1960). ISSN 0031899X. doi: 10.1103/PhysRev.120.745.

[42] Y. N. Gartstein and E. M. Conwell. High-field hopping mobility in molecular systems with spatially correlated energetic disorder. *Chemical Physics Letters*, **245**, 4-5, 351 (1995). ISSN 00092614. doi: 10.1016/0009-2614(95)01031-4.

[43] S. V. Novikov, D. H. Dunlap, V. M. Kenkre, P. E. Parris and A. V. Vannikov. Essential Role of Correlations in Governing Charge Transport in Disordered Organic Materials. *Physical Review Letters*, **81**, 20, 4472 (1998). ISSN 10797114. doi: 10.1103/PhysRevLett.81.4472.

[44] W. F. Pasveer, J. Cottaar, C. Tanase, R. Coehoorn, P. A. Bobbert, P. W. Blom, M. De Leeuw and M. A. Michels. Unified description of charge-carrier mobilities in disordered semiconducting polymers. *Physical Review Letters*, **94**, 20, 1 (2005). ISSN 00319007. doi: 10.1103/PhysRevLett.94.206601.

[45] H. Ishii and K. Seki. Energy level alignment at organic/metal interfaces studied by UV photoemission: breakdown of traditional assumption of a common vacuum level at the interface. *IEEE Transactions on Electron Devices*, **44**, 8, 1295 (1997). ISSN 00189383. doi: 10.1109/16.605471.

[46] X. Crispin, V. Geskin, A. Crispin, J. Cornil, R. Lazzaroni, W. R. Salaneck and J. L. Brédas. Characterization of the interface dipole at organic/metal interfaces. *Journal of the American Chemical Society*, **124**, 27, 8131 (2002). ISSN 00027863. doi: 10.1021/ja025673r.

[47] J. G. Simmons. Richardson-Schottky Effect in Solids. *Physical Review Letters*, **15**, 25, 967 (1965). ISSN 0031-9007. doi: 10.1103/PhysRevLett.15.967.

[48] R. H. Fowler and L. Nordheim. Electron emission in intense electric fields. *Proceedings of the Royal Society of London. Series A, Containing Papers of a Mathematical and Physical Character*, **119**, 781, 173 (1928). ISSN 0950-1207. doi: 10.1098/rspa.1928.0091.

[49] M. Pope, H. P. Kallmann and P. Magnante. Electroluminescence in Organic Crystals. *The Journal of Chemical Physics*, **38**, 8, 2042 (1963). ISSN 0021-9606. doi: 10.1063/1.1733929.

[50] C. W. Tang and S. A. VanSlyke. Organic electroluminescent diodes. *Applied Physics Letters*, **51**, 12, 913 (1987). ISSN 0003-6951. doi: 10.1063/1.98799.

[51] W. Shockley. The Theory of p-n Junctions in Semiconductors and p-n Junction Transistors. *Bell System Technical Journal*, **28**, 3, 435 (1949). ISSN 00058580. doi: 10.1002/j.1538-7305.1949.tb03645.x.

[52] K. Tvingstedt and C. Deibel. Temperature Dependence of Ideality Factors in Organic Solar Cells and the Relation to Radiative Efficiency. *Advanced Energy Materials*, **6**, 9, 1502230 (2016). ISSN 16146832. doi: 10.1002/aenm.201502230.

[53] M. Pfeiffer, K. Leo, X. Zhou, J. S. Huang, M. Hofmann, A. Werner and J. Blochwitz-Nimoth. Doped organic semiconductors: Physics and application in light emitting diodes. *Organic Electronics* (2003). ISSN 15661199. doi: 10.1016/j.orgel.2003.08.004.

[54] N. C. Greenham, R. H. Friend and D. D. Bradley. Angular Dependence of the Emission from a Conjugated Polymer Light-Emitting Diode: Implications for efficiency calculations. *Advanced Materials* (1994). ISSN 15214095. doi: 10.1002/adma.19940060612.

[55] T. Tsutsui, E. Aminaka, C. P. Lin and D. U. Kim. Extended molecular design concept of molecular materials for electroluminescence: Sublimed-dye films, molecularly doped polymers and polymers with chromophores. *Philosophical*

Transactions of the Royal Society A: Mathematical, Physical and Engineering Sciences, **355**, 1725, 801 (1997). ISSN 1364503X. doi: 10.1098/rsta.1997.0045.

[56] S. Nowy, J. Frischeisen and W. Brütting. Simulation based optimization of light-outcoupling in organic light-emitting diodes. In *Organic Light Emitting Materials and Devices XIII* (2009). ISBN 9780819477057. ISSN 0277786X. doi: 10.1117/12.824858.

[57] J.-S. Kim, P. K. H. Ho, N. C. Greenham and R. H. Friend. Electroluminescence emission pattern of organic light-emitting diodes: Implications for device efficiency calculations. *Journal of Applied Physics*, **88**, 2, 1073 (2000). ISSN 0021-8979. doi: 10.1063/1.373779.

[58] T. D. Schmidt, D. S. Setz, M. Flämmich, J. Frischeisen, D. Michaelis, B. C. Krummacher, N. Danz and W. Brütting. Evidence for non-isotropic emitter orientation in a red phosphorescent organic light-emitting diode and its implications for determining the emitter's radiative quantum efficiency. *Applied Physics Letters*, **99**, 225 (2011). ISSN 00036951. doi: 10.1063/1.3653475.

[59] L. Xiao, Z. Chen, B. Qu, J. Luo, S. Kong, Q. Gong and J. Kido. Recent progresses on materials for electrophosphorescent organic light-emitting devices. *Advanced Materials*, **23**, 8, 926 (2011). ISSN 09359648. doi: 10.1002/adma.201003128.

[60] S. Reineke, F. Lindner, G. Schwartz, N. Seidler, K. Walzer, B. Lüssem and K. Leo. White organic light-emitting diodes with fluorescent tube efficiency. *Nature*, **459**, 7244, 234 (2009). ISSN 0028-0836. doi: 10.1038/nature08003.

[61] Z. B. Wang, M. G. Helander, J. Qiu, D. P. Puzzo, M. T. Greiner, Z. M. Hudson, S. Wang, Z. W. Liu and Z. H. Lu. Unlocking the full potential of organic light-emitting diodes on flexible plastic. *Nature Photonics*, **5**, 12, 753 (2011). ISSN 17494885. doi: 10.1038/nphoton.2011.259.

[62] Kenichi Goushi, Kou Yoshida, Keigo Sato and Chihaya Adachi. Organic light emitting diodes employing efficient reverse intersystem crossing for triplet to singlet state conversion. *Nature Photonics*, **6**, 253 (2012). doi: 10.1038/nphoton.2012.31 10.1038/NPHOTON.2012.31.

[63] Y. Wang, K. Sahin-Tiras, N. J. Harmon, M. Wohlgenannt and M. E. Flatté. Immense Magnetic Response of Exciplex Light Emission due to Correlated Spin-Charge Dynamics. *Physical Review X*, **6**, 1, 011011 (2016). ISSN 2160-3308. doi: 10.1103/PhysRevX.6.011011.

[64] Y. Tao, K. Yuan, T. Chen, P. Xu, H. Li, R. Chen, C. Zheng, L. Zhang and W. Huang. Thermally Activated Delayed Fluorescence Materials Towards the Breakthrough of Organoelectronics. *Advanced Materials*, **26**, 47, 7931 (2014). ISSN 09359648. doi: 10.1002/adma.201402532.

[65] H. Yersin. *Highly efficient OLEDs: Materials based on thermally activated delayed fluorescence*. Wiley (2018). ISBN 9783527691722. doi: 10.1002/9783527691722.

[66] A. Szabo and N. Ostlund. *Modern quantum chemistry : introduction to advanced electronic structure theory / Attila Szabo, Neil S. Ostlund* (1996). ISBN 9780486691862.

[67] T. Chen, L. Zheng, J. Yuan, Z. An, R. Chen, Y. Tao, H. Li, X. Xie and W. Huang. Understanding the Control of Singlet-Triplet Splitting for Organic Exciton Manipulating: A Combined Theoretical and Experimental Approach. *Scientific Reports*, **5**, 1, 10923 (2015). ISSN 2045-2322. doi: 10.1038/srep10923.

[68] S. Weissenseel, N. A. Drigo, L. G. Kudriashova, M. Schmid, T. Morgenstern, K. H. Lin, A. Prlj, C. Corminboeuf, A. Sperlich, W. Brütting, M. K. Nazeeruddin and V. Dyakonov. Getting the Right Twist: Influence of Donor-Acceptor Dihedral Angle on Exciton Kinetics and Singlet-Triplet Gap in Deep Blue Thermally Activated Delayed Fluorescence Emitter. *Journal of Physical Chemistry C*, **123**, 45, 27778 (2019). ISSN 19327455. doi: 10.1021/acs.jpcc.9b08269.

[69] X. K. Chen, Y. Tsuchiya, Y. Ishikawa, C. Zhong, C. Adachi and J. L. Brédas. A New Design Strategy for Efficient Thermally Activated Delayed Fluorescence Organic Emitters: From Twisted to Planar Structures. *Advanced Materials*, **29**, 1702767 (2017). ISSN 15214095. doi: 10.1002/adma.201702767.

[70] Q. Huang, S. Zhao, Z. Xu, X. Fan, C. Shen and Q. Yang. Exciplex emission and decay of co-deposited 4,4',4"-tris [3-methylphenyl (phenyl) amino] triphenylamine: tris-[3-(3-pyridyl) mesityl] borane organic light-emitting devices with different electron transporting layer thicknesses. *Applied Physics Letters*, **104**, 16, 161112 (2014).

[71] D. Graves, V. Jankus, F. B. Dias and A. Monkman. Photophysical Investigation of the Thermally Activated Delayed Emission from Films of m-MTDATA:PBD Exciplex. *Advanced Functional Materials*, **24**, 16, 2343 (2014). ISSN 1616301X. doi: 10.1002/adfm.201303389.

[72] T. Zhang, B. Chu, W. Li, Z. Su, Q. M. Peng, B. Zhao, Y. Luo, F. Jin, X. Yan, Y. Gao, H. Wu, F. Zhang, D. Fan and J. Wang. Efficient Triplet Application in Exciplex Delayed-Fluorescence OLEDs Using a Reverse Intersystem Crossing Mechanism Based on a $E_S of around Zero. ACS Applied Materials Interfaces$, **6**, 15, 11907(2014). $ISSN$1944–8244. doi : 10.1021/am501164s.

[73] J. A. Weil and J. R. Bolton. *Electron paramagnetic resonance: elementary theory and practical applications*. John Wiley Sons (2007). ISBN 9780471754961.

[74] D. Goldfarb and S. Stoll. *EPR Spectroscopy: Fundamentals and Methods*. John Wiley Sons, 1st editio edition (2018). ISBN 9781119162971.

[75] C. P. Poole. *Electron spin resonance: a comprehensive treatise on experimental techniques*. John Wiley Sons, Inc. (1983). ISBN 9780486694443.

[76] W. Gerlach and O. Stern. Der experimentelle Nachweis des magnetischen Moments des Silberatoms. *Zeitschrift für Physik*, **8**, 1, 110 (1922). ISSN 1434-6001. doi: 10.1007/BF01329580.

[77] A. Abragam and M. H. L. Pryce. Theory of the nuclear hyperfine structure of paramagnetic resonance spectra in crystals. *Proceedings of the Royal Society of London. Series A. Mathematical and Physical Sciences*, **205**, 1080, 135 (1951). ISSN 0080-4630. doi: 10.1098/rspa.1951.0022.

[78] S. Stoll and A. Schweiger. EasySpin, a comprehensive software package for spectral simulation and analysis in EPR. *Journal of Magnetic Resonance*, **178**, 1, 42 (2006). ISSN 10907807. doi: 10.1016/j.jmr.2005.08.013.

[79] W. Pauli. Exclusion Principle and Quantum Mechanics. In *Writings on Physics and Philosophy*, 165–181. Springer Berlin Heidelberg, Berlin, Heidelberg (1994). doi: 10.1007/978-3-662-02994-$7_2$0.

[80] A. Bencini and D. Gatteschi. *Electron Paramagnetic Resonance of Exchange Coupled Systems*. Springer Berlin Heidelberg, Berlin, Heidelberg (1990). ISBN 978-3-642-74601-7. doi: 10.1007/978-3-642-74599-7.

[81] P. Zeeman. The effect of magnetisation on the nature of light emitted by a substance. *Nature* (1897). ISSN 00280836. doi: 10.1038/055347a0.

[82] M. Pope and C. E. Swenberg. *Electronic Processes in Organic Crystals and Polymers*. Electronic Processes in Organic Crystals and Polymers (1999). ISBN 0195129636. doi: 10.1063/1.327880.

[83] U. E. Steiner and T. Ulrich. Magnetic field effects in chemical kinetics and related phenomena. *Chemical Reviews*, **89**, 1, 51 (1989). ISSN 0009-2665. doi: 10.1021/cr00091a003.

[84] G. Jeschke. Determination of the nanostructure of polymer materials by electron paramagnetic resonance spectroscopy. *Macromolecular Rapid Communications*, **23**, 4, 227 (2002). ISSN 10221336. doi: 10.1002/1521-3927(20020301)23:4<227::AID-MARC227>3.0.CO;2-D.

[85] E. Fermi. Über die magnetischen Momente der Atomkerne. *Zeitschrift für Physik*, **60**, 5-6, 320 (1930). ISSN 1434-6001. doi: 10.1007/BF01339933.

[86] M. Brustolon and E. Giamello. *Electron Paramagnetic Resonance*. John Wiley Sons, Inc., Hoboken, NJ, USA (2009). ISBN 9780470432235. doi: 10.1002/9780470432235.

[87] A. Farmany. Lifetime broadening of a nuclear magnetic resonance peak under minimal length uncertainty analysis. *Acta Physica Polonica A*, **117**, 3, 454 (2010). ISSN 1898794X. doi: 10.12693/APhysPolA.117.454.

[88] D. Sen. The uncertainty relations in quantum mechanics. *Current Science*, **107**, 2, 203 (2014). ISSN 00113891. doi: 10.18520/CS/V107/I2/203-218.

[89] G. R. Eaton, S. S. Eaton, D. P. Barr and R. T. Weber. *Quantitative EPR*. Springer Vienna, Vienna (2010). ISBN 978-3-211-92947-6. doi: 10.1007/978-3-211-92948-3.

[90] J. F. Wang, J. M. Cui, F. F. Yan, Q. Li, Z. D. Cheng, Z. H. Liu, Z. H. Lin, J. S. Xu, C. F. Li and G. C. Guo. Optimization of power broadening in optically detected magnetic resonance of defect spins in silicon carbide. *Physical Review B*, **101**, 6, 4 (2020). ISSN 24699969. doi: 10.1103/PhysRevB.101.064102.

[91] R. F. Wenzel and Y. W. Kim. Linewidth of the Electron Paramagnetic Resonance. *Physical Review*, **140**, 5A, A1592 (1965). ISSN 0031-899X. doi: 10.1103/PhysRev.140.A1592.

[92] W. Froncisz and J. S. Hyde. Broadening by strains of lines in the g-parallel region of Cu2+ EPR spectra. *The Journal of Chemical Physics*, **73**, 7, 3123 (1980). ISSN 00219606. doi: 10.1063/1.440548.

[93] W. R. Hagen, D. O. Hearshen, R. H. Sands and W. R. Dunham. A statistical theory for powder EPR in distributed systems. *Journal of Magnetic Resonance (1969)*, **61**, 2, 220 (1985). ISSN 00222364. doi: 10.1016/0022-2364(85)90077-0.

[94] G. Jeschke. Einführung in die ESR-Spektroskopie - Skript Mainz (1998).

[95] W. Demtröder. *Laserspektroskopie 1*. Springer Berlin Heidelberg, Berlin, Heidelberg (2011). ISBN 978-3-642-21305-2. doi: 10.1007/978-3-642-21306-9.

[96] N. Bunzmann. Excited State Pathways in 3rd Generation Organic Light-Emitting Diodes. Ph.d. thesis, Excited State Pathways in 3rd Generation Organic Light-Emitting Diodes (2020).

[97] M. Y. Wong and E. Zysman-Colman. Purely Organic Thermally Activated Delayed Fluorescence Materials for Organic Light-Emitting Diodes. *Advanced Materials*, **29**, 22, 1605444 (2017). ISSN 09359648. doi: 10.1002/adma.201605444.

[98] Z. Yang, Z. Mao, Z. Xie, Y. Zhang, S. Liu, J. Zhao, J. Xu, Z. Chi and M. P. Aldred. Recent advances in organic thermally activated delayed fluorescence materials. *Chemical Society Reviews*, **46**, 3, 915 (2017). ISSN 0306-0012. doi: 10.1039/C6CS00368K.

[99] Y. Im, M. Kim, Y. J. Cho, J.-A. Seo, K. S. Yook and J. Y. Lee. Molecular Design Strategy of Organic Thermally Activated Delayed Fluorescence Emitters. *Chemistry of Materials*, **29**, 5, 1946 (2017). ISSN 0897-4756. doi: 10.1021/acs.chemmater.6b05324.

[100] Y. Liu, C. Li, Z. Ren, S. Yan and M. R. Bryce. All-organic thermally activated delayed fluorescence materials for organic light-emitting diodes. *Nature Reviews Materials*, **3**, 4, 18020 (2018). ISSN 20588437. doi: 10.1038/natrevmats.2018.20.

[101] X. Cai and S. Su. Marching Toward Highly Efficient, Pure-Blue, and Stable Thermally Activated Delayed Fluorescent Organic Light-Emitting Diodes. *Advanced Functional Materials*, **28**, 43, 1802558 (2018). ISSN 1616301X. doi: 10.1002/adfm.201802558.

[102] D. R. Lee, B. S. Kim, C. W. Lee, Y. Im, K. S. Yook, S.-H. Hwang and J. Y. Lee. Above 30Organic Light-Emitting Diodes. *ACS Applied Materials Interfaces*, **7**, 18, 9625 (2015). ISSN 1944-8244. doi: 10.1021/acsami.5b01220.

[103] D. Yokoyama, A. Sakaguchi, M. Suzuki and C. Adachi. Horizontal orientation of linear-shaped organic molecules having bulky substituents in neat and doped vacuum-deposited amorphous films. *Organic Electronics: physics, materials, applications*, **10**, 1, 127 (2009). ISSN 15661199. doi: 10.1016/j.orgel.2008.10.010.

[104] T. D. Schmidt, T. Lampe, M. R. Daniel Sylvinson, P. I. Djurovich, M. E. Thompson and W. Brütting. Emitter Orientation as a Key Parameter in Organic Light-Emitting Diodes. *Physical Review Applied*, **8**, 3, 37001 (2017). ISSN 23317019. doi: 10.1103/PhysRevApplied.8.037001.

[105] T.-A. Lin, T. Chatterjee, W.-L. Tsai, W.-K. Lee, M.-J. Wu, M. Jiao, K.-C. Pan, C.-L. Yi, C.-L. Chung, K.-T. Wong, C.-C. Wu and Others. Organic LEDs: Sky-Blue Organic Light Emitting Diode with 37External Quantum Efficiency Using Thermally Activated Delayed Fluorescence from Spiroacridine-Triazine Hybrid (Adv. Mater. 32/2016). *Advanced Materials*, **28**, 32, 7029 (2016). doi: 10.1002/adma.201670224.

[106] M. Liu, R. Komatsu, X. Cai, K. Hotta, S. Sato, K. Liu, D. Chen, Y. Kato, H. Sasabe, S. Ohisa, Y. Suzuri, D. Yokoyama, S. J. Su and J. Kido. Horizontally Orientated Sticklike Emitters: Enhancement of Intrinsic Out-Coupling Factor and Electroluminescence Performance. *Chemistry of Materials*, **29**, 20, 8630 (2017). ISSN 15205002. doi: 10.1021/acs.chemmater.7b02403.

[107] M. Numata, T. Yasuda and C. Adachi. High efficiency pure blue thermally activated delayed fluorescence molecules having 10H-phenoxaborin and acridan units. *Chemical Communications*, **51**, 46, 9443 (2015). ISSN 1359-7345. doi: 10.1039/C5CC00307E.

[108] K. Wang, C. J. Zheng, W. Liu, K. Liang, Y. Z. Shi, S. L. Tao, C. S. Lee, X. M. Ou and X. H. Zhang. Avoiding Energy Loss on TADF Emitters: Controlling the Dual Conformations of D–A Structure Molecules Based on the Pseudoplanar Segments. *Advanced Materials*, **29**, 47, 1701476 (2017). ISSN 15214095. doi: 10.1002/adma.201701476.

[109] J. Frischeisen, D. Yokoyama, C. Adachi, W. Brütting, J. Frischeisen, D. Yokoyama, C. Adachi and W. Brütting. Determination of molecular dipole orientation in doped fluorescent organic thin films by photoluminescence measurements Determination of molecular dipole orientation in doped fluorescent organic thin films by photoluminescence measurements. *Applied Physics Letters*, **073302**, 2010, 11 (2011). doi: 10.1063/1.3309705.

[110] W. L. Barnes. Fluorescence near interfaces: The role of photonic mode density. *Journal of Modern Optics*, **45**, 4, 661 (1998). ISSN 0950-0340. doi: 10.1080/09500349808230614.

[111] L. Penninck, P. De Visschere, J. Beeckman and K. Neyts. Dipole radiation within one-dimensional anisotropic microcavities: a simulation method. *Optics Express*, **19**, 19, 18558 (2011). doi: 10.1364/oe.19.018558.

[112] D. Y. K. Ko and J. C. Inkson. Matrix method for tunneling in heterostructures: Resonant tunneling in multilayer systems. *Physical Review B*, **38**, 14, 9945 (1988). ISSN 01631829. doi: 10.1103/PhysRevB.38.9945.

[113] L.-s. Cui, H. Nomura, Y. Geng, J. U. Kim, H. Nakanotani and C. Adachi. Organic Electronics Hot Paper Controlling Singlet – Triplet Energy Splitting for Deep-Blue Thermally Activated Delayed Fluorescence Emitters Angewandte. *Angew. Chem. Int. Ed.*, **56**, 6, 1571 (2017). doi: 10.1002/anie.201609459.

[114] J. Zhang, D. Ding, Y. Wei and H. Xu. Extremely condensing triplet states of DPEPO-type hosts through constitutional isomerization for high-efficiency deep-blue thermally activated delayed fluorescence diodes. *Chemical Science*, **7**, 4, 2870 (2016). ISSN 2041-6520. doi: 10.1039/C5SC04848F.

[115] N. Drigo, L. Kudriashova, S. Weissenseel, A. Sperlich, A. Huckaba, M. Nazeeruddin and V. Dyakonov. Photophysics of Deep Blue Acridane- and Benzonitrile-Based Emitter Employing Thermally Activated Delayed Fluorescence. *Journal of Physical Chemistry C*, **122**, 39, 2279622801 (2018). ISSN 19327455. doi: 10.1021/acs.jpcc.8b08716.

[116] L. Muccioli, G. D'Avino and C. Zannoni. Simulation of vapor-phase deposition and growth of a pentacene thin film on C 60 (001). *Advanced Materials* (2011). ISSN 09359648. doi: 10.1002/adma.201101652.

[117] C. Tonnelé, M. Stroet, B. Caron, A. J. Clulow, R. C. Nagiri, A. K. Malde, P. L. Burn, I. R. Gentle, A. E. Mark and B. J. Powell. Elucidating the Spatial Arrangement of Emitter Molecules in Organic Light-Emitting Diode Films. *Angewandte Chemie - International Edition* (2017). ISSN 15213773. doi: 10.1002/anie.201610727.

[118] P. J. Stephens, F. J. Devlin, C. F. Chabalowski and M. J. Frisch. Ab Initio calculation of vibrational absorption and circular dichroism spectra using density functional force fields. *Journal of Physical Chemistry®*, **98**, 11623 (1994). ISSN 00223654. doi: 10.1021/j100096a001.

[119] A. D. Becke. Density-functional thermochemistry. III. The role of exact exchange. *The Journal of Chemical Physics*, **98**, 5648 (1993). ISSN 00219606. doi: 10.1063/1.464913.

[120] S. Grimme, S. Ehrlich and L. Goerigk. Effect of the damping function in dispersion corrected density functional theory. *Journal of Computational Chemistry*, **32**, 1465 (2011). ISSN 01928651. doi: 10.1002/jcc.21759.

[121] T. Stein, L. Kronik and R. Baer. Reliable prediction of charge transfer excitations in molecular complexesusing time-dependent density functional theory. *Journal of the American Chemical Society*, **131**, 2818 (2009). ISSN 00027863. doi: 10.1021/ja8087482.

[122] S. K. Lower and M. A. El-Sayed. The Triplet State and Molecular Electronic Processes in Organic Molecules. *Chemical Reviews*, **66**, 2, 199 (1966). ISSN 0009-2665. doi: 10.1021/cr60240a004.

[123] I. Lyskov and C. M. Marian. Climbing up the Ladder: Intermediate Triplet States Promote the Reverse Intersystem Crossing in the Efficient TADF Emitter ACRSA. *The Journal of Physical Chemistry C*, **121**, 39, 21145 (2017). ISSN 1932-7447. doi: 10.1021/acs.jpcc.7b06187.

[124] E. W. Evans, Y. Olivier, Y. Puttisong, W. K. Myers, T. J. H. Hele, S. M. Menke, T. H. Thomas, D. Credgington, D. Beljonne, R. H. Friend and N. C. Greenham. Vibrationally Assisted Intersystem Crossing in Benchmark Thermally Activated Delayed Fluorescence Molecules. *The Journal of Physical Chemistry Letters*, **9**, 14, 4053 (2018). ISSN 1948-7185. doi: 10.1021/acs.jpclett.8b01556.

[125] M. K. Etherington, J. Gibson, H. F. Higginbotham, T. J. Penfold and A. P. Monkman. Revealing the spin–vibronic coupling mechanism of thermally activated delayed fluorescence. *Nature Communications*, **7**, 1, 13680 (2016). ISSN 2041-1723. doi: 10.1038/ncomms13680.

[126] T. Zhang, B. Zhao, B. Chu, W. Li, Z. Su, L. Wang, J. Wang, F. Jin, X. Yan, Y. Gao, H. Wu, C. Liu, T. Lin and F. Hou. Blue exciplex emission and its role as a host of phosphorescent emitter. *Organic Electronics*, **24**, 1 (2015). ISSN 15661199. doi: 10.1016/j.orgel.2015.05.013.

[127] Q. Zhang, D. Tsang, H. Kuwabara, Y. Hatae, B. Li, T. Takahashi, S. Y. Lee, T. Yasuda and C. Adachi. Nearly 100Electroluminescent Devices Employing Pure Organic Emitters. *Advanced Materials*, **27**, 12, 2096 (2015). ISSN 09359648. doi: 10.1002/adma.201405474.

[128] J. Shinar. Optically detected magnetic resonance studies of luminescence-quenching processes in π-conjugated materials and organic light-emitting de-

vices. *Laser Photonics Reviews*, **6**, 6, 767 (2012). ISSN 18638880. doi: 10.1002/lpor.201100026.

[129] S. Väth, K. Tvingstedt, M. Auth, A. Sperlich, A. Dabuliene, J. V. Grazulevicius, P. Stakhira, V. Cherpak and V. Dyakonov. Direct Observation of Spin States Involved in Organic Electroluminescence Based on Thermally Activated Delayed Fluorescence. *Advanced Optical Materials*, **5**, 3, 1600926 (2017). ISSN 21951071. doi: 10.1002/adom.201600926.

[130] N. Bunzmann, S. Weissenseel, L. Kudriashova, J. Gruene, B. Krugmann, J. V. Grazulevicius, A. Sperlich and V. Dyakonov. Optically and electrically excited intermediate electronic states in donor:acceptor based OLEDs. *Materials Horizons*, **7**, 4, 1126 (2020). ISSN 2051-6347. doi: 10.1039/C9MH01475F.

[131] N. Bunzmann, B. Krugmann, S. Weissenseel, L. Kudriashova, K. Ivaniuk, P. Stakhira, V. Cherpak, M. Chapran, G. Grybauskaite-Kaminskiene, J. V. Grazulevicius, V. Dyakonov and A. Sperlich. Spin- and Voltage-Dependent Emission from Intra- and Intermolecular TADF OLEDs. *Advanced Electronic Materials*, **7**, 3, 1 (2021). ISSN 2199160X. doi: 10.1002/aelm.202000702.

[132] S. K. Misra. *Multifrequency Electron Paramagnetic Resonance*. Wiley-VCH Verlag GmbH Co. KGaA, Weinheim, Germany (2011). ISBN 9783527633531. doi: 10.1002/9783527633531.

[133] G. Joshi, R. Miller, L. Ogden, M. Kavand, S. Jamali, K. Ambal, S. Venkatesh, D. Schurig, H. Malissa, J. M. Lupton and C. Boehme. Separating hyperfine from spin-orbit interactions in organic semiconductors by multi-octave magnetic resonance using coplanar waveguide microresonators. *Applied Physics Letters*, **109**, 10, 103303 (2016). ISSN 0003-6951. doi: 10.1063/1.4960158.

[134] Z. Yang, Z. Mao, Z. Xie, Y. Zhang, S. Liu, J. Zhao, J. Xu, Z. Chi and M. P. Aldred. Recent advances in organic thermally activated delayed fluorescence materials. *Chemical Society Reviews*, **46**, 3, 915 (2017). ISSN 14604744. doi: 10.1039/c6cs00368k.

[135] M. K. Etherington, N. A. Kukhta, H. F. Higginbotham, A. Danos, A. N. Bismillah, D. R. Graves, P. R. McGonigal, N. Haase, A. Morherr, A. S. Batsanov, C. Pflumm, V. Bhalla, M. R. Bryce and A. P. Monkman. Persistent Dimer Emission in Thermally Activated Delayed Fluorescence Materials. *Journal of Physical Chemistry C*, **123**, 17, 11109 (2019). ISSN 19327455. doi: 10.1021/acs.jpcc.9b01458.

[136] Z. V. Vardeny. *Organic Spintronics*. CRC Press (2010). ISBN 9780429150722. doi: 10.1201/EBK1439806562.

[137] W. R. Bennett. Hole Burning Effects in a He-Ne Optical Maser. *Physical Review*, **126**, 2, 580 (1962). ISSN 0031-899X. doi: 10.1103/PhysRev.126.580.

[138] H. A. El-Ella, A. Huck and U. L. Andersen. Continuous microwave hole burning and population oscillations in a diamond spin ensemble. *Physical Review B*, **100**, 21, 214407 (2019). ISSN 24699969. doi: 10.1103/PhysRevB.100.214407.

[139] P. Kehayias, M. Mrózek, V. M. Acosta, A. Jarmola, D. S. Rudnicki, R. Folman, W. Gawlik and D. Budker. Microwave saturation spectroscopy of nitrogen-vacancy ensembles in diamond. *Physical Review B - Condensed Matter and Materials Physics*, **89**, 24, 1 (2014). ISSN 1550235X. doi: 10.1103/PhysRevB.89.245202.

[140] M. Leung and M. El-Sayed. Hole burning in the optically detected zero-field spectrum using eedor. *Chemical Physics Letters*, **16**, 3, 454 (1972). ISSN 00092614. doi: 10.1016/0009-2614(72)80399-3.

[141] W. E. Moerner, editor. *Persistent Spectral Hole-Burning: Science and Applications*, volume 44 of *Topics in Current Physics*. Springer Berlin Heidelberg, Berlin, Heidelberg (1988). ISBN 978-3-642-83292-5. doi: 10.1007/978-3-642-83290-1.

[142] P. R. Moran. Electron Spin Double Resonance Studies of F- Centers in KCl. I. *Physical Review*, **135**, 1A, A247 (1964). ISSN 0031-899X. doi: 10.1103/PhysRev.135.A247.

[143] M. Mrózek, D. Rudnicki, P. Kehayias, A. Jarmola, D. Budker and W. Gawlik. Longitudinal spin relaxation in nitrogen-vacancy ensembles in diamond. *EPJ Quantum Technology*, **2**, 1, 22 (2015). ISSN 2196-0763. doi: 10.1140/epjqt/s40507-015-0035-z.

[144] M. Mrozek, A. M. Wojciechowski, D. S. Rudnicki, J. Zachorowski, P. Kehayias, D. Budker and W. Gawlik. Coherent population oscillations with nitrogen-vacancy color centers in diamond. *Physical Review B*, **94**, 3, 1 (2016). ISSN 24699969. doi: 10.1103/PhysRevB.94.035204.

[145] K. W. Rousslang, J. B. Alexander Ross, A. L. Kwiram and D. A. Deranleau. Triplet State of Tryptophan in Proteins: The Nature of the Optically Detected Magnetic Resonance Lines. *Biochemistry*, **17**, 6, 1087 (1978). ISSN 15204995. doi: 10.1021/bi00599a023.

[146] J. U. von Schütz, J. Zuclich and A. H. Maki. Resolution of Tryptophan Phosphorescence from Multiple Sites in Proteins using Optical Detection of Magnetic Resonance. *Journal of the American Chemical Society*, **96**, 3, 714 (1974). ISSN 15205126. doi: 10.1021/ja00810a014.

[147] V. A. Soltamov, C. Kasper, A. V. Poshakinskiy, A. N. Anisimov, E. N. Mokhov, A. Sperlich, S. A. Tarasenko, P. G. Baranov, G. V. Astakhov and V. Dyakonov. Excitation and coherent control of spin qudit modes in silicon carbide at room temperature. *Nature Communications* (2019). ISSN 20411723. doi: 10.1038/s41467-019-09429-x.

[148] A. Gottscholl, M. Diez, V. Soltamov, C. Kasper, A. Sperlich, M. Kianinia, C. Bradac, I. Aharonovich and V. Dyakonov. Room temperature coherent control of spin defects in hexagonal boron nitride. *Science Advances*, **7**, 14, eabf3630 (2021). ISSN 2375-2548. doi: 10.1126/sciadv.abf3630.

[149] W. Y. Hung, G. C. Fang, Y. C. Chang, T. Y. Kuo, P. T. Chou, S. W. Lin and K. T. Wong. Highly efficient bilayer interface exciplex for yellow organic light-emitting diode. *ACS Applied Materials and Interfaces*, **5**, 15, 6826 (2013). ISSN 19448244. doi: 10.1021/am402032z.

[150] J. Li, H. Nomura, H. Miyazaki and C. Adachi. Highly efficient exciplex organic light-emitting diodes incorporating a heptazine derivative as an electron acceptor. *Chemical Communications*, **50**, 46, 6174 (2014). ISSN 1364548X. doi: 10.1039/c4cc01590h.

[151] M. Mamada, G. Tian, H. Nakanotani, J. Su and C. Adachi. The Importance of Excited-State Energy Alignment for Efficient Exciplex Systems Based on a Study of Phenylpyridinato Boron Derivatives. *Angewandte Chemie International Edition*, **57**, 38, 12380 (2018). ISSN 14337851. doi: 10.1002/anie.201804218.

[152] A. M. Akulshin, R. Mclean, A. I. Sidorov and P. Hannaford. *ELECTROMAGNETICALLY INDUCED ABSORPTION AND TRANSPARENCY DUE TO LONG-LIVED ZEEMAN COHERENCE*. January (2009). ISBN 978-1607410256.

[153] J. Fuchs, G. J. Duffy, W. J. Rowlands, A. Lezama, P. Hannaford and A. M. Akulshin. Electromagnetically induced transparency and absorption due to optical and ground-state coherences in 6Li. *Journal of Physics B: Atomic, Molecular and Optical Physics*, **40**, 6, 1117 (2007). ISSN 09534075. doi: 10.1088/0953-4075/40/6/003.

[154] J. H. Lee, J. J. Song, M. A. F. Scarparo and M. D. Levenson. Coherent population oscillations and hole burning observed in $Sm^{+}2$: $CaF_2 using polarization spectroscopy$. *Optics Letters*(1980). $ISSN$0146 − 9592.doi : 10.1364/ol.5.000196.

[155] N. Bunzmann, D. L. Baird, H. Malissa, S. Weissenseel, C. Boehme, V. Dyakonov and A. Sperlich. Thermal Activation Bottleneck in TADF OLEDs based on m-MTDATA:BPhen. *arXiv*, 1–15 (2020). ISSN 23318422.

[156] X. Liu, H. Popli, O. Kwon, H. Malissa, X. Pan, B. Park, B. Choi, S. Kim, E. Ehrenfreund, C. Boehme and Z. V. Vardeny. Isotope Effect in the Magneto-Optoelectronic Response of Organic Light-Emitting Diodes Based on Donor–Acceptor Exciplexes. *Advanced Materials*, **32**, 48, 2004421 (2020). ISSN 15214095. doi: 10.1002/adma.202004421.

[157] S. Richert, C. E. Tait and C. R. Timmel. Delocalisation of photoexcited triplet states probed by transient EPR and hyperfine spectroscopy. *Journal of Magnetic Resonance*, **280**, 103 (2017). ISSN 10960856. doi: 10.1016/j.jmr.2017.01.005.

[158] F. Kraffert and J. Behrends. Spin-correlated doublet pairs as intermediate states in charge separation processes. *Molecular Physics*, **115**, 19, 2373 (2017). ISSN 13623028. doi: 10.1080/00268976.2016.1278479.

[159] V. Ivády, G. Barcza, G. Thiering, S. Li, H. Hamdi, J. P. Chou, Ö. Legeza and A. Gali. Ab initio theory of the negatively charged boron vacancy qubit in hexagonal boron nitride. *npj Computational Materials*, **6**, 1, 1 (2020). ISSN 20573960. doi: 10.1038/s41524-020-0305-x.

[160] J. Niklas, K. L. Mardis, B. P. Banks, G. M. Grooms, A. Sperlich, V. Dyakonov, S. Beaupré, M. Leclerc, T. Xu, L. Yu and O. G. Poluektov. Highly-efficient charge separation and polaron delocalization in polymer-fullerene bulk-heterojunctions: A comparative multi-frequency EPR and DFT study. *Physical Chemistry Chemical Physics*, **15**, 24, 9562 (2013). ISSN 14639076. doi: 10.1039/c3cp51477c.

[161] R. Steyrleuthner, Y. Zhang, L. Zhang, F. Kraffert, B. P. Cherniawski, R. Bittl, A. L. Briseno, J. L. Bredas and J. Behrends. Impact of morphology on polaron delocalization in a semicrystalline conjugated polymer. *Physical Chemistry Chemical Physics*, **19**, 5, 3627 (2017). ISSN 14639076. doi: 10.1039/c6cp07485e.

[162] I. I. Vlasov, A. S. Barnard, V. G. Ralchenko, O. I. Lebedev, M. V. Kanzyuba, A. V. Saveliev, V. I. Konov and E. Goovaerts. Nanodiamond Photoemitters Based on Strong Narrow-Band Luminescence from Silicon-Vacancy Defects. *Advanced Materials*, **21**, 7, 808 (2009). ISSN 09359648. doi: 10.1002/adma.200802160.

[163] M. L. Kirk, D. A. Shultz, D. Habel-Rodriguez, R. D. Schmidt and U. Sullivan. Hyperfine interaction, spin polarization, and spin derealization as probes of donor-bridge-acceptor interactions in exchange-coupled biradicals. *Journal of Physical Chemistry B*, **114**, 45, 14712 (2010). ISSN 15205207. doi: 10.1021/jp102955j.

[164] T. A. Schaub, T. Mekelburg, P. O. Dral, M. Miehlich, F. Hampel, K. Meyer and M. Kivala. A Spherically Shielded Triphenylamine and Its Persistent Radical Cation. *Chemistry - A European Journal*, **26**, 15, 3264 (2020). ISSN 15213765. doi: 10.1002/chem.202000355.

[165] M. Kuratsu, M. Kozaki and K. Okada. 2,2:6,2:6,6-Trioxytriphenylamine: Synthesis and Properties of the Radical Cation and Neutral Species. *Angewandte Chemie*, **117**, 26, 4124 (2005). ISSN 0044-8249. doi: 10.1002/ange.200500397.

[166] W. J. Baker, T. L. Keevers, J. M. Lupton, D. R. McCamey and C. Boehme. Slow Hopping and Spin Dephasing of Coulombically Bound Polaron Pairs in an Organic Semiconductor at Room Temperature. *Physical Review Letters*, **108**, 26, 267601 (2012). ISSN 0031-9007. doi: 10.1103/PhysRevLett.108.267601.

[167] C. G. Yang, E. Ehrenfreund and Z. V. Vardeny. Polaron Spin-Lattice Relaxation Time in <math display="inline"> <mi>π</mi> </math> -Conjugated Polymers from Optically Detected Magnetic Resonance. *Physical Review Letters*, **99**, 15, 157401 (2007). ISSN 0031-9007. doi: 10.1103/PhysRevLett.99.157401.

[168] D. R. McCamey, H. A. Seipel, S.-Y. Paik, M. J. Walter, N. J. Borys, J. M. Lupton and C. Boehme. Spin Rabi flopping in the photocurrent of a polymer light-emitting diode. *Nature Materials*, **7**, 9, 723 (2008). ISSN 1476-1122. doi: 10.1038/nmat2252.

[169] F. Kraffert, R. Steyrleuthner, C. Meier, R. Bittl and J. Behrends. Transient electrically detected magnetic resonance spectroscopy applied to organic solar cells. *Applied Physics Letters*, **107**, 4, 043302 (2015). ISSN 0003-6951. doi: 10.1063/1.4927446.

[170] E. Hontz, W. Chang, D. N. Congreve, V. Bulovic, M. A. Baldo and T. Van Voorhis. The Role of Electron–Hole Separation in Thermally Activated Delayed Fluores-

cence in Donor–Acceptor Blends. *The Journal of Physical Chemistry C*, **119**, 45, 25591 (2015). doi: 10.1021/acs.jpcc.5b07340.

[171] J. Grüne, N. Bunzmann, M. Meinecke, V. Dyakonov and A. Sperlich. Kinetic Modeling of Transient Electroluminescence Reveals TTA as an Efficiency-Limiting Process in Exciplex-Based TADF OLEDs. *The Journal of Physical Chemistry C*, **124**, 47, 25667 (2020). ISSN 1932-7447. doi: 10.1021/acs.jpcc.0c06528.

[172] T. Huang, X. Song, M. Cai, D. Zhang and L. Duan. Improving reverse intersystem crossing in exciplex-forming hosts by introducing heavy atom effect. *Materials Today Energy*, **21**, 100705 (2021). ISSN 24686069. doi: 10.1016/j.mtener.2021.100705.

[173] Y.-S. Park, K.-H. Kim and J.-J. Kim. Efficient triplet harvesting by fluorescent molecules through exciplexes for high efficiency organic light-emitting diodes. *Applied Physics Letters*, **102**, 15, 153306 (2013). ISSN 0003-6951. doi: 10.1063/1.4802716.

[174] W.-C. Chen, C.-S. Lee and Q.-X. Tong. Blue-emitting organic electrofluorescence materials: progress and prospective. *Journal of Materials Chemistry C*, **3**, 42, 10957 (2015). ISSN 2050-7526. doi: 10.1039/C5TC02420J.

[175] Y. Olivier, B. Yurash, L. Muccioli, G. D'Avino, O. Mikhnenko, J. C. Sancho-García, C. Adachi, T.-Q. Nguyen and D. Beljonne. Nature of the singlet and triplet excitations mediating thermally activated delayed fluorescence. *Physical Review Materials*, **1**, 7, 075602 (2017). ISSN 2475-9953. doi: 10.1103/PhysRevMaterials.1.075602.

[176] T. Hosokai, H. Matsuzaki, H. Nakanotani, K. Tokumaru, T. Tsutsui, A. Furube, K. Nasu, H. Nomura, M. Yahiro and C. Adachi. Evidence and mechanism of efficient thermally activated delayed fluorescence promoted by delocalized excited states. *Science Advances*, **3**, 5, e1603282 (2017). ISSN 2375-2548. doi: 10.1126/sciadv.1603282.

[177] M. Fuchs, J. Schliemann and B. Trauzettel. Ultralong spin decoherence times in graphene quantum dots with a small number of nuclear spins. *Physical Review B*, **88**, 24, 245441 (2013). ISSN 1098-0121. doi: 10.1103/PhysRevB.88.245441.

[178] J. Hetfield and L. Ulrich. Nothing else matters. *Metallica* (1991).

9 Appendix

9.1 Publications and Conference Contributions

Publications in peer-reviewed journals

1. **Sebastian Weissenseel**, Andreas Gottscholl, Rebecca Bönnighausen, Vladimir Dyakonov, Andreas Sperlich.
   Science Advances (2021)
   Long-lived spin-polarized intermolecular exciplex states in thermally activated delayed fluorescence-based organic light-emitting diodes.
   doi: 10.1126/sciadv.abj9961

2. Nikolai Bunzmann, Benjamin Krugmann, **Sebastian Weissenseel**, Liudmila Kudriashova, Khrystyna Ivaniuk, Pavlo Stakhira, Vladyslav Cherpak, Marian Chapran, Gintare Grybauskaite-Kaminskiene, Juozas Vidas Grazulevicius, Vladimir Dyakonov, Andreas Sperlich.
   Advanced Electronic Materials (2021)
   Spin- and Voltage-dependent emission from Intra- and Intermolecular TADF OLEDs.
   doi: 10.1002/aelm.202000702

3. Nikolai Bunzmann, **Sebastian Weissenseel**, Liudmila Kudriashova, Jeannine Gruene, Benjamin Krugmann, Juozas Vidas Grazulevicius, Andreas Sperlich, Vladimir Dyakonov.
   Materials Horizons (2020)
   Optically and electrically excited intermediate electronic states in donor:acceptor based OLEDs.
   doi: 10.1039/C9MH01475F

4. **Sebastian Weissenseel**, Nikita A. Drigo, Liudmila G. Kudriashova, Markus Schmid, Thomas Morgenstern, Kun-Han Lin, Antonio Prlj, Clémence Corminboeuf, Andreas Sperlich, Wolfgang Brütting, Mohammad Khaja Nazeeruddin, Vladimir Dyakonov.
   The Journal Of Physical Chemistry C (2019)

Getting the Right Twist: Influence of Donor–Acceptor Dihedral Angle on Exciton Kinetics and Singlet–Triplet Gap in Deep Blue Thermally Activated Delayed Fluorescence Emitter.
doi: 10.1021/acs.jpcc.9b08269

5. Nikita A. Drigo, Liudmila G. Kudriashova, **Sebastian Weissenseel**, Andreas Sperlich, Aron Joel Huckaba, Mohammad Khaja Nazeeruddin, Vladimir Dyakonov.
The Journal Of Physical Chemistry C (2018)
Photophysics of Deep Blue Acridane- and Benzonitrile-Based Emitter Employing Thermally Activated Delayed Fluorescence.
doi: 10.1021/acs.jpcc.8b08716

6. Matthias Amthor, **Sebastian Weissenseel**, Julian Fischer, Martin Kamp, Christian Schneider, Sven Höfling.
Optics Express, Optical Society of America (2014)
Electro-optical switching between polariton and cavity lasing in an InGaAs quantum well microcavity.
doi: 10.1364/OE.22.031146

Publications with arXiv Preprint

1. Nikolai Bunzmann, Douglas L. Baird, Hans Malissa, **Sebastian Weissenseel**, Christoph Boehme, Vladimir Dyakonov, Andreas Sperlich. *Preprint on arXiv (2020)* and under Review.
Thermal Activation Bottleneck in TADF OLEDs based on m-MTDATA:BPhen
arXiv: arxiv.org/abs/2008.05781

9.2 Danksagung

An dieser Stelle möchte ich natürliche noch ein paar Dankesworte verlieren und mich an einzelne Personen wenden, welche mich sowohl während dem Studium als auch während dieser Promotion begleitet haben und zum Gelingen dieser Arbeit beigetragen haben:

- Mein erstes Dankeschön geht an Prof. Dr. Vladimir Dyakonov für die Aufnahme an den Lehrstuhl Experimentelle Physik VI und die unkomplizierte Möglichkeit direkt im Anschluss an die Masterarbeit mit der Promotion fortzufahren. Danke für das entgegengebrachte Vertrauen in meine Arbeit, welches mich sehr bei allen Herausforderungen dieser Arbeit bestärkt hat. Die unzähligen kritschen Korrekturen und Verbesserungen zu Publikationen und Probevorträgen haben mich immer ein Stück dem Ziel der Promotion näher gebracht. Danke für die schöne Zeit am Lehrstuhl, welche vorallem durch allerlei Lehrstuhlaktivitäten und Ausflügen unvergesslich wurde.
- PD. Dr. Andreas Sperlich, a.k.a. Hex, als Betreuer oder auch Gruppenleiter der OLED Spinnies möchte ich auch dir besonderen Dank aussprechen. Durch deine kompetente wissenschaftliche Betreuung während der Arbeit und die unzähligen Diskussionen in Mittags- und Kaffeepausen konnte ich mein wissenschaftliches Arbeiten weiterentwickeln und habe viel über das Präsentieren und Diskutieren von wissenschaftlichem Zusammenhängen lernen können. Das Brainstorming am Whitboard oder wöchentliche Sportchallenges mit dir haben mir besonders viel Spaß bereitet.
- Dr. Nikolai Bunzmann, Danke für die Zusammenarbeit über all die Jahre hinweg. Wir haben sehr viel diskutiert, Probleme erörtert, Simulationen durchgespielt und Setups justiert. Mit dir als oberfränkischen Doktorandenkollegen war unmöglich, dass die Stimmung mal nicht am Siedepunkt war. Das Humorbarometer stand bei dir immer auf Anschlag, was mir immer dann geholfen hat, wenns im Labor mal nicht so rund lief.
- Dr. Michael Auth, der sogenannte Spaßminister des Ministry of fun, hat mit seiner Art die EP6 Familie zu etwas besonderem gemacht. *Was kaputt ist, mach wieder ganz*, ist sein Motto hat es hat er mehrmals am ESR Setup unter Beweis gestellt. Danke auch für deinen Rat rund ums Fahrrad! Ich bin schon gespannt auf zukünftige Touren am/mit Heizenberg.
- Ein weiteres Dankeschön geht generell an das OLED Team für das tolle Team-Work und das Arbeitsklima, besonders hierbei an Jeannine Grüne für die kritischen Fragen und Verbesserungen bei Vorträgen und Meetings. Allen beteili-

genten Masteranden und Bacheloranden aus der OLED Gruppe sei hiermit auch gedankt!

- Danke auch an Dr. Kristover Tvingstedt, Dr. Andreas Baumann und Liudmila Kudriashova für die Zusammenarbeit, Diskussionen und zahlreichen Tips rund um Organische Halbleiter!
- Allen weiteren Doktoranden die mich während meiner Zeit am Lehrstuhl begleitet haben. Die EP6 ist einfach einzigartig und ihr gehört dazu.
- Ein besonderer Dank geht hier Philipp Rieder, der mir schon in meiner Masterarbeit viele Tricks und Kniffs im Labor an diversen Setups gezeigt hat. Von dir konnte ich wirklich lernen, was mir für meine meine Promotion sehr geholfen hat. Nicht zuletzt haben wir uns in unserer Schreibphase gegenseitig immer wieder gepushed und motiviert, vorallem dann wenn die Batterie mal wieder leer war.
- Dankeschön auch an Dr. Christian Kasper für die legendäre Labplaylist und Dr. David Kiermasch für die überragende Zeit am Lehrstuhl
- Weiterhin möchte ich allen Bürokollegen im ZEF E13 danken! Andreas Gottscholl für deine hilfsbereite Art. Mit deinem Ehrgeiz bei der Arbeit am Lehrstuhl als auch beim Sport hast du mich immer wieder inspiriert. Die Diskussionen mit Gehirnknoten über unsere (vielen) Bildschirme hinweg waren am Ende doch immer sehr erleuchtend. Moritz Fischer, Felix Brust, und Stefan Kießmüller waren immer bei einem kurzen ALT dabei, was immer wieder den nötigen Dampf aus dem Gehirn entweichen lies. Stephanie Dietz, du hast auch im Winter bei offenem Fenster und ohne Heizung immer für gute Laune gesorgt.
- Unser Techniker Andre Thiem-Riebe, der mit seinem MacGyver know-how immer beiseite Stand, wenn es technische Probleme im Labor zu lösen gab. Deine Hilfestellung und dein Erfahrungsschatz beim Entwerfen diverser Setups sind einfach unersetzbar.
- Allen weiteren Mitgliedern der EP VI, die die zurückliegenden Jahre mit so vielen tollen Ereignissen gefüllt haben!
- Sowieso gilt diese Danksagung allen Korrekturlesern dieser Arbeit, für die intensive Fehlersuche und Verbesserungsvorschläge!
- Hiermit grüße ich noch die Ultra-geile $5 \cdot 10^{-9}$ m große Nano-Crew, Felix, Simon, Jo und Johannes, sowie die Astro-Crew Alex und Josh. Ohne euch hätte mein Studium nicht einmal halb so viel Spaß gemacht! Danke für die vielzähligen Übungsblätter-Sessions und allen sinnfreien Unternehmungen. Danke für die unvergessliche Zeit!
- FREELETICS WÜRZBURG aka Sandicrew: Danke an die wunderschöne Zeit am Sandi. Wenn es mal nicht so rund mit der Arbeit lief gab es immer eine(n) ver-

rückte(n), die/der für eine Burpee Session zu begeistern war. Besonders hervorzuheben ist hierbei die unermüdliche Motivation von dir, Andrea! #nopainnogain #gohardorgohome

- Abschließend danke ich noch Dr. Stephan Lück. Du warst es, der mich damals schon im Physikleistungskurs bestärkt hat, den Pfad der Naturwissenschaften einzuschlagen. Du hast immer ein offenes Ohr in allen Lebenslagen. Danke dafür!
- Last but not least: "Thank you for the music" - Danke der Musik von Ernst Mosch, Sia, Metallica, die Schürzenjäger, Haddaway, Gloryhammer, Meeblech, Dvořák, Beethoven, Mahler und alles was sonst noch während dieser Arbeit durch meine Kopfhörer oder Laborlautsprecher gedröhnt hat. [178]

Besonders danke ich hiermit auch meinen Eltern, welche mich in meinem Tun mein ganzes Leben immer wieder bestärkt und unterstützt haben, sei es bei der Musik oder der Physik. Darüberhinaus gibt es nur noch eine Person, die es nun zu erwähnen gilt: Mareike, Danke für deine unermüdliche Kraft, mit der du mich immer wieder unterstützt hast. Deine einzigartige aufmunternde Art hat mir diesen Weg um vieles leichter gemacht, da du ihn mit mir zusammen gegangen bist. Ich bin sehr gespannt auf die nun folgenden neuen Lebenswege.